

**BEYOND THE EXCEPTIONAL POINT: EXPLORING THE
FEATURES OF NON-HERMITIAN PT SYMMETRIC
SYSTEMS**

by

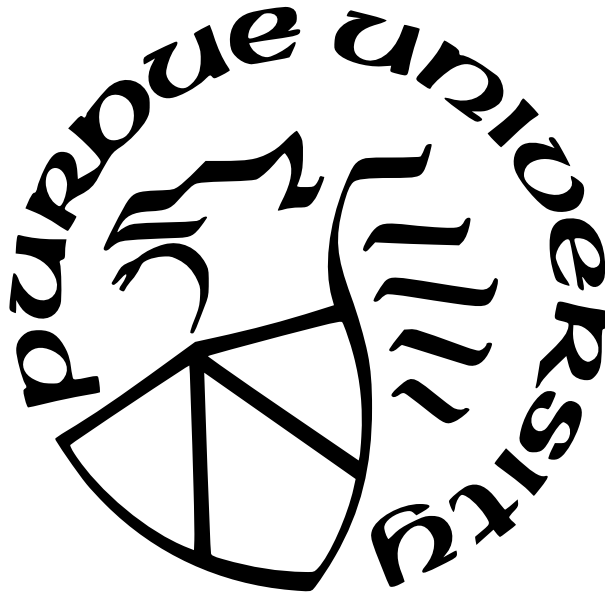
Kaustubh Shrikant Agarwal

A Dissertation

Submitted to the Faculty of Purdue University

In Partial Fulfillment of the Requirements for the degree of

Doctor of Philosophy



Department of Physics

Indianapolis, Indiana

August 2022

**THE PURDUE UNIVERSITY GRADUATE SCHOOL
STATEMENT OF COMMITTEE APPROVAL**

Prof. Yogesh N. Joglekar, Chair

School of Science, Department of Physics

Prof. Gautam Vemuri

School of Science, Department of Physics

Prof. Zhe “Jeff” Ou

School of Science, Department of Physics

Dr. Horia I. Petrache

School of Science, Department of Physics

Dr. Joseph Lukens

Oak Ridge National Laboratory

Approved by:

Dr. Horia I. Petrache

To Shweta, Mimmy, Bhaskar and Papa

ACKNOWLEDGMENTS

I express my sincere gratitude towards Prof. Yogesh N. Joglekar, my mentor, guru, and advisor for all the support, training, and knowledge throughout this journey. I thank him for being very patient with me through my learning curve. Yogesh has taught me to see the beauty in the details of the concepts in physics and their importance in the obstacles we faced in our research.

In this endeavor to achieve prowess in theoretical physics, I have the utmost gratitude towards my family friends, and teachers. I thank my wife Shweta, my mother Anita, and brother Bhaskar for their love and constant support without which this wouldn't have been possible.

I would like to thank my committee members, Dr. Horia I. Petrache, Prof. Gautam Vemuri, Prof. Jeff Ou, and Dr. Joseph Lukens from Oak Ridge National Laboratory for their interest in my research and for providing valuable insights and advice.

I thank Horia for the countless music jam sessions with our band "Play more Drums" which is known all across the Department of Physics at IUPUI. Besides the fun, he has been a constant source of encouragement and life lessons for which I am eternally grateful. There is nothing like a great research group discussion where we can share the happiness and misery of research. I thank my YJTG friends and colleagues: Jacob, Franck, Andrew-the-wise-Harter, Andrew Wilkey, Brendon, Akhil, Ross, Achal, Zach, and Jake. I am grateful to my teachers, Ricardo, Steve, Andy, Marvin, Ruihua, Jing, Vivek, Kashyap, James, and Brian, and my friends and family: Thomas, Andres, Xin, Ashley, Leo, Muchuan, Fadil, Patrick, Lukasz, Azam, Joseph, Saeed, Garrick, Richard, Kristian, David, Jared, Charles, Maria, Kesav, Mihir, Deepesh, Abhijit, Abdul, Nalini, Nagesh, Vaishnavi, Pratik, Urvi, Jinag, Shreyas, Vignesh, Swapnil, Vaibhavi, Deshpandes, Sants, Agrawals and Sawants.

I would also like to thank my master's degree advisor from India, Prof. Rajeev Pathak, for his encouragement and inspiration.

I finally dedicate this thesis to my late father, who showed me the wonders of science and inspired me to study physics.

TABLE OF CONTENTS

LIST OF FIGURES	7
ABSTRACT	13
1 INTRODUCTION	15
1.1 Introduction to \mathcal{PT} -symmetry	15
1.2 The Hamiltonian	17
1.2.1 Floquet quantum mechanics	23
1.2.2 \mathcal{PT} -symmetric Floquet dimer	25
Case 1:	27
Case 2:	29
1.3 Pseudo Hermiticity, intertwining operators, and conserved quantities	31
1.3.1 Conserved quantities in non-Hermitian systems	31
1.3.2 Finding η operators from an eigenvalue problem	33
1.4 \mathcal{PT} -symmetry in optics	35
1.4.1 Beam Propagation method	38
2 \mathcal{PT} -SYMMETRIC LATTICE MODELS	43
2.0.1 Energy spectrum of a tight binding lattice	43
2.1 Non-Hermitian \mathcal{PT} -symmetric chains	46
2.1.1 Strongly coupled chains	49
2.1.2 Numerical calculation of the \mathcal{PT} threshold	50
2.1.3 Results for small systems	51
2.2 A brief introduction to topological superconductors	54
2.3 Understanding the Kitaev Hamiltonian	54
2.4 \mathcal{PT} -symmetric Kitaev chain	57
2.4.1 \mathcal{PT} -threshold Results	58
2.4.2 Exceptional Lines and reentrant \mathcal{PT} phase	66
3 \mathcal{PT} -SYMMETRIC ELECTRICAL CIRCUITS	69

3.1	\mathcal{PT} -symmetry in a single oscillator	69
	Generating a \mathcal{PT} Hamiltonian	72
3.2	Experimental results for a static $H_{\mathcal{PT}}$	74
3.3	Results for a time-periodic $H_{\mathcal{PT}}$	75
3.4	Walking the EP line	78
4	CONCLUSION	83
	REFERENCES	85

LIST OF FIGURES

1.1	Schematic of the various section and chapters in the thesis	16
1.2	A comparison of the energy eigenvalue profiles and inner product plots of eigenvectors for two simple yet significant model non-Hermitian Hamiltonians. The top row demonstrate the flow of the (a) real and the (b) imaginary parts of energy eigenvalues of H_1 and overlap of its eigenstates while (d)-(f) are the plots for the Hamiltonian H_2 . In these two cases, the red and the blue lines show the variation of the real and imaginary parts of the energies as the non-Hermitian gain-loss strength is increased, for $\delta/J = 0$. The black lines in the linear variation of the inner product starting from $I.P. = 0$ for $\gamma/J = 0$ to $I.P. = 1$ for $\gamma/J = 1$. This is the exceptional point where the eigenvectors are parallel to each other.	18
1.3	The evolution of the transmission probability, $ \psi(t) ^2$ (black dashed line), for simple 2-site \mathcal{PT} -symmetric system. The probabilities, $ \langle 1 \psi(t)\rangle ^2$ (blue) and $ \langle 2 \psi(t)\rangle ^2$ (red) for (a) Hermitian case, $\gamma = 0$, (b) \mathcal{PT} -symmetric phase, $\gamma = 0.5J$, (c) at the \mathcal{PT} threshold $\gamma = J$, and (d) when $\gamma = 1.5J$ with broken \mathcal{PT} -symmetry (log scale).	23
1.4	\mathcal{PT} phase plots and eigenstate inner product (I.P.) plots for the system with a square wave modulation described in Eq. 1.23. Panels (a)-(c) show the scaled relative difference in the eigenvalues of the time evolution operator for three different cases of modulation parameterized by α . Panels (d)-(f) show a rich profile of the inner product of the eigenvectors of the G_F . (a)&(d) When $\alpha = -1$ the system switches between a \mathcal{PT} -symmetric dimer and its reflection counterpart. (b)&(e) when $\alpha = 0$ the system is modulates from a \mathcal{PT} -dimer and a Hermitian dimer. Finally when $\alpha = 0.5$ the system modulates between two \mathcal{PT} -symmetric dimers, one with half its gain-loss strength. All three cases show a very rich \mathcal{PT} -phase with the blue region being the symmetric phase and the colored region representing \mathcal{PT} broken phase. The inner product plots show clearly show the region of exceptional line contours where the eigenvectors are parallel to each other. The red dotted line represents the exceptional points of a static dimer	28

1.5	<p>\mathcal{PT} phase plots and eigenstate inner product (I.P.) plots for the system with a square wave modulation described in Eq. 1.25. Panels (a)-(b) show the scaled relative difference in the eigenvalues of the time evolution operator for three different cases of modulation parameterized by α. Panels (c)-(d) shows the inner product of the eigenvectors of the $G_F^{(2)}$. (a)&(c) When $\alpha = -1$ the \mathcal{PT} dimer switches between a negative coupling and a positive coupling. (b)&(d) when $\alpha = 0$ the system is modulates from a \mathcal{PT}-dimer and a completely non-Hermitian dimer with no coupling between the sites. In contrast to the earlier case, when $\alpha = 0$, there is a rich \mathcal{PT}-phase diagram with the blue region being the symmetric phase and the colored region representing \mathcal{PT} broken phase. The inner product plots show clearly show the region of exceptional line contours where the eigenvectors are parallel to each other. The red dotted line represents the exceptional points of a static dimer. When $\alpha = -1$, although there are no \mathcal{PT} phases, it is interesting because we are able to realize an anti-Hermitian Hamiltonian by switching between two \mathcal{PT}-symmetric systems.</p>	30
1.6	<p>Beam Propagation results for a pair of evanescently coupled waveguides of width $5\mu m$ separated by $15\mu m$. The incident light has a wavelength of $630 nm$. The core refractive index is 1.4505 and the cladding refractive index is 1.4500. Panel (a) shows the Hermitian case with $n_I = 0$. In panel (b), $n_I = 2.658 \times 10^{-6}$. Panel (c) show the region of broken \mathcal{PT}-symmetry with the imaginary refractive index as $n_I = 5.316 \times 10^{-6}$ and panel (d) with $n_I = 7.974 \times 10^{-6}$ the intensity increases exponentially (lower subpanel logscale in y).</p>	41
1.7	<p>Variation of the overlap of individual eigenmodes, $\langle e_1 e_2 \rangle$, of the two coupled waveguides as a function of their separation Δx_{gap}.</p>	42
2.1	<p>Schematic of a lattice with (a) Open boundary condition, (b) Periodic boundary condition.</p>	44
2.2	<p>(a) Dispersion relation of a tight binding lattice with nearest neighbour coupling J and $\epsilon_0 = 0$ (b) Probability distribution of eigenstates of a single particle Hamiltonian describing a tight binding lattice with $N = 8$ sites and open boundary condition. Note that the energy axis is independent of the site index and is only there to label the eigenstate to its corresponding energy eigenvalue.</p>	45

- 2.3 1D chain : Plots of the eigenspectrum flow for a lattice of $N = 20$ sites as a function of the non-Hermiticity strength γ/J with the gain-loss sites at the (a) edges i.e. $m_0 = 1$ along with the eigenstates of the Hamiltonian participating in the breaking of \mathcal{PT} -symmetry when (b) $\gamma = 0.5J$ and (c) $\gamma = 1.2J$. (c) As the γ/J is increased beyond the \mathcal{PT} -threshold ($\gamma_{th} = J$) the eigenstate distribution no longer possess parity symmetry. A schematic is provided on the left. (d) This is the eigenspectrum flow for when the gain-loss sites are closest to each other i.e. $m_0 = 10$. (e) One such pair is presented here when $\gamma_{th} = J$ with the feature that not only they have the same eigenvalue but their probability distributions overlap completely. (f) As the non-Hermiticity is increased to $\gamma = 1.2J$ the states with their broken parity symmetry are anti-symmetric to each other. 46
- 2.4 Schematic of a \mathcal{PT} symmetric chain with N_x sites, strongly coupled to $N_y - 1$ Hermitian chains of the same length. The gain site (blue) has a potential $+i\gamma$ and its parity-symmetric site (red) has the loss potential $-i\gamma$. The coupling within a chain is J_x and the inter-chain coupling is J_y 48
- 2.5 Dependence of the \mathcal{PT} -breaking threshold $\gamma_{th}(m_0)/J_x$ on the relative gain position $\mu = 2m_0/N_x$ and the number of horizontal chains N_y for (a) even lattice with $N_x = 26$ and (c) odd lattice with $N_x = 27$. The couplings are $J_y/J_x = 20$. For a single chain, $\gamma_{th}(m_0)$ shows the characteristic U-shape. As N_y is increased, the \mathcal{PT} -threshold increases as well. The graphs in panel (b) and (d) show that the maximum value of the threshold, found for $m_0 = 1$, increases linearly with the number of chains. 51
- 2.6 \mathcal{PT} threshold dependence on coupling to neutral sites shown by blank circles; the gain-site is shown in blue and the loss-site is shown in red. (a) γ_{th}/J_x for a \mathcal{PT} -neutral dimer system is tripled from its single-dimer value when $J_y/J_x = 2$, and saturates to two in the strong coupling limit, $J_y/J_x \gg 1$. (b) for three dimers, the threshold is more than doubled near $J_y/J_x \sim 2$ and saturates to two for $J_y/J_x \gg 1$. Corresponding results for a (c) \mathcal{PT} -neutral trimer system, and (d) a three-trimers system. In all cases, the threshold is more than doubled even at moderate values of $J_y/J_x \gtrsim 2$ 52
- 2.7 Schematic representation of a Kitaev model with one pair of gain and loss potentials, Eq.(2.22). Two chains (gray and white) with detuned potentials $\pm\mu$ have nearest neighbor Hermitian tunneling amplitudes $\pm J$, and next-nearest-neighbor Hermitian amplitudes $\pm i\delta$. Due to the presence of two degree of freedom on each site [60], the potential $i\gamma$ on site m_0 acts as gain (red) for one and loss (blue) for the other. This schematic can be realized with coupled resonator rings where one can engineer complex, Hermitian tunneling amplitudes. 58

- 2.8 Energy eigenvalues (in units of J) of an $N = 20$ site Hamiltonian $H_{\text{BdG}}(\delta)$, Eq.(2.17) as a function of detuning. (a) $\mu/J = 0$, (b) $\mu/J = 1$ have topological edge modes, while the system is in the topologically trivial phase at (c) $\mu/J = 2$ and (d) $\mu/J = 3$. Corresponding \mathcal{PT} threshold values γ_{th}/J obtained from the Hamiltonian H_{K} , Eq.(2.22) are plotted as a function of the gain location $m_0 \in [1, N/2]$ and the superconducting order parameter δ/J : (e) $\mu/J = 0$, (f) $\mu/J = 1$, (g) $\mu/J = 2$ (h) $\mu/J = 3$. Most of these features can be understood in terms of Hermitian band structure, panels a-d. 60
- 2.9 Energy eigenvalues (in units of J) of an $N = 21$ site Hamiltonian $H_{\text{BdG}}(\delta)$, Eq.(2.17) as a function of detuning. (a) $\mu/J = 0$, (b) $\mu/J = 1$ have mid-gap states with zero energy, but these are not topological. (c) $\mu/J = 2$ and (d) $\mu/J = 3$ show emergence of a gapped spectrum. Corresponding \mathcal{PT} threshold values γ_{th}/J obtained from the Hamiltonian H_{K} , Eq.(2.22) are plotted as a function of the gain location $m_0 \in [1, (N - 1)/2]$ and the superconducting order parameter δ/J : (e) $\mu/J = 0$, (f) $\mu/J = 1$, (g) $\mu/J = 2$ (h) $\mu/J = 3$. Due to the absence of topological edge modes, the \mathcal{PT} threshold behavior at $\mu = 0$ is markedly different from that of an even chain, Fig. 2.8(e). At nonzero detuning, the threshold is non-monotonically suppressed with increasing δ 61
- 2.10 (a) \mathcal{PT} -symmetry threshold for a chain with $N = 20$ and $m_0 = N/2$. The white dashed line, separating the zero-threshold region from the nonzero-threshold region, is empirically fit by equation $\alpha\mu J + |J^2 - \delta^2| = 0$ where $\alpha \rightarrow 0.5$ as $N \rightarrow \infty$; at $N = 20$, we find that $\alpha = 0.53$. This functional dependence can be obtained by requiring that two adjacent levels in the Hermitian band-structure become degenerate to get $\gamma_{\text{th}} = 0$. (b) closeup of the boxed region near the origin shows multiple ripples in γ_{th} 63
- 2.11 \mathcal{PT} threshold for an $N = 5$ chain. (a) Schematic of $N = 5$ chain with $m_0 = 1$. (b)-(c) Flow of real part of eigenvalues of the $N = 5$ chain as a function of γ for farthest gain-loss locations (far left) shows that \mathcal{PT} breaking occurs at an EP3 and the threshold increases monotonically with the superconducting order parameter δ . (d) $\gamma_{\text{th}}(\mu, \delta)$ shows behavior consistent with Fig. 2.10 including a contour of zero threshold given by $\alpha\mu J + |J^2 - \delta^2| = 0$. (e) Schematic of $N = 5$ chain with $m_0 = 2$. (f)-(g) Corresponding results for closest gain-loss locations, $m_0 = 2$, show that \mathcal{PT} -breaking occurs at an EP2, and the threshold varies non-monotonically with δ . (h) $\gamma_{\text{th}}(\mu, \delta)$ map shows features similar to those in panel (d). The white-dashed line is zero-threshold contour given by $\alpha\mu J + |J^2 - \delta^2| = 0$ with $\alpha = 1.6$ 64

2.12 (a) \mathcal{PT} phase diagram in the $\gamma - \delta$ plane for an $N = 8$ lattice with $\mu = 0$ and $m_0 = 1$ shows the heat map of $\Lambda \equiv \log_{10} \max_k \Im(E_k)$ where E_k are the $2N$ are the eigenvalues of H_K , Eq.(2.22). A re-entrant \mathcal{PT} -symmetric phase (black) emerges in the range $1 \leq \delta/J \leq \sqrt{2}$ as the gain-loss strength γ/J is increased. (b) EP2 contours at the \mathcal{PT} boundary and in the \mathcal{PT} -broken region show sequential coalescence of eigenvalues. At $\delta/J = 1$, due to the presence of robust Majorana modes, a third-order EP emerges at $\gamma/J = 2$ (yellow circle). (c)-(d) corresponding results for an $N = 24$ lattice shows same qualitative features. 67

3.1 \mathcal{PT} -symmetry in a single LC circuit. (a) The state $|\phi(t)\rangle$ of the circuit encodes the voltage $V(t)$ across the capacitor and current $I(t)$ in the inductor, and satisfies a linear, first-order equation given by Kirchoff laws. A static change-of-basis to $|\psi(t)\rangle = A^{1/2}|\phi(t)\rangle$ leads to a Hermitian Hamiltonian $H_0 = \omega_0\sigma_y$ for the new state $|\psi(t)\rangle$. Thus, an LC circuit is mapped into a two-site model. (b) When $C(t), L(t)$ are exponentially varied subject to the constraint $L(t)C(t) = L_0C_0$ (hyperbola), the time-dependent change of basis generates balanced, constant gain and loss $\pm i\gamma$. This leads to a purely imaginary, \mathcal{PT} -symmetric Hamiltonian $H_{PT} = \omega_0\sigma_y + i\gamma\sigma_z$. (c) When the constrained variation is not exponential, arbitrary, but balanced gain and loss potentials $\pm i\gamma(t)$ can be generated. Here, we focus on the special case when $\gamma(t)$ is periodic. 70

3.2 Dynamics of a \mathcal{PT} -dimer with static gain and loss. (a) Schematics of synthetic LC circuit comprising capacitor (red), inductor (blue), resistor (yellow), and signal adder (pink) boxes. (b) Actual circuit board with corresponding color-coded components marked. The circuit has $C = 100 \mu\text{F}$, $L = 0.01 \text{ H}$, $\omega_0 = (2\pi) \times 159.15 \text{ Hz}$, and a parasitic resistance $R = 10^3 \Omega$. (c)-(d) Circuit energy $\mathcal{E}(t)$ oscillates in the \mathcal{PT} -symmetric phase. The gain-loss strength is (c) $\gamma = 0.375\omega_0$ and (d) $\gamma = 0.75\omega_0$. (e) $\mathcal{E}(t)$ grows exponentially in the \mathcal{PT} -broken phase, $\gamma = 1.05\omega_0$ (experimental data: blue dots, theory: red dashed line). (f) At $\gamma = 0.375\omega_0$ (\mathcal{PT} -symmetric region, PTS) although the circuit energy $\mathcal{E}(t)$ oscillates, $\eta_2(t) = \mathcal{E}(t) + \gamma V(t)I(t)/2\omega_0^2$ remains constant with time. (g) The same, constant behavior of $\eta_2(t)$ is observed at $\gamma = 1.05\omega_0$ (\mathcal{PT} -broken region, PTB). Gray traces are experimental data; red dashed lines are theory. 73

- 3.3 Floquet \mathcal{PT} -transitions and conserved quantities. (a) The step-function $f(t)$ switches $C(t)$ and $L(t)$ by a factor of $e^{\pm\alpha}$ and gives rise to periodic, δ -function gain and loss. Resultant EP lines emerging from odd resonances $\nu_k = 502/(2k+1)$ Hz are shown by red and blue in the $\alpha-\nu_T$ plane. (b) \mathcal{PT} -broken regions in the vicinity of ν_2 (cyan), ν_3 (yellow), ν_4 (pink), and ν_5 (green), signaled by $\Lambda_{\text{amp}} > 0$, are shown (experimental data: filled circles, theory: gray surface). (c) At $\nu_1 = 500/3 = 167$ Hz, the gain saturation leads to a suppressed Λ_{amp} , with the suppression largest near the resonance (experimental data: filled circles; theory with gain saturation: muve surface, theory without: gray mesh). In all cases $2\tau = 50$ ms is used in Eq.(3.18). (d) Constant of motion $\eta_{1F}(t_m)$ is measured near the ν_3 dome (yellow) in the \mathcal{PT} -symmetric phase ($\nu = 69$ Hz; circles) and \mathcal{PT} -broken phase ($\nu = 72$ Hz; diamonds). These data are at $\alpha = 0.1$. (e) Measured values of $\eta_{2F}(t_m)$ near the ν_5 dome (green), both in the \mathcal{PT} -symmetric phase ($\nu = 44$ Hz, circles) and \mathcal{PT} -broken phase ($\nu = 46$ Hz, diamonds). These data are at $\alpha = 0.2$. Gain saturation leads to non-constant behavior at times $t \gtrsim 2\tau$. Gray flat lines are theory in (d)-(e). 76
- 3.4 Giant dynamical asymmetry along the EP contours. (a) The inner-product heat map $I_P(\alpha, \nu_T)$ shows EP lines emerging from odd resonances $\nu_k = 502/(2k+1)$ Hz, consistent with Eq.(3.17). (b) Zoomed-in view near $\nu_1 = 167$ Hz shows the α_{EP} values sampled for the circuit energy dynamics (filled and open circles). (c) Experimentally measured $\mathcal{E}(t)$ for the two EPs at $\alpha = 0.2$ show a giant asymmetry. The circuit energy is constant except at times $pT/2$ ($p \geq 1$) when the δ -function gain-loss potentials are active. (d) Color-coded stroboscopic, normalized energy traces along the blue contour show quadratic behavior consistent with a second-order EP. The (constant) energy along the flat steps in (c) is averaged to obtain error bars on $\mathcal{E}(t_m)/\mathcal{E}(0)$. By fitting the data to Eq.(3.20), $A_{\pm}(\alpha), B_{\pm}(\alpha)$ are obtained for the nine α values sampled along blue and red contours. (e) $A_{\pm}(\alpha)$ show approximate $\alpha \leftrightarrow -\alpha$ symmetry, vanish at the DP as expected, and show that $\mathcal{E}(t_m)$ growth along the red contour is ~ 25 -fold larger than along the blue contour. (f) Similar results, including a giant 25-fold asymmetry, are obtained for $B_{\pm}(\alpha)$ 79

ABSTRACT

Over the past two decades, open systems that are described by a non-Hermitian Hamiltonian have become a subject of intense research. These systems encompass classical wave systems with balanced gain and loss, semi-classical models with mode selective losses, and lossy quantum systems. The rapidly growing research on these systems has mainly focused on the wide range of novel functionalities they demonstrate. In this thesis, I intend to present some intriguing properties of a class of open systems which possess parity (\mathcal{P}) and time-reversal (\mathcal{T}) symmetry with a theoretical background, accompanied by the experimental platform these are realized on. These systems show distinct regions of broken and unbroken symmetries separated by a special phase boundary in the parameter space. This separating boundary is called the \mathcal{PT} -breaking threshold or the \mathcal{PT} transition threshold. We investigate non-Hermitian systems in two settings: tight binding lattice models, and electrical circuits, with the help of theoretical and numerical techniques.

With lattice models, we explore the \mathcal{PT} -symmetry breaking threshold in discrete realizations of systems with balanced gain and loss which is determined by the effective coupling between the gain and loss sites. In one-dimensional chains, this threshold is maximum when the two sites are closest to each other or the farthest. We investigate the fate of this threshold in the presence of parallel, strongly coupled, Hermitian (neutral) chains, and find that it is increased by a factor proportional to the number of neutral chains. These results provide a surprising way to engineer the \mathcal{PT} threshold in experimentally accessible samples. In another example, we investigate the \mathcal{PT} -threshold for a one-dimensional, finite Kitaev chain—a prototype for a p-wave superconductor—in the presence of a single pair of gain and loss potentials as a function of the superconducting order parameter, onsite potential, and the distance between the gain and loss sites. In addition to a robust, non-local threshold, we find a rich phase diagram for the threshold that can be qualitatively understood in terms of the band-structure of the Hermitian Kitaev model. Finally, with electrical circuits, we propose a protocol to study the properties of a \mathcal{PT} -symmetric system in a single LC oscillator circuit which is contrary to the notion that these systems require a pair of spatially separated balanced gain and loss elements. With a dynamically tunable LC oscillator with

synthetically constructed circuit elements, we demonstrate static and Floquet \mathcal{PT} breaking transitions by tracking the energy of the circuit. Distinct from traditional mechanisms to implement gain and loss, our protocol enables parity-time symmetry in a minimal classical system.

1. INTRODUCTION

This chapter mainly contains already established theoretical framework of non-Hermitian PT symmetry, to help set up the background, with one section containing original work published in Acta Polytechnica conference proceedings.

My eight year old journey in exploring non-Hermitian physics probably began very similar to almost all researchers currently in the field: which is the surprise one gets from conventional teachings of quantum mechanics courses that Hamiltonians which describe a physical system, need not be Hermitian to engender a real energy eigenvalue spectrum. This finding took the physics community by storm in 1998 when Carl Bender and Stefan Boettcher published their seminal paper describing a class of quantum Hamiltonians on a continuum line that respect the combined parity (\mathcal{P}) and time-reversal (\mathcal{T}) symmetries show a real eigenvalue spectrum [1]. Their paper currently stands at 5513 citations (at the time of writing this thesis) from various journals. Since then there have been hundreds of papers submitted to *arXiv* under the topic of \mathcal{PT} -symmetry every year. The interesting fact is that it was only over a decade ago that experiments were designed to test some of the properties which I intend to describe in thesis.

This thesis is divided into four chapters, where the first chapter introduces the various concept I have learned and some important algebra pertaining to Non-Hermitian quantum mechanics. The following chapters allude to the new work I have done. Figure 1.1 is a pictorial representation of the thesis, where the bubbles in the blue section (above the research bubble) indicate the background which will collate into the introduction chapter. The bubbles in the red section indicate the chapters which include some of the published and currently ongoing works I have had the opportunity to investigate.

1.1 Introduction to \mathcal{PT} -symmetry

In the past two decades, there has been an explosion of research in the field of non-Hermitian systems described by Hamiltonians which are invariant under the combined operation of parity(\mathcal{P}) and time-reversal(\mathcal{T}). Traditionally in quantum mechanics, the notion of a closed system means that the system is described by a Hermitian Hamiltonian. This

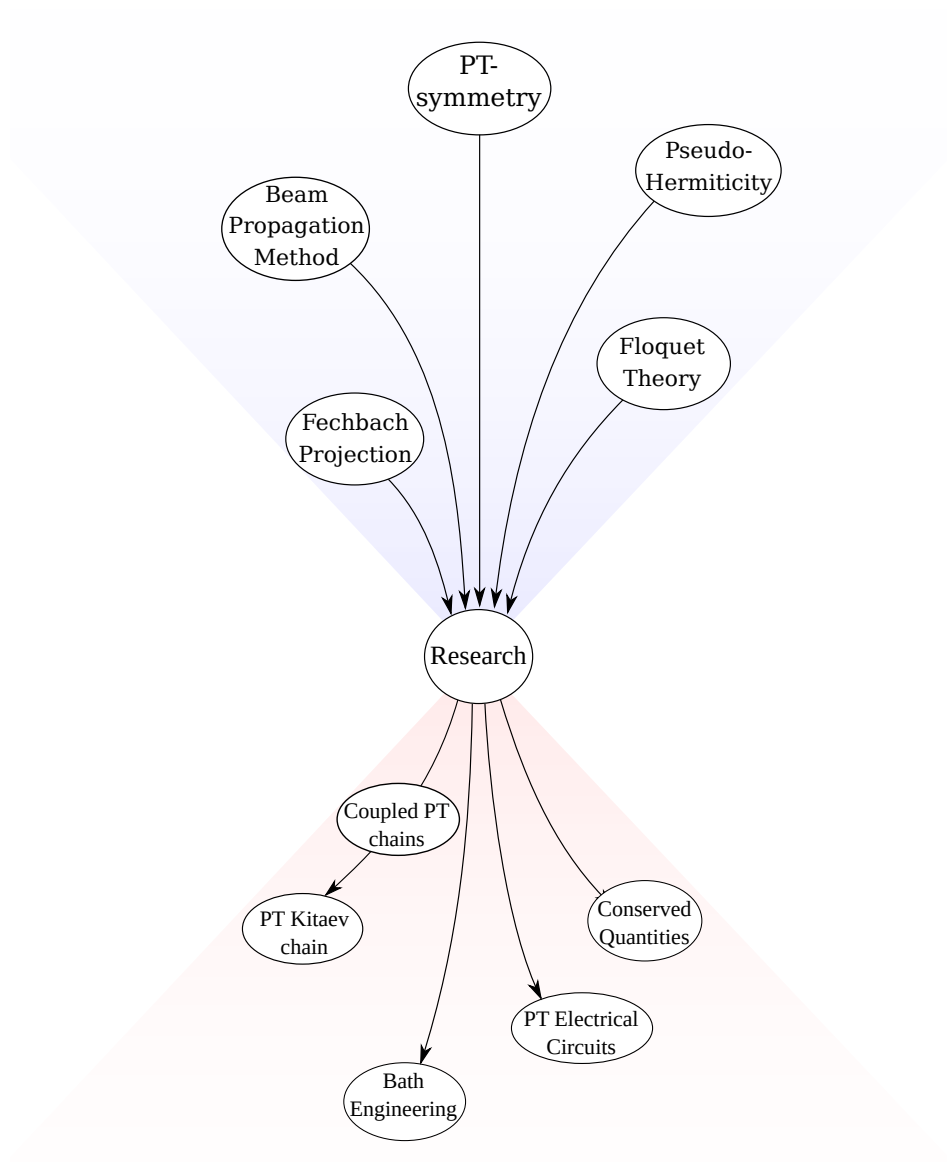


Figure 1.1. Schematic of the various section and chapters in the thesis

is good because Hermiticity guarantees that the energy levels are real and the time evolution operator of the system is unitary. This would mean that the bases states functions of this system spans a Hilbert space implying that the position and momentum operators are observables. More than two decades ago Bender et al. found that certain non-Hermitian Hamiltonians with \mathcal{PT} -symmetry engender a purely real spectra [1], [2]. It was only in the last decade or so, that it has become clear that \mathcal{PT} -symmetric systems can be reproduced in open, semi-classical systems with balanced, spatially or temporally separated gain and loss that are represented by complex real-space potentials [3]–[5]. This idea has been the inspiration of many research ideas including ours.

Ever since its first inception, \mathcal{PT} -symmetry has emerged as a powerful tool to study open classical or quantum systems. The theory is a complex extension of quantum mechanics, based on a special class of non-Hermitian Hamiltonians which have a purely real spectra [1], [2], [6], [7]. This class of Hamiltonians are invariant under the combined operations of parity (\mathcal{P}) and time-reversal (\mathcal{T}). We have now realized that \mathcal{PT} -symmetric systems can be represented by systems with balanced, spatially or temporally separated gain and loss sites [3]–[5].

A special property of these Hamiltonians is that when the strength of the non-Hermiticities is small relative to the energy scale of the Hermitian part, the spectrum is purely real. We refer to this as the \mathcal{PT} -symmetric phase. For large non-Hermiticities, the spectrum turns into complex conjugate pairs which we refer as the \mathcal{PT} -broken phase.

1.2 The Hamiltonian

To illustrate the properties of non-Hermitian physics we begin with a general 2×2 Hamiltonian,

$$H = \begin{pmatrix} W + Z & X - iY \\ X + iY & W - Z \end{pmatrix} \equiv W\mathbb{1} + X\sigma_x + Y\sigma_y + Z\sigma_z, \quad (1.1)$$

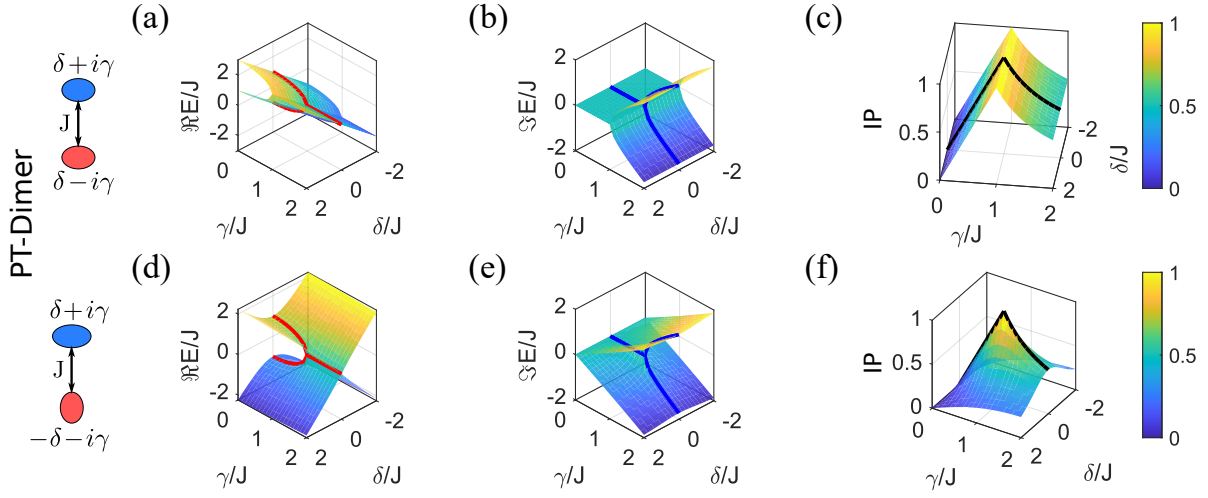


Figure 1.2. A comparison of the energy eigenvalue profiles and inner product plots of eigenvectors for two simple yet significant model non-Hermitian Hamiltonians. The top row demonstrate the flow of the (a) real and the (b) imaginary parts of energy eigenvalues of H_1 and overlap of its eigenstates while (d)-(f) are the plots for the Hamiltonian H_2 . In these two cases, the red and the blue lines show the variation of the real and imaginary parts of the energies as the non-Hermitian gain-loss strength is increased, for $\delta/J = 0$. The black lines in the linear variation of the inner product starting from $I.P. = 0$ for $\gamma/J = 0$ to $I.P. = 1$ for $\gamma/J = 1$. This is the exceptional point where the eigenvectors are parallel to each other.

where W, X, Y, Z are complex coefficients, $\mathbb{1}$ denotes the identity matrix and $\sigma_{x,y,z}$ are the Pauli matrices. The eigenvalues for this non-Hermitian Hamiltonian are,

$$E_{1,2} = W \pm \sqrt{X^2 + Y^2 + Z^2}, \quad (1.2)$$

and the corresponding linearly independent eigenvectors are,

$$|E_{1,2}\rangle = \frac{1}{N_{1,2}} \begin{pmatrix} (E_{1,2} - W + Z)/(X + iY) \\ 1 \end{pmatrix}, \quad (1.3)$$

where $N_{1,2}$ is the appropriate normalization constant.

If the coefficients are real, it is evident that $H = H^\dagger$; i.e. the Hamiltonian is Hermitian with a real energy eigenvalue spectrum. One can then see that if all the coefficients are purely imaginary then this is an example of a trivially broken non-Hermitian Hamiltonian with $H = -H^\dagger$. This is known as anti-Hermiticity. Here the eigenvalues are complex in the entire parameter space. One must notice that in both these cases, that eigenvectors are orthogonal everywhere.

Let us now consider the case when $W = \delta$, $X = -J$ and $Z = i\gamma$.

$$H_1 = \begin{pmatrix} \delta + i\gamma & -J \\ -J & \delta - i\gamma \end{pmatrix} \equiv \delta\mathbb{1} - J\sigma_x + i\gamma\sigma_z. \quad (1.4)$$

The construction of such a simple single particle Hamiltonian is motivated by its representation of two site (dimer) systems with complex on-site potentials and coupling between these sites. Here δ represents the real symmetric potential while $i\gamma$ represents the imaginary anti-symmetric onsite potential and J is the strength of the coupling between two sites. This is clearly a non-Hermitian model since $H \neq H^\dagger$ with the non-Hermiticity in the z-component. This model of a two site system model with balanced gain and loss as illustrated on the far left of the first column of Fig.1.2.

A comparison of the energy eigenvalue profiles and inner product plots of eigenvectors with a contrasting non Hermitian Hamiltonians defined by:

$$H_2 = \begin{pmatrix} \delta + i\gamma & -J \\ -J & -\delta - i\gamma \end{pmatrix} \equiv -J\sigma_x + (\delta + i\gamma)\sigma_z, \quad (1.5)$$

where δ is detuning attached to the σ_z component. In Fig. 1.2 the top row demonstrate the flow of the (a) real and the (b) imaginary parts of energy eigenvalues of H_1 and overlap of its eigenstates while (d)-(f) are the plots for the Hamiltonian H_2 . In these two cases, the red and the blue lines show the variation of the real and imaginary parts of the energies as the non-Hermitian gain-loss strength is increased, for $\delta/J = 0$. The black lines in the linear variation of the inner product starting from inner product $I.P. = 0$ for $\gamma/J = 0$ to $I.P. = 1$ for $\gamma/J = 1$. This is the exceptional point where the eigenvectors are parallel to each other. Notice that for H_1 a change in δ does not change the relative difference in the energies as compared to the model described by H_2 . At the exceptional point, perturbing the system by increasing δ , increases the energy gap proportional to $\sqrt{\delta}$ in the first order correction to the eigenvalue. The perturbation series of eigenvalues of non-Hermitian Hamiltonians is known as the Puiseux series ¹. This is different from the regular power series expansion for Hermitian Hamiltonians where the first order correction is linear. This means that a system described by a non-Hermitian Hamiltonian is more sensitive to perturbation. This idea is the bases for making ultra sensitive sensors using non-Hermitian physics. In our current example, $n = 2$. By definition the order of an exceptional point is the size of the Jordan block.

Let us now look at the symmetries of this problem. We define the linear parity operator, as $\mathcal{P} = \sigma_x$ and an anti-linear time reversal operator as $\mathcal{T} = *$ where $*$ is the complex conjugation operation and one can verify that $\mathcal{P}\mathcal{T}H_{1,2}\mathcal{P}\mathcal{T} = H_{1,2}$. This Hamiltonian is $\mathcal{P}\mathcal{T}$ -symmetric!

The next obvious question is that *What are the conservation laws or quantities that are associated with these symmetries?* We will answer this in the later sections of this chapter

¹↑ $E = E_0 + \Delta^{1/N} E_1 + \Delta^{2/N} E_2 + \dots$

under *Pseudo-Hermiticity and Intertwining operators*. The phase transition from \mathcal{PT} -symmetric to \mathcal{PT} -broken occurs when $\gamma = \gamma_{\text{th}} = J$, where γ_{th} is called the \mathcal{PT} -symmetry breaking threshold. At this point the eigenvalues become degenerate. The most intriguing feature of the transition point is that the non-Hermiticity not only induces the degeneracies in the eigenvalues, but also in their corresponding eigenvectors. Such a Hamiltonian degeneracy is called an exceptional point (EP) degeneracy. Fig. 1.2(c) shows the overlap of the two eigenstates calculated by their Dirac inner product; $I.P.(\delta/J, \gamma/J) = \langle E_1 | E_2 \rangle / |E_1| |E_2|$.

In the past decade, \mathcal{PT} -symmetric systems with balanced gain-loss have been realized in classical wave systems including evanescently coupled waveguides [8], fiber loops [9], optical resonators [10], [11], electrical circuits [12], [13], and mechanical oscillators [14]. However, since the EP degeneracies also occur for Hamiltonians with mode selective dissipation, the dynamics of \mathcal{PT} -symmetric Hamiltonians have also been realized in purely lossy classical systems consisting of coupled waveguides, resonators, or electrical circuits [15], [16], semi-classical systems with ultracold atoms [17], and quantum systems [18]–[20]. These systems, in the definition of quantum mechanics, engender a complex energy eigenvalue spectrum. About two decades ago, Carl Bender and Stefan Boettcher made a remarkable discovery where they realized that a non-Hermitian system, if invariant under the combined operation on parity(\mathcal{P}) and time reversal(\mathcal{T}), will exhibit a real energy spectrum [1]. With the birth of this new field, investigations were carried out which are physically realized as systems with balanced, spatially separated, gain and loss [21] locations, with an effective coupling between them. Traditional Dirac Hermiticity in quantum mechanics, ensures the preservation of the norm and hence is a sufficient condition to guarantee a real energy spectrum. It is now shown that, a system having an antilinear symmetry (like \mathcal{PT}), and anti-unitary, serves as a necessary condition to produce real energy eigenvalues [22], [23], thus making it a more general theory of quantum mechanics. Typically, a non-Hermitian \mathcal{PT} -symmetric system behaves either like an open or a closed system depending on the strength of the non-Hermiticity. As this strength increases, two (or more) real eigenvalues become degenerate as do the corresponding eigenvectors. Although, \mathcal{PT} -symmetric quantum mechanics was initially studied on a continuum line, experimental realizations, in the past few years, have been done using simple discrete models. Therefore, with the motivation to investigate

the aspects of the \mathcal{PT} -symmetry breaking threshold, we study discrete quantum systems which are generalizations of a simple dimer model with one pair of \mathcal{PT} -symmetric gain-loss potentials. In Fig. 1.2(a), the energy eigenvalues start out distinct and real when $\gamma/J = 0$. As the non-Hermiticity increases, the energy levels are drawn closer to each other. At this point, the corresponding eigenvectors are no longer orthonormal.

Furthermore, we can also define our time evolution operator (let $\hbar = 1$) as

$$G(t) \equiv e^{-iHt} = G(t) = \cos(Et)\mathbb{1} - i\frac{H}{E}\sin(Et) \quad (1.6)$$

Consider that $|1\rangle$ and $|2\rangle$ are the normalized states in the site basis, with 1 representing the gain site and 2 the loss site. We can rewrite the Hamiltonian in the site basis as

$$H = i\gamma(|1\rangle\langle 1| - |2\rangle\langle 2|) - J(|1\rangle\langle 2| + |2\rangle\langle 1|) \quad (1.7)$$

We evolve a wavefunction, $|\psi(t=0)\rangle = a|1\rangle + b|2\rangle$ starting in the gain site, i.e. $a = 1$ and $b = 0$; i.e.

$$|\psi(t)\rangle = G(t)|\psi(t=0)\rangle = G(t)|1\rangle \quad (1.8)$$

Fig. 1.3 captures the evolution of the norm of the wavefunction $|\psi(t)|^2$ for different values of γ . In the Hermitian case, panel(a), the norm (black dashed line) is constant. The blue and red lines indicate the probability of the wavefunction projected onto 1 and 2 respectively. As the non-Hermiticity is increased to $0.5J$, panel(b), we notice the total probability is no longer conserved but exhibits a bounded oscillatory behavior much like the Hermitian case. With $\gamma = J$, panel(c), at the \mathcal{PT} transition threshold, the probability has a quadratic increase in time. In panel(d), the probability increases exponentially (figure shows linear growth in log scale) as the system is rendered into the \mathcal{PT} broken phase with $\gamma = 1.2J$.

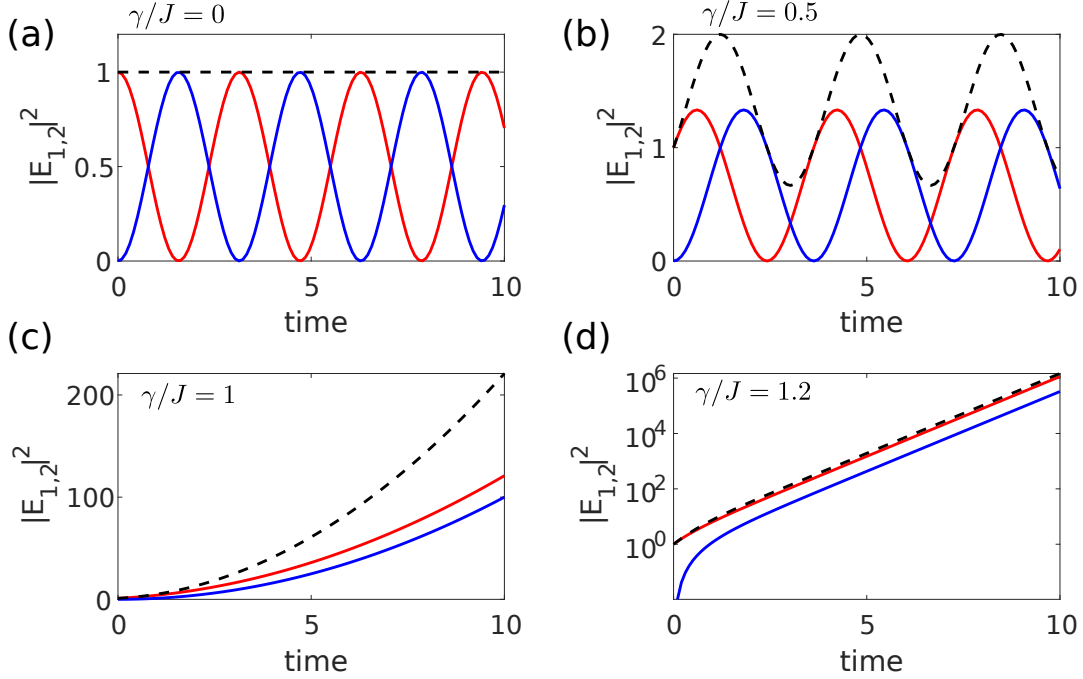


Figure 1.3. The evolution of the transmission probability, $|\psi(t)|^2$ (black dashed line), for simple 2-site \mathcal{PT} -symmetric system. The probabilities, $|\langle 1|\psi(t)\rangle|^2$ (blue) and $|\langle 2|\psi(t)\rangle|^2$ (red) for (a) Hermitian case, $\gamma = 0$, (b) \mathcal{PT} -symmetric phase, $\gamma = 0.5J$, (c) at the \mathcal{PT} threshold $\gamma = J$, and (d) when $\gamma = 1.5J$ with broken \mathcal{PT} -symmetry (log scale).

1.2.1 Floquet quantum mechanics

Let us now introduce an interesting formalism to engineer different quantum systems that may be difficult to investigate experimentally. A quantum system is driven by external fields such that the Hamiltonian describing the system follows,

$$H(t) = H(t + T), \quad (1.9)$$

where T is the time period of the periodic drive. The Floquet formalism provides a recipe for generating a static effective Hamiltonian by periodically probing the system at integer multiples of time period of the driving field.

We will explore some details of this formalism in this section through some examples of simple two level systems. Consider the time-dependent Schrödinger equation;

$$H(t)|\psi(t)\rangle = i\hbar\partial_t|\psi(t)\rangle \quad (1.10)$$

where $H(t) = H(t + T)$ is a time-periodic Hamiltonian with a drive frequency of $\omega = 2\pi/T$ acting on an eigenstate $|\psi(t)\rangle$. For simplicity we assume $\hbar = 1$.

We are particularly interested in the dynamics of the state $|\psi(t)\rangle$ as measured stroboscopically, i.e. $t = nT$. This leads to the following definition of the time operator $G(T)$ as a time ordered product

$$G(T, 0) = \mathbb{T}e^{-i\int_0^T H(t)dt} \equiv e^{-iH_F T}, \quad (1.11)$$

where \mathbb{T} indicates the time-ordering operator.

According to the theory, we can define an effective Floquet Hamiltonian H_F using the Floquet time evolution operator,

$$G(t) = P(t) \exp[-iH_F t], \quad (1.12)$$

where $P(t) = P(t + T)$ is called the micromotion operator that describes the dynamics with a single period. Using the initial condition, $G(t = 0) = \mathbb{1}$ implies that

$$P(0) = P(nT) = \mathbb{1} \quad \forall n \in \mathbb{Z}^+. \quad (1.13)$$

It is easy to see that if an observer was to make periodic observations starting at $t = t_0$ during the driving cycle, the new time evolution operator is related to $G(t)$ by a similarity transformation:

$$\tilde{G}(T + t_0, t_0) = \hat{S}^{-1}G(T, 0)\hat{S}, \quad (1.14)$$

where \hat{S} is micromotion operator that connects the observation times. Consequently, the effective Hamiltonians will also change based on when one begins to observe :

$$\tilde{H}_F(t_0) = \hat{S}^{-1}H_F(0)\hat{S}. \quad (1.15)$$

This method shows us a way to realise a whole new class of \mathcal{PT} -symmetric systems. The time dependent Hamiltonian representations may not even be \mathcal{PT} -symmetric, but it could on some stroboscopic observation lead to an effective \mathcal{PT} -symmetric Hamiltonian representation. To illustrate we this, investigate two simple dimer models with a periodically driven by a square wave.

1.2.2 \mathcal{PT} -symmetric Floquet dimer

Let us consider a \mathcal{PT} -symmetric dimer with the matrix representation as given in Eq.1.4 with $\delta/J = 0$.

$$H(t) = \begin{pmatrix} +i\Gamma(t) & -\kappa(t) \\ -\kappa(t) & -i\Gamma(t) \end{pmatrix}. \quad (1.16)$$

Now let's examine two cases: Case 1, where the non-Hermitian onsite potential ($\Gamma(t) = \gamma f(t/T)$) is driven while the intersite coupling ($\kappa = J$) is kept constant during the cycle. Case 2, where the coupling $\kappa(t) = Jf(t/T)$ is driven while the onsite potential ($\Gamma(t) = \gamma$) is constant. Here $f(t/T)$ is the driving function. The two cases produce distinct and rich phase diagrams showing regions of broken and unbroken \mathcal{PT} -symmetries. For the sake of analytical tractability, let us consider the periodic driving function to be a square wave with a time period of T defined as :

$$f(t/T) = \begin{cases} 1 & 0 \leq t < T/2 \\ \alpha & T/2 \leq t < T \end{cases} \quad (1.17)$$

where $\alpha \in [-1, 1)$ is the lower limit of the function. Let us call these Hamiltonians $H_{1,2} = e_{1,2} \vec{\sigma}$. Here we define $\vec{\sigma} = \sigma_x \hat{x} + \sigma_y \hat{y} + \sigma_z \hat{z}$, and the complex vectors $e_{1,2} = ex_{1,2} \hat{x} + ey_{1,2} \hat{y} + ez_{1,2} \hat{z}$. This means that the first half of the cycle, the system is described by Hamiltonian H_1 while for the second half of the cycle the Hamiltonian is H_2 . In practice, driving the system in between these states is also experimentally easier to implement.

The general form for the Floquet time evolution operator in a two site basis with a square wave modulation [24] is:

$$G_F(T) = [C_1 C_2 - (\vec{e}_2 \cdot \vec{e}_1) S_1 S_2] \mathbb{1}_2 + i [C_1 S_2 \vec{e}_1 + C_2 S_1 \vec{e}_2 + (\vec{e}_2 \times \vec{e}_1)] \cdot \vec{\sigma}, \quad (1.18)$$

where $C_1 = \cos(E_1 T/2)$, $C_2 = \cos(E_2 T/2)$, $S_1 = \sin(E_1 T/2)$, $S_2 = \sin(E_2 T/2)$ and $E_{1,2} = |\vec{e}_{1,2}| = \sqrt{ex_{1,2}^2 + ey_{1,2}^2 + ez_{1,2}^2}$, which is also the positive energy eigenvalue of $H_{1,2}$.

In order to see the features of the effective Floquet Hamiltonian we need to calculate the time evolution operator, which fortunately for us, can be easily found for these two level systems with a square wave drive. Recall our definition in Eq. 1.11. To find the Floquet Hamiltonian H_F , $G_f(T)$ can be rewritten as:

$$G_F(T) \equiv e^{-h_0 T} \left[\cos(|\vec{h}|T) \mathbb{1} - i \frac{\vec{\sigma} \cdot \vec{h}}{|\vec{h}|} \sin(|\vec{h}|T) \right] \quad (1.19)$$

$$\text{where } H_F = h_0 \mathbb{1}_2 + \vec{\sigma} \cdot \vec{h}. \quad (1.20)$$

The Floquet Hamiltonian is written in terms of the Pauli matrices, with $\vec{h} = h_x \hat{x} + h_y \hat{y} + h_z \hat{z}$ and $|\vec{h}| = \sqrt{h_x^2 + h_y^2 + h_z^2}$.²

Since the behaviour of $G_F(T)$ switches between unitary and non-unitary, we can thus introduce a robust parameter $\Delta\xi$ which we define as the scaled absolute difference of the magnitudes of the eigenvalue of $G_F(T)$.

$$\Delta\xi = \left| \frac{|g_1| - |g_2|}{|g_1| + |g_2|} \right| \quad (1.21)$$

Fig. 1.41.5 reveals a rich phase diagram with \mathcal{PT} -symmetric and \mathcal{PT} -broken regions. Since these phase plot have a phase boundary, it is only natural to ask *are there exceptional points?* We therefore calculate the inner product of the eigenvectors of $G_F(T)$ in order to compute these exceptional line contours and also support the phase diagrams plots. Recall

²↑With the eigenspectrum decomposition of $G_F = V \Lambda V^{-1}$ one can compute the effective Floquet Hamiltonian $H_F = \frac{i}{T} V \log[\Lambda_{G_F}] V^{-1}$ using symbolic numerical techniques

that at the exceptional points the eigenvectors are parallel to each other. The metric we used is simply the Dirac inner product:

$$I.P. = |\langle g_1 | g_2 \rangle|, \quad (1.22)$$

where $|g_{1,2}\rangle$ are the eigenvectors of $G_F(T)$.

Case 1:

In this case, constructing of the Floquet system from the Hamiltonian in Eq.1.16, the periodic switch happens between :

$$H_1 = \begin{pmatrix} +i\gamma & -J \\ -J & -i\gamma \end{pmatrix} \quad \text{and} \quad H_2 = \begin{pmatrix} +i\alpha\gamma & -J \\ -J & -i\alpha\gamma \end{pmatrix}. \quad (1.23)$$

The time evolution operator for one period can be thus constructed simply as the time ordered product of the two individual half cycles [24]:

$$G_F^{(1)} = e^{-iH_2T/2} e^{-iH_1T/2} \quad (1.24)$$

Fig. 1.4 shows the \mathcal{PT} phase plots numerically computed using Eq. 1.21 and eigenstate inner product from Eq. 1.22 for this system with a square wave modulation. Panels (a)-(c) show the scaled relative difference in the eigenvalues of the time evolution operator for three different cases of modulation parameterized by α . It is interesting to see that different values of α have unique phase diagrams since their effective Hamiltonians represent completely different systems. When $\alpha = -1$ the system switches between a \mathcal{PT} -symmetric dimer and its reflection counterpart. Panels (a) and (d) show the relative difference of the eigenvalues and inner product plots for this type of system. Notice in panel (a) as the frequency of modulation is increased the \mathcal{PT} breaking threshold is also enhanced which is not seen in the other cases. When $\alpha = 0$, the system is modulates from a \mathcal{PT} -dimer and a purely real, Hermitian Hamiltonian. Finally when $\alpha = 0.5$ the system modulates between two \mathcal{PT} -symmetric dimers, one with half its gain-loss strength. For all three cases, the inner product

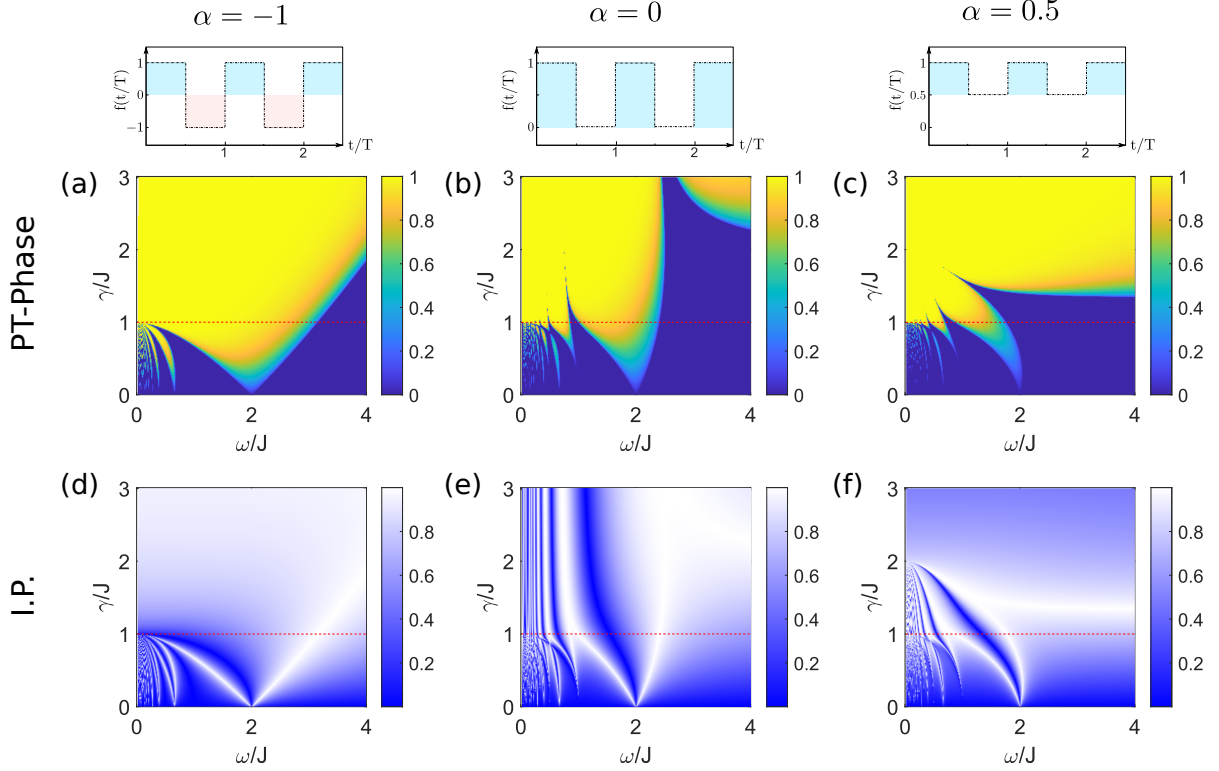


Figure 1.4. \mathcal{PT} phase plots and eigenstate inner product (I.P.) plots for the system with a square wave modulation described in Eq. 1.23. Panels (a)-(c) show the scaled relative difference in the eigenvalues of the time evolution operator for three different cases of modulation parameterized by α . Panels (d)-(f) show a rich profile of the inner product of the eigenvectors of the G_F . (a)&(d) When $\alpha = -1$ the system switches between a \mathcal{PT} -symmetric dimer and its reflection counterpart. (b)&(e) when $\alpha = 0$ the system is modulates from a \mathcal{PT} -dimer and a Hermitian dimer. Finally when $\alpha = 0.5$ the system modulates between two \mathcal{PT} -symmetric dimers, one with half its gain-loss strength. All three cases show a very rich \mathcal{PT} -phase with the blue region being the symmetric phase and the colored region representing \mathcal{PT} broken phase. The inner product plots show clearly show the region of exceptional line contours where the eigenvectors are parallel to each other. The red dotted line represents the exceptional points of a static dimer

plots show a key feature missing from the phase diagrams. These are the contours of zero overlap deep in the broken region signifying resonances in the system. These regions show a similar behavior to non-Hermitian systems with completely decoupled gain-loss elements. The red dotted line represents the exceptional points of a static dimer. This line is there to show that at certain points the system has real eigenvalues even when the individual half cycle Hamiltonians have an exceptional point.

Case 2:

Contrary to the earlier case, we can now see if periodic changes in the Hamiltonian Eq.1.16, occur in the coupling between the two sites; i.e. :

$$H_1 = \begin{pmatrix} +i\gamma & -J \\ -J & -i\gamma \end{pmatrix} \quad \text{and} \quad H_2 = \begin{pmatrix} +i\gamma & -\alpha J \\ -\alpha J & -i\gamma \end{pmatrix}. \quad (1.25)$$

The features seen in the phase diagrams in Fig. 1.5 are contrasting to case 1. The motivation to study this case is important to quantum experiments done in platforms using photonics and superconducting qubits where modulating the gain is specially difficult.

Fig. 1.4 shows the \mathcal{PT} phase plots numerically computed using Eq. 1.21 and eigenstate inner product from Eq. 1.22 for this system with a square wave modulation. When $\alpha = -1$ the \mathcal{PT} dimer switches between a negative coupling and a positive coupling. In panels (b) and (d) when $\alpha = 0$ the system is modulates from a \mathcal{PT} -dimer and a completely non-Hermitian dimer with no coupling between the sites. In contrast to the earlier case, when $\alpha = 0$, there is a rich \mathcal{PT} -phase diagram with the blue region being the symmetric phase and the colored region representing \mathcal{PT} broken phase. The inner product plots show clearly show the region of exceptional line contours where the eigenvectors are parallel to each other. The red dotted line represents the exceptional points of a static dimer. When $\alpha = -1$, although there are no \mathcal{PT} phases, it is interesting because we are able to realize an anti-Hermitian Hamiltonian by switching between two \mathcal{PT} -symmetric systems.

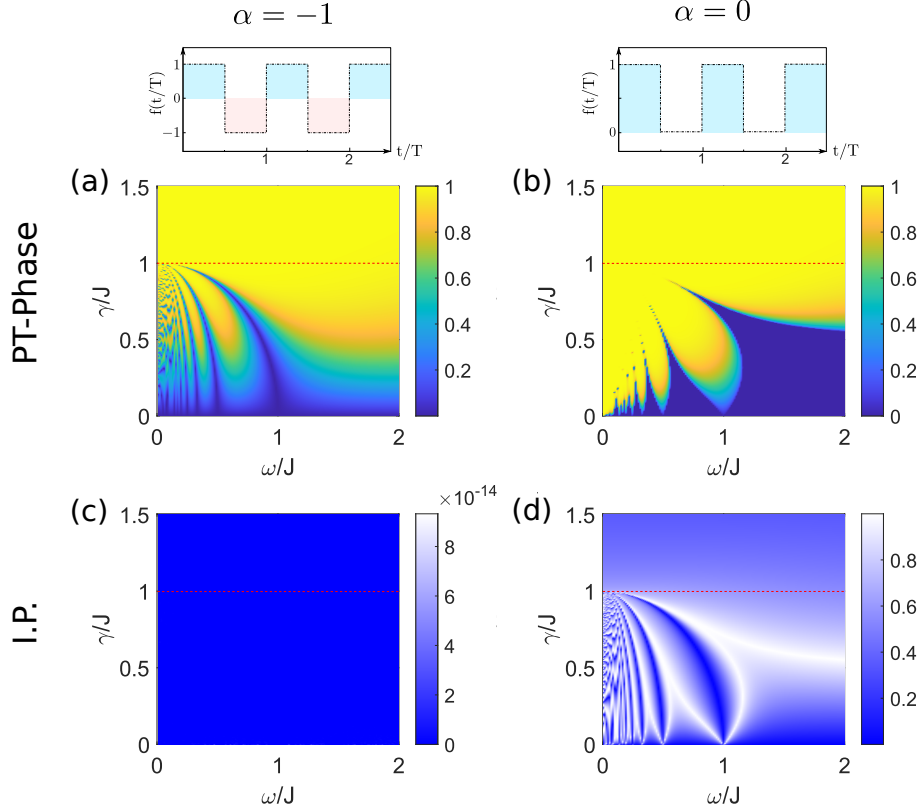


Figure 1.5. \mathcal{PT} phase plots and eigenstate inner product (I.P.) plots for the system with a square wave modulation described in Eq. 1.25. Panels (a)-(b) show the scaled relative difference in the eigenvalues of the time evolution operator for three different cases of modulation parameterized by α . Panels (c)-(d) shows the inner product of the eigenvectors of the $G_F^{(2)}$. (a)&(c) When $\alpha = -1$ the \mathcal{PT} dimer switches between a negative coupling and a positive coupling. (b)&(d) when $\alpha = 0$ the system is modulates from a \mathcal{PT} -dimer and a completely non-Hermitian dimer with no coupling between the sites. In contrast to the earlier case, when $\alpha = 0$, there is a rich \mathcal{PT} -phase diagram with the blue region being the symmetric phase and the colored region representing \mathcal{PT} broken phase. The inner product plots show clearly show the region of exceptional line contours where the eigenvectors are parallel to each other. The red dotted line represents the exceptional points of a static dimer. When $\alpha = -1$, although there are no \mathcal{PT} phases, it is interesting because we are able to realize an anti-Hermitian Hamiltonian by switching between two \mathcal{PT} -symmetric systems.

1.3 Pseudo Hermiticity, intertwining operators, and conserved quantities

This section consists of excerpts from our paper on intertwining operators and conserved quantities which have been slightly modified

We have noticed that Hermiticity is not a necessary condition for eigenvalues to be real. It is however Hamiltonians with an antilinear symmetry (like \mathcal{PT}), where reality of eigenvalues is possible [25]. \mathcal{PT} -symmetry provides an way to implement the symmetry in a physical setting by spatial separation of gain-loss elements. We will now see a more general idea called pseudo Hermiticity that provides a deeper insight into the properties of general non-Hermitian operators [6], [7], [26].

To establish the idea of pseudo-Hermiticity, we assume a linear operator H acting on the Hilbert space. H is said to be pseudo-Hermitian if it satisfies the following relation,

$$H^\dagger = \eta H \eta^{-1} \tag{1.26}$$

where η is an invertible, Hermitian linear operator, also called the intertwining operator.

1.3.1 Conserved quantities in non-Hermitian systems

The content of this subsection is a part of our paper published in Journal of Physics: Conference series.

In classical mechanics, observables that are conserved during time evolution are most easily defined in the Hamiltonian formalism, where they are determined by a vanishing Poisson bracket [27]. Therefore, it should come at no surprise that their quantum counterparts become by far most apparent in the Heisenberg picture. Let the system under consideration be governed by a static Hamiltonian H that may not be Hermitian. It satisfies the equations of motion $i\partial_t|\psi(t)\rangle = H|\psi(t)\rangle$ and $-i\partial_t\langle\psi(t)| = \langle\psi(t)|H^\dagger$. By definition, a linear operator η is a constant of motion if and only if $\langle\psi(t)|\eta|\psi(t)\rangle = \text{Tr}[\eta\rho_\psi(t)]$ remains constant for any

arbitrary state $|\psi\rangle$ (or a density matrix ρ_ψ). In the absence of intrinsic time-dependence, this constraint translates into

$$i\frac{d}{dt}\langle\psi(t)|\eta|\psi(t)\rangle = \langle\psi(t)|\eta H - H^\dagger\eta|\psi(t)\rangle = 0. \quad (1.27)$$

Due to the linearity of the constraint in Eq.(1.27), without loss of generality, we can choose η to be a Hermitian matrix. When $H = H^\dagger$ (an isolated system), the observable conservation is therefore equivalent to commutation of η with H , just as expected. A Hermitian system trivially leaves two important operators conserved, namely the identity (state-norm) and the Hamiltonian itself (energy). We emphasize that many more independent, conserved operators can be constructed very easily; an example is the set of Hermitian projectors onto the eigenspace for each real eigenvalue. These are often disregarded in many applications since they are not connected to fundamental symmetries of the system. However, they fulfill all requirements for a genuine conserved observable and will play an important role in the following analysis. When H is not Hermitian, Eq.(1.27) leads to the following intertwining constraint,

$$\eta H = H^\dagger \eta. \quad (1.28)$$

This characterization of conserved observables as intertwining operators, Eq.(1.28), has appeared in the literature in the context of pseudo-Hermitian operators (η is invertible) [6], [7], [28]. Here, we only focus on them as conserved observables for an open system with gain and loss.

A simple but powerful way to generate these conserved operators may be constructed iteratively by using the prescription

$$\eta_{k+1} = \eta_k H \quad (1.29)$$

starting from an initial η_1 that is determined from the outset. Note that if η_k is Hermitian, the intertwining relation Eq.(1.28) implies that recursively obtained η_{k+1} is also Hermitian. It also follows that the different η operators do not commute with each other, and the

commutator is proportional to the anti-Hermitian part of H . Finally, since H obeys a characteristic polynomial equation of order n , it follows that

$$\eta_{N+1} = \eta_1 H^N, \quad (1.30)$$

can be written as a linear combination of lower-order operators $\eta_{k \leq N}$. Thus, for an n -dimensional system, this recursive procedure gives rise to n non-commuting, linearly independent conserved observables [29].

For a broad class of transpose-symmetric Hamiltonians η_1 is found as follows. For conserved quantities to exist, the Hamiltonian must have purely real or complex-conjugate eigenvalues, i.e. an antilinear operator \mathcal{A} commutes with it. Let us write $\mathcal{A} = \mathcal{P}\mathcal{T} = \mathcal{L}*$ where \mathcal{L} denotes *the entire linear part of \mathcal{A}* and $*$ is purely the complex-conjugation operation. (In general, the operator \mathcal{T} has a nontrivial unitary part; that has been absorbed into the operator \mathcal{L} .) It is easy to see that if $H = H^T$, then \mathcal{L} is an intertwining operator. Once $\eta_1 = \mathcal{L}$ is identified, the rest are determined by the recursive procedure.

1.3.2 Finding η operators from an eigenvalue problem

The content of this subsection is a part of our paper published in Acta Polytechnica conference proceedings.

Here is a novel method we developed to find the conserved quantities by treating the intertwining relation we mentioned in Eq. 1.26 as an eigenvalue equation [30]. Let us recall, the constraint condition in Eq. 1.27. This equation is reminds of the Gorini Kossakowski Sudarshan Lindblad (GKSL) equation [31], [32] (henceforth referred to as the Lindblad equation) that describes the dynamics of the reduced density matrix of a quantum system coupled to a much larger environment [33]–[35]. Interpreting $\hat{\eta}$ as an $N \times N$ matrix, all $\hat{\eta}$ s that satisfy Eq.(1.27) can be obtained from the corresponding eigenvalue problem

$$\mathcal{E}_k \hat{\eta}_k = -i(\hat{\eta}_k H_{\text{PT}} - H_{\text{PT}}^\dagger \hat{\eta}_k) \equiv \mathcal{L} \hat{\eta}_k, \quad (1.31)$$

for $1 \leq k \leq N^2$. We vectorize the matrix $\hat{\eta}$ into an N^2 -sized column vector $|\eta^v\rangle$ by stacking its columns, i.e. $[\hat{\eta}]_{pq} \rightarrow \eta_{p+(q-1)N}^v$ [36]. Under this vectorization, the Hilbert-Schmidt trace inner product carries over to the Dirac inner product, $(\hat{\eta}_1^\dagger \hat{\eta}_2) = \langle \eta_1^v | \eta_2^v \rangle$ where $\langle \eta_1^v |$ is the Hermitian-conjugate row vector obtained from the column vector $|\eta_1^v\rangle$. Using the identity $A\hat{\eta}B \rightarrow (B^T \otimes A)|\eta^v\rangle$, the eigenvalue problem Eq. (1.31) becomes $\det(\mathcal{L} - \mathcal{E}\mathbf{1}_{N^2}) = 0$ where the $N^2 \times N^2$ ‘‘Liouvillian’’ matrix is given by

$$\mathcal{L} = -i \left[H_{\text{PT}}^T \otimes \mathbf{1}_N - \mathbf{1}_N \otimes H_{\text{PT}}^\dagger \right], \quad (1.32)$$

and $\mathbf{1}_m$ is the $m \times m$ identity matrix. Thus, the intertwining operators are distinct eigenvectors $|\eta_m^v\rangle$ with zero eigenvalue in Eq.(1.31). The N^2 eigenvalues of the Liouvillian \mathcal{L} are simply related to N eigenvalues ϵ_m of the H_{PT} as

$$\mathcal{E}_{pq} = -i(\epsilon_p - \epsilon_q^*). \quad (1.33)$$

Since the spectrum of H_{PT} is either real ($\epsilon_p = \epsilon_p^*$) or complex conjugates ($\epsilon_p = \epsilon_q^*$ for some pair), there are N zero eigenvalues of \mathcal{L} when H_{PT} has no symmetry-driven degeneracies; the number of zero eigenvalues grows to N^2 if the Hamiltonian is proportional to the identity matrix [37]. Note that when $\mathcal{E} = 0$, due to the linearity of the intertwining relation, Eq.(1.26), without loss of generality, we can choose the N intertwining operators $\hat{\eta}_m$ to be Hermitian.

This analysis of constants of motion is not only valid for static \mathcal{PT} -symmetric Hamiltonians, but can be generalized to time-periodic (Floquet) \mathcal{PT} -symmetric Hamiltonians [16], [38]–[41]. When $H_{\text{PT}}(t) = H_{\text{PT}}(t + T)$ is periodic in time, the long-time dynamics of the system is governed by the Floquet time-evolution operator [42]

$$G_F(T) = \mathbb{T}e^{-i \int_0^T H_{\text{PT}}(t') dt'}, \quad (1.34)$$

where \mathbb{T} stands for the time ordered product that takes into account non-commuting nature of the Hamiltonians at different times. The (stroboscopic) dynamics of the system at times

$t_m = mT$ is then given by $|\psi(t_m)\rangle = G_F^m |\psi(0)\rangle$, and the corresponding, Hermitian, conserved operators $\hat{\eta} = \hat{\eta}^\dagger$ are determined by us [37], [41]

$$G_F^\dagger \hat{\eta} G_F = \hat{\eta}. \quad (1.35)$$

Vectorization of Eq.(1.35) implies the conserved quantities are given by eigenvectors with unit eigenvalue of the ‘‘Floquet Liouville time-evolution’’ matrix

$$\mathcal{G} = G_F^T \otimes G_F^\dagger \quad (1.36)$$

Furthermore, the transformation properties of $G_F(T) \rightarrow G_F(T + t)$ (recall Eq. 1.14) and the conserved operators $\hat{\eta}$ are related. When the periodic Hamiltonian is Hermitian, i.e. $H_0(t_0) = H_0^\dagger(t) = H_0(t_0 + T)$, shifting the zero of time to t_0 leads to a unitary transformation,

$$G_F(T + t_0, t_0) = U(t_0) G_F(T) U^\dagger(t_0), \quad (1.37)$$

where $U(t_0) = \mathbb{T} e^{-i \int_0^{t_0} H_0(t') dt'}$ and therefore the conserved operators are also transformed by the same unitary operator. However, in our case, Eq.(1.37) becomes a *similarity transformation*,

$$G_F(T + t_0, t_0) = S G_F(T) S^{-1} \quad (1.38)$$

where $S = \mathbb{T} \exp(-i \int_0^{t_0} H_{\text{PT}}(t') dt')$ does not satisfy $S^\dagger S = \mathbb{1} = S S^\dagger$. Under this transformation, the conserved operators change as $\hat{\eta} \rightarrow S^{-1\dagger} \hat{\eta} S^{-1}$. This non-unitary transformation of the conserved quantities under a shift of zero of time suggests that they are not related to ‘‘symmetries’’ of the open system with balanced gain and loss.

1.4 \mathcal{PT} -symmetry in optics

We now switch our attention to the experimental side of \mathcal{PT} -symmetry. In order to observe \mathcal{PT} transitions, optics has been an accessible tool for observing these effects of \mathcal{PT} -symmetric quantum systems experimentally, although it can be a challenging task. Nonetheless, the possibility to implement \mathcal{PT} -symmetry can be done with the propagation of light in

optical systems such as coupled waveguides arrays [43], [44]. With some engineering of materials one can have a set of complex potentials by introducing positive and negative imaginary parts in the refractive index. This is achievable because the scalar form of Maxwell's wave equation, under paraxial approximation, yields the Schrödinger equation. As we will see in this section, even though this is a pure classical setting, it captures the essence of a quantum system with balanced gain and loss.

Let us consider the following Maxwell's equations in a homogeneous material with no charge or current densities;

$$\begin{aligned}\nabla \times \vec{E} &= -\frac{\partial \vec{B}}{\partial t} \\ \nabla \times \vec{B} &= \mu\epsilon \frac{\partial \vec{E}}{\partial t} = \frac{n(x, y, z)^2}{c^2} \frac{\partial \vec{E}}{\partial t}\end{aligned}\tag{1.39}$$

Here, \vec{E} and \vec{B} are the electric and magnetic fields, μ and ϵ are the permittivity and permeability, and $n(x, y, z)$ is the refractive index profile of the material. With this we can derive the wave equation of the electric field,

$$\nabla \times \nabla \times \vec{E} = -\frac{n^2}{c^2} \frac{\partial^2 \vec{E}}{\partial t^2}\tag{1.40}$$

Using the identity,

$$\nabla \times \nabla \times \vec{E} = \nabla(\nabla \cdot \vec{E}) - \nabla^2 \vec{E}\tag{1.41}$$

Using the fact that $\nabla \cdot \vec{E} = 0$, Eq. 1.40 is simplified to,

$$\nabla^2 \vec{E} = -\frac{n^2}{c^2} \frac{\partial^2 \vec{E}}{\partial t^2}\tag{1.42}$$

The solution for the above equation can be written as follows, assuming that the propagation of the wave is in the z -direction,

$$\vec{E}(x, y, z, t) = \vec{u}(x, y, z)e^{i(kz - \omega_0 t)}.\tag{1.43}$$

Here we define $k = n_0 k_0$ where the wavenumber $k_0 = \omega_0/c = 2\pi/\lambda$ for incident light of wavelength λ and n_0 is the effective refractive index of cladding. Substituting Eq. 1.43 in Eq. 1.42 we obtain,

$$\begin{aligned} & \left(\frac{\partial^2}{\partial x^2} + \frac{\partial^2}{\partial y^2} + \frac{\partial^2}{\partial z^2} + 2ik \frac{\partial}{\partial z} - k^2 \right) \vec{u} = - \frac{n^2 \omega_0^2}{c^2} \vec{u} \\ \implies & \left(\nabla_T^2 + \frac{\partial^2}{\partial z^2} + 2ik \frac{\partial}{\partial z} + k_0^2 (n^2 - n_0^2) \right) \vec{u} = 0 \end{aligned} \quad (1.44)$$

where $\nabla_T^2 = \partial^2/\partial x^2 + \partial^2/\partial y^2$. This is now reduced down to the Helmholtz equation.

We now impose that the electric field in the propagation direction is slowly varying, also known as SVEA (slowly varying envelope approximation), i.e.;

$$\left| \frac{\partial^2 \vec{u}}{\partial z^2} \right| \ll \left| 2k \frac{\partial \vec{u}}{\partial z} \right|. \quad (1.45)$$

For small enough refractive index contrast (i.e. $(n - n_0)/n_0 \sim 10^{-4}$), we can approximate $(n^2 - n_0^2)/n_0 \approx 2(n - n_0) = 2\Delta n$. Therefore we get,

$$\left(-\frac{1}{2k} \nabla_T^2 - \Delta n \right) \vec{u} = i \frac{\partial \vec{u}}{\partial z}. \quad (1.46)$$

This is called the *paraxial equation*, and indeed it looks similar to the time dependent Schrödinger equation for potential well(s) with depth Δn . The width and the depth of a single well is chosen appropriately to get a single eigenmode. Notice that the partial derivative with respect to time is replaced by the propagation direction z . Now considering the analogy to the Schrödinger equation, let us define an evolution operator. This can be written as

$$\begin{aligned} G &= e^{-i\widehat{H}z} \\ \text{where } \widehat{H} &= -\frac{1}{2k} \nabla_T^2 - \Delta n. \end{aligned} \quad (1.47)$$

1.4.1 Beam Propagation method

This description of a quantum system in a classical framework is a remarkable correspondence and therefore allows us to study discrete single particle quantum systems experimentally. In order to numerically model these systems in settings like coupled waveguide arrays we use a computational technique called the *Finite Difference-Beam Propagation Method* (FD-BPM) [45].

For simplicity we assume that the variation in the refractive index of a waveguide and the intensity profile of the input beam incident is only in one dimension. Therefore the refractive index is $n(x) = n_s + \Delta n(x) \pm in_I(x)$, where n_s is the index of the substrate or cladding ($n_s = 1.4500$), $\Delta n(x)$ is the contrasting index of the core of the waveguide ($\Delta n_s \sim 5 \times 10^{-4}$), and n_I represents the imaginary refractive index to be introduced as gain-loss potentials on parity symmetric sites ($n_I \sim 10^{-6}$). The envelope function is therefore $\vec{u}(x, z) = u(x, z)\hat{y}$ with the direction of propagation along the z-axis.

The continuous variables x, z are made discrete and hence the envelope function is written as $u(x_i, z_j) \equiv u(i\Delta x, j\Delta z)$ with $i = 0, 1, \dots, N_x - 1$ and $j = 0, 1, \dots, N_z - 1$. The 2nd order differential operator, written in the 3-point symmetric form, as;

$$\frac{\partial^2 u(x_i, z_j)}{\partial x^2} = \frac{u(x_{i-1}, z_j) - 2u(x_i, z_j) + u(x_{i+1}, z_j)}{\Delta x^2} \quad (1.48)$$

We can represent this differential operator as a matrix product in the following way;

$$\begin{aligned} \frac{\partial^2 u(x_i, z_j)}{\partial x^2} &\rightarrow \frac{1}{\Delta x^2} \begin{bmatrix} -2 & 1 & & 0 \\ 1 & \ddots & \ddots & \\ & \ddots & \ddots & 1 \\ 0 & & 1 & -2 \end{bmatrix} \begin{bmatrix} u(x_0, z_j) \\ u(x_1, z_j) \\ \vdots \\ u(x_{N_x-1}, z_j) \end{bmatrix} \\ &= \left[\frac{M}{\Delta x^2} \right] \mathbf{U}(x, z_j). \end{aligned} \quad (1.49)$$

Here we define $U(x, z_j)$ as the column vector representing the beam profile in the x-direction. Note that, we make use of open boundary conditions that requires the elements $u(x_{-1}, z_j)$ and $u(x_{N_x}, z_j)$ to be zero. The operator \widehat{H} from Eq. 1.47 can be rewritten as;

$$\widehat{H} = -\frac{1}{2k} \left[\frac{M}{\Delta x^2} \right] - \mathbb{1} \Delta n(x) \quad (1.50)$$

where $\mathbb{1}$ is the identity matrix of size $N_x \times N_x$ and $\Delta n(x)$ is the refractive index contrast represented as a column matrix. We now have an expression for the evolution operator in the form of a matrix which needs to be calculated only once in the case where the refractive index does not change in the propagation direction. Therefore,

$$U(x, z_{j+1}) = e^{i\widehat{H}\Delta z} U(x, z_j). \quad (1.51)$$

Recall that the paraxial equation (Eq. 1.46) had a 1st order derivative of $u(x, z)$ with respect to z . Using forward difference, Eq. 1.51 can be discretized as,

$$\frac{u(x_i, z_{j+1}) - u(x_i, z_j)}{\Delta z} = -i\widehat{H}u(x_i, z_j) \quad (1.52)$$

$$\therefore U(x, z_{j+1}) = (\mathbb{1} - i\widehat{H}\Delta z)U(x, z_j). \quad (1.53)$$

This is called the explicit scheme. Although simplified for numerical calculations, the expression is unstable for large Δz . For this reason, we also consider the backward difference of the derivative (called the implicit scheme),

$$\frac{u(x_i, z_{j+1}) - u(x_i, z_j)}{\Delta z} = -i\widehat{H}u(x_i, z_{j+1}) \quad (1.54)$$

Adding the two schemes, essentially gives a half-step propagator, defined below, which fixes the instability problem;

$$K_{\pm} = \mathbb{1} \pm i\Delta z \widehat{H} / 2. \quad (1.55)$$

Hence, for a full step of Δz ,

$$U(x, z_{j+1}) = K_+^{-1} K_- U(x, z_j). \quad (1.56)$$

The finite difference discretization of this kind is called the Crank-Nicholson scheme and serves as a sufficiently powerful tool to numerically simulate beam propagation.

In Fig. 1.6, we show an example of the BPM calculation for a system of two coupled waveguides. Let the waveguides be labeled WG1 and WG2. Keeping in mind the \mathcal{PT} -symmetric dimer case discussed in Sec. 1.2, we used the following parameters for the simulations. Consider a light beam of wavelength $\lambda = 630 \text{ nm}$ injected in WG1 centered at $x = -10 \mu\text{m}$. We define the 1D envelope function of this beam as $U(x, z) \equiv e_1$, which is the normalized eigenmode of WG1. We also define, ‘ e_2 ’, the normalized eigenmode of WG2. With this, we define the intensities of light in each of the waveguides, at a distance z , as the square of the projected weight of $U(x, z)$ on the eigenmodes of individual waveguides. In the language of quantum mechanics we can write this as, $|E_1|^2 = |\langle U | e_1 \rangle|^2$ and $|E_2|^2 = |\langle U | e_2 \rangle|^2$ respectively. Each waveguide has a width $5 \mu\text{m}$ with edges separated by $15 \mu\text{m}$. The distance between waveguides is chosen such that the overlap of the eigenmodes ‘ e_1 ’ and ‘ e_2 ’ is significantly small as compared to the intensity of each mode.

Fig. 1.7 shows this variation as the separation between the waveguides increase. As seen this overlap decreases exponentially with the separation. This needs to be small enough to treat the eigenmodes as solutions to the paraxial equation (Eq. 1.46) for a single waveguide. This is analogous to the wavefunction of a particle localized in one of the site in the tight binding model.

The substrate refractive index is $n_s = 1.45$ while the core refractive index is $n_c = 1.4505$. The figure shows four case each for a different value of n_I . In each panel of Fig. 1.6, the top image, shows the electric field intensity $|U(x, z)|^2$ of the beam as it evolves in the transverse z direction. The bottom sub-panel, plots show variation in the transverse direction of the normalized intensities $|E_{\text{norm}}|^2$ in WG1 (shown in blue), WG2 (shown in red) and the total intensity in both (black). Panel (a) shows the Hermitian case with $n_I = 0$. In panel (b), the magnitude of the complex refractive index is $n_I = 2.658 \times 10^{-6}$. Notice the total normalized

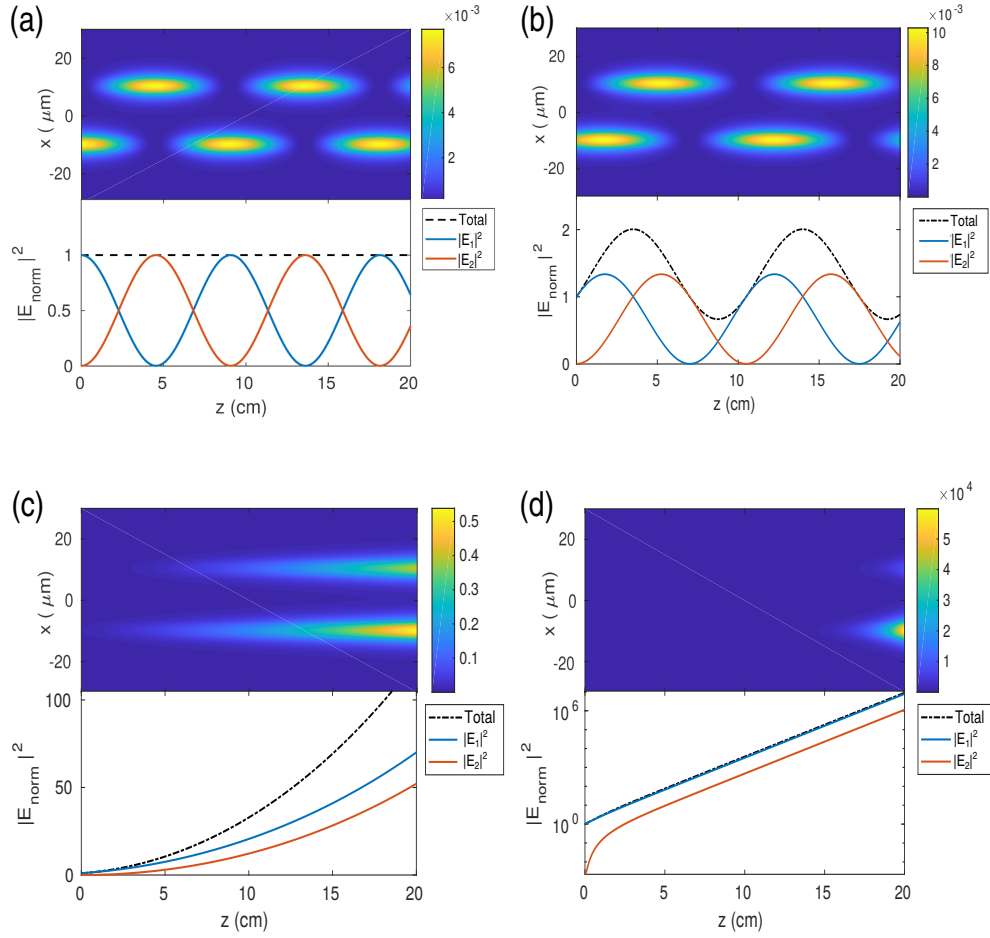


Figure 1.6. Beam Propagation results for a pair of evanescently coupled waveguides of width $5\mu m$ separated by $15\mu m$. The incident light has a wavelength of 630 nm . The core refractive index is 1.4505 and the cladding refractive index is 1.4500 . Panel (a) shows the Hermitian case with $n_I = 0$. In panel (b), $n_I = 2.658 \times 10^{-6}$. Panel (c) show the region of broken \mathcal{PT} -symmetry with the imaginary refractive index as $n_I = 5.316 \times 10^{-6}$ and panel (d) with $n_I = 7.974 \times 10^{-6}$ the intensity increases exponentially (lower sub-panel logscale in y).

intensity is bounded but greater than 1. This signifies the \mathcal{PT} -symmetric region. Panels (c) and (d), with n_I equal to 5.316×10^{-6} and 7.974×10^{-6} respectively, show unbounded growth in the intensity signifying that the \mathcal{PT} -symmetry in the system is broken.

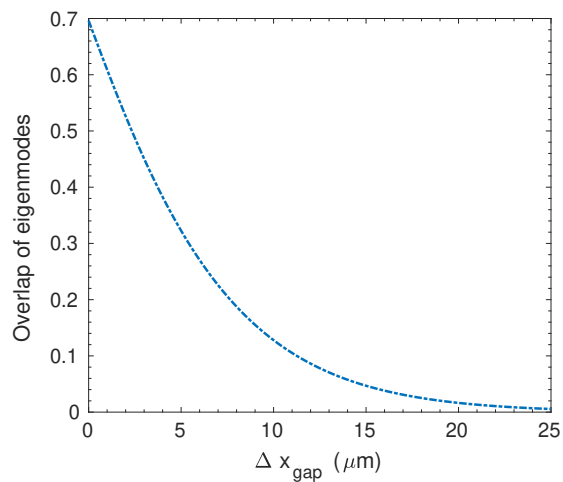


Figure 1.7. Variation of the overlap of individual eigenmodes, $|\langle e_1|e_2\rangle|$, of the two coupled waveguides as a function of their separation Δx_{gap} .

In the next chapter, we theoretically investigate the fate of the \mathcal{PT} -symmetry breaking threshold, keeping in mind an experimental setup of coupled waveguide arrays with one pair of spatially separated, balanced gain-loss potentials.

2. \mathcal{PT} -SYMMETRIC LATTICE MODELS

The content of this chapter is a parts of two of our papers which have been slightly modified. These papers have been published in APS Physical Review A.

Before we dive into what \mathcal{PT} -symmetric lattice models are, it is important for us to understand some key properties of a simple lattices. Lattice models are designed to investigate properties such as electron transport in materials or to determine their electronic band structure, although as we will see, is not limited to condensed matter systems. Tight binding models have widely been used due to their simplicity and accuracy in describing a large number of systems in condensed matter, ultra cold atoms and photonic lattices. The underlying idea is to use the discretization the system to solve the single particle non-interacting Schrodinger equation. Although doing so can be analytically difficult if the lattice structure in non-uniform or has impurities, but can solved numerically much more easily. One very versatile and powerful technique is the tight-binding model.

2.0.1 Energy spectrum of a tight binding lattice

Let us consider the simplest model of an arrangement of atoms forming a 1D lattice with an electron moving through it. These “nearly free” electrons have a uniform hopping probability of J to jump from one atom to the next. Note that the motivation in using a crystal and an electron is only due to its historical significance: this tight binding model was used to explain electronic properties of crystals. We will generically refer to the discretely positioned atoms of the crystal as sites of a lattice and the electron as a particle. For a more mathematically rigorous description, we recall our friend, the Hamiltonian. The goal is to construct a Hamiltonian description of a system and solve the Schrödinger equation. For this, we first assume that a particle localized at site n will be represented by $|n\rangle$. This serves as our eigenvector basis. The energy of such a particle is $\epsilon_n = \langle n|H_0|n\rangle$, where H_0 is the Hamiltonian of this system. Another assumption we impose is that the particle is only

allowed to hop to its nearest neighbour with a probability of $J = \langle n|H_0|n+1\rangle$. So this single particle Hamiltonian with N sites can be written as:

$$H_0 = \sum_{n=1}^N \epsilon_n |n\rangle \langle n| - \sum_{n=1}^N J_n |n\rangle \langle n+1| = H_0^\dagger, \quad (2.1)$$

where $\epsilon_n = \epsilon_0$ and $J_n = J$ for all $n \in [1, N]$ due to uniformity.

Since we have N sites in our lattice (typically we assume that $N \rightarrow \infty$), we form an ansatz to describe a particle in such a lattice as a linear combination of plane wave solutions in site basis:

$$|\psi_n\rangle = A \sum_{n=1}^N c_n |n\rangle, \quad (2.2)$$

where k is the quasi momentum, A is the normalization constant and $c_n = e^{-ikn}$ are the amplitudes of finding the particle on site n ¹. Evaluating the Schrodinger equation, the dispersion relation is calculated to be,

$$E(k) = \epsilon_0 - 2J \cos k \quad (2.3)$$

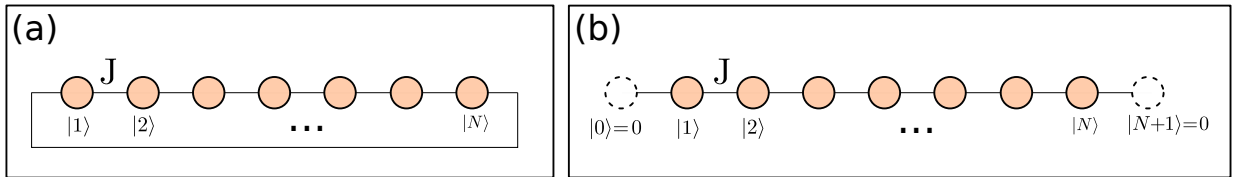


Figure 2.1. Schematic of a lattice with (a) Open boundary condition, (b) Periodic boundary condition.

Fig. 2.1 shows the schematics of lattices with two different boundary conditions. Panel (a) is when the last site is coupled to the first site. With this condition the model represents an infinite lattice with translational invariance. This type can help in understanding lattices which are in the shape of a ring. In this case, from the boundary condition ($e^{-ik(N)} = e^{-ik(0)} = 1$), one can easily calculate the quasi-momentum to be $k = 2p\pi/N$ where $p \in [1, N]$ denotes the energy level index. The normalization constant is $A = \frac{1}{\sqrt{N}}$. Panel (b) shows the

¹↑The tight binding model is also known as Linear Combination of Atomic Orbitals (LCAO) for this reason.

schematic for a lattice with open boundary conditions. Here the model represents a more realistic scenario since materials have edges where the probability of finding a particle outside is zero, (unless of course there exists a coupling between the environment and the boundary). Most of the lattice examples we deal with in this thesis will possess open boundary conditions. Here we find that $e^{-ik(N+1)} = e^{-ik(0)} = 0$, resulting in the quasi-momentum to be $k = p\pi/(N + 1)$ where again $p \in [1, N]$ denotes the energy level index. The normalization constant in this case is $A = \sqrt{\frac{2}{N+1}}$ Fig. 2.2(a) show a typical energy dispersion plot for a

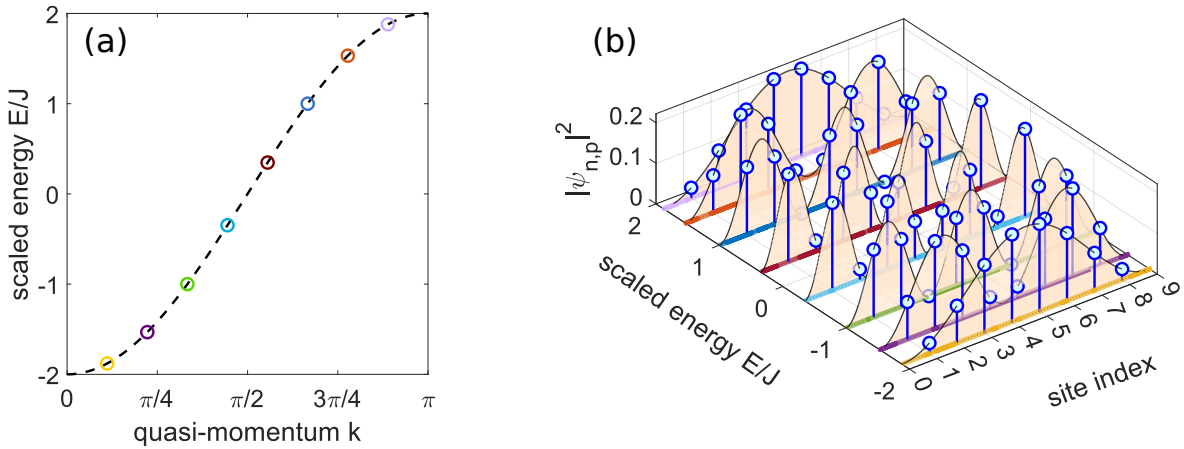


Figure 2.2. (a) Dispersion relation of a tight binding lattice with nearest neighbour coupling J and $\epsilon_0 = 0$ (b) Probability distribution of eigenstates of a single particle Hamiltonian describing a tight binding lattice with $N = 8$ sites and open boundary condition. Note that the energy axis is independent of the site index and is only there to label the eigenstate to its corresponding energy eigenvalue.

uniform tight binding lattice with $N = 8$ sites and $\epsilon_0 = 0$. Panel (b) shows the probability distribution, $|\psi_{n,p}|^2$ of all the eigenstates which due to open boundary conditions simplifies to:

$$|\psi_{n,p}\rangle = \sqrt{\frac{2}{N+1}} \sum_{n=1}^N \sin\left(\frac{p\pi n}{N+1}\right) |n\rangle \quad (2.4)$$

We shall now explore some tight binding lattice where specific sites interact with the environment and calculate the \mathcal{PT} symmetry breaking points for these systems in one and two dimensions. These models have been a playground for many researchers studying non-

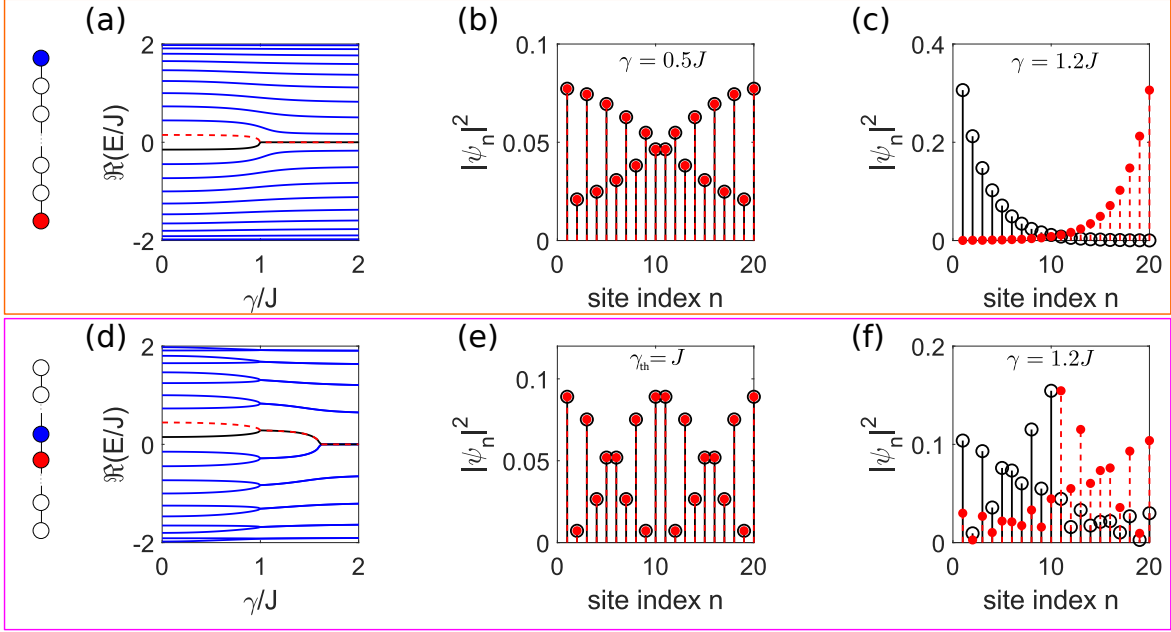


Figure 2.3. 1D chain : Plots of the eigenspectrum flow for a lattice of $N = 20$ sites as a function of the non-Hermiticity strength γ/J with the gain-loss sites at the (a) edges i.e. $m_0 = 1$ along with the eigenstates of the Hamiltonian participating in the breaking of \mathcal{PT} -symmetry when (b) $\gamma = 0.5J$ and (c) $\gamma = 1.2J$. (c) As the γ/J is increased beyond the \mathcal{PT} -threshold ($\gamma_{th} = J$) the eigenstate distribution no longer possess parity symmetry. A schematic is provided on the left. (d) This is the eigenspectrum flow for when the gain-loss sites are closest to each other i.e. $m_0 = 10$. (e) One such pair is presented here when $\gamma_{th} = J$ with the feature that not only they have the same eigenvalue but their probability distributions overlap completely. (f) As the non-Hermiticity is increased to $\gamma = 1.2J$ the states with their broken parity symmetry are anti-symmetric to each other.

Hermitian open quantum systems as they offer a numerically solvable simple representation of the \mathcal{PT} -symmetric Hamiltonian.

2.1 Non-Hermitian \mathcal{PT} -symmetric chains

Let us recall the Hermitian Hamiltonian from Eq. 2.1 that describes a system of N sites with constant couplings J . We now introduce a non-Hermitian potential of the following form:

$$\Gamma(m_0, \gamma) = i\gamma(|m_0\rangle\langle m_0| - |\bar{m}_0\rangle\langle \bar{m}_0|) = -\Gamma^\dagger, \quad (2.5)$$

where m_0 is the site of with a $+i\gamma$ potential and $\bar{m}_0 = N + 1 - m_0$ has a $-i\gamma$ potential, with γ denoting the strength of the non-Hermiticity. The new Hamiltonian $H(m_0, \gamma) = H_0 + \Gamma$ is non-Hermitian but \mathcal{PT} -symmetric. We define the linear parity operator by its action on a state as $\mathcal{P}|n\rangle \rightarrow |N + 1 - n\rangle$ and anti-linear time reversal operator as : $\mathcal{T} : |n\rangle \rightarrow |n\rangle^*$ where $*$ is the complex conjugation operator.

Introducing a complex potential like this means that the norm of the system is not preserved. The system's interaction with the environment is special since the $\pm i\gamma$ on reflection symmetric sites represents *balanced* gain and loss. This is special because of the following reason. When $\gamma = 0$, the Hamiltonian is Hermitian. As the gain-loss strength is increased, the eigenvalues of the $H(\gamma)$ are real and their corresponding eigenstates are simultaneous eigenstates of the \mathcal{PT} operator until $\gamma = \gamma_{th}$, where γ_{th} is called the \mathcal{PT} breaking threshold. At this point depending on whether N is even or odd and the relative position of the gain-loss sites, the two or three levels coalesce. On increasing γ more than the threshold, the symmetry is broken and two eigenstates have complex eigenvalues.

Fig. 2.3 exactly depicts this change from closed to open system behaviour for two lattices with $N = 20$ sites, first (a)-(c) when $m_0 = 1$ and then (d)-(f) when $m_0 = 10$. The plot in panel (a) shows the flow of the eigenspectrum as a function of the non-Hermiticity γ/J . Panel (b) shows the eigenstates of the Hamiltonian participating in the breaking of \mathcal{PT} -symmetry when $\gamma = 0.5J$ and clearly shows that the states are invariant under parity. (c) Beyond the threshold for $\gamma = 1.2J$, the eigenstate distribution no longer possess parity symmetry. This is the region of broken \mathcal{PT} -symmetry. In panel (d), the eigenspectrum flow for when the gain-loss sites are closest to each other i.e. $m_0 = 10$. This is a special case because at the \mathcal{PT} breaking threshold, all the states participate in the symmetry breaking as consecutive states coalesce producing $N/2$ 2^{nd} order exceptional points. [46]. (e) One such pair is presented here when $\gamma_{th} = J$ with the feature that not only they have the same eigenvalue but their probability distributions overlap completely. (f) As the non-Hermiticity is increased to $\gamma = 1.2J$ the states with their broken parity symmetry are anti-symmetric to

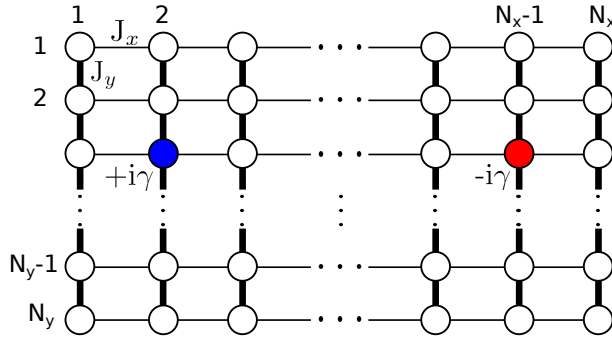


Figure 2.4. Schematic of a \mathcal{PT} symmetric chain with N_x sites, strongly coupled to $N_y - 1$ Hermitian chains of the same length. The gain site (blue) has a potential $+i\gamma$ and its parity-symmetric site (red) has the loss potential $-i\gamma$. The coupling within a chain is J_x and the inter-chain coupling is J_y .

each other². It is worth mentioning that when the lattice has an odd number of sites, the \mathcal{PT} breaking threshold when $m_0 = N/2$, $\gamma_{th} \rightarrow J/2$ as $N \rightarrow \infty$.

A feature of \mathcal{PT} symmetric models with one pair of gain-loss potentials is that the \mathcal{PT} breaking threshold is proportional to the tunneling amplitude. In principle, the threshold is increased by reducing the distance between the gain and loss sites. Similarly, the \mathcal{PT} transition threshold is, in principle, increased by making the gain and loss sites closer to each other. Although in practice, the different physical machinery necessary to implement loss in one and gain in the other put serious constraints on the minimum separation between the two sites.

So the question is whether the \mathcal{PT} -threshold can be enhanced beyond $\gamma_{th}/J = 1$. We now show that when strongly coupling the \mathcal{PT} symmetric chain to a large number of neutral chains, the \mathcal{PT} symmetry breaking threshold increases by a factor proportional to the total number of coupled chains. The results obtained in this section are a part of the paper we have published [47].

2.1.1 Strongly coupled chains

Let us now construct a two-dimensional, finite, tight binding lattice with N_x sites along the x -direction, N_y sites along the y -direction, and open boundary conditions as shown in Fig. 2.4. J_x and J_y denote the nearest-neighbor couplings along the two directions respectively. The gain site potential $+i\gamma$, is located at (m_0, n_0) while the loss potential $-i\gamma$, is at reflection-symmetric location (\bar{m}_0, n_0) with $\bar{m}_0 = N_x + 1 - m_0$. We can write the Hamiltonian for this system as $H_{PT} = H_0 + \Gamma$, where the Hermitian tight-binding part and the non-Hermitian part are given by

$$H_0 = -J_x \sum_{m,n} (|m, n\rangle \langle m+1, n| + \text{h.c.}),$$

$$-J_y \sum_{m,n} (|m, n\rangle \langle m, n+1| + \text{h.c.}), \quad (2.6)$$

$$\Gamma = +i\gamma (|m_0, n_0\rangle \langle m_0, n_0| - |\bar{m}_0, n_0\rangle \langle \bar{m}_0, n_0|), \quad (2.7)$$

where $|m, n\rangle$ denotes a state localized at lattice site (m, n) . The parity operator is given by $\mathcal{P} : (m, n) \rightarrow (\bar{m}, n)$ and time reversal operator is defined by $\mathcal{T} = *$. We find the eigenvalues and eigenvectors of $H_0(J_x, J_y)$ to be,

$$\Psi_{p,q}(m, n) \equiv \langle m, n | k_p, k_q \rangle = A \sin(k_p m) \sin(k_q n), \quad (2.8)$$

$$E_{p,q} = -2J_x \cos k_p - 2J_y \cos k_q, \quad (2.9)$$

where $k_p = p\pi/(N_x + 1)$ and $k_q = q\pi/(N_y + 1)$ are the dimensionless quasimomenta consistent with open boundary conditions, $1 \leq p \leq N_x$, $1 \leq q \leq N_y$, and the normalization constant is given by $A = 2/\sqrt{(N_x + 1)(N_y + 1)}$.

In this project, we focused on the strongly coupled chains, i.e. $J_y/J_x \gg 1$. In this limit, the spectrum in Eq.(2.9) has N_y energy bands, with each band comprising N_x eigenvalues spread over a width $\sim 4J_x$. Therefore, in the following, we will use the label p to denote the level index within a band and q to denote the band index. This separation of the spectrum

²↑It is often thought that the symmetry of the \mathcal{PT} -symmetric Hamiltonian breaks is misleading since the symmetry of the Hamiltonian is independent of γ/J . A more accurately, beyond the threshold the eigenstates of the Hamiltonian are no longer simultaneous eigenstates of the \mathcal{PT} operator. This can be seen in Fig. 2.3

into bands and levels within a band is valid when the bands do not overlap, and we will consider chains where this criterion is satisfied.

2.1.2 Numerical calculation of the \mathcal{PT} threshold

The results we obtain for $\gamma_{\text{th}}(m_0, n_0)$ are found by exact diagonalization of the \mathcal{PT} -symmetric Hamiltonian, $H_{\mathcal{PT}}$. Figure 2.5 shows the behavior of γ_{th} as a function of the relative gain position $\mu = 2m_0/N_x$ when the gain site is on the top chain, i.e. $n_0 = 1$. These results are for $J_y/J_x = 20$. Panel (a) shows the results for an even chain with $N_x = 26$ sites. When the number of chains is $N_y = 1$, the threshold shows the characteristic U-pattern as a function of location of the gain site [48]. When the number of chains increases to $N_y = \{6, 13\}$, the maximum value of the threshold increases monotonically with it. Recall that this maximum occurs when the gain-loss potentials are farthest apart, i.e. $m_0 = 1$, or nearest neighbors, i.e. $m_0 = N_x/2$. The maximum threshold $\gamma_{\text{th}}(m_0 = 1)/J_x$ scales linearly with the number of horizontal chains N_y up to a point, $N_y \lesssim 15$. These results are valid for all strongly coupled chains with an even number of lattice sites.

Figure 2.5(b) shows the results for an odd, $N_x = 27$ lattice with $J_y/J_x = 20$ and relative gain position $\mu = 2m_0/(N_x - 1)$. For a single chain, the threshold $\gamma_{\text{th}}(m_0)$ shows the characteristic U-shape where the threshold for the nearest gain-loss location, $m_0 = (N_x - 1)/2$, is half of that for the farthest gain and loss, $m_0 = 1$ [48]. As the number of chains N_y is increased, the threshold $\gamma_{\text{th}}(m_0)$ increases in a proportionate manner. Fig. 2.5(d) shows the linear dependence of the largest threshold $\gamma_{\text{th}}(m_0 = 1)/J_x$ on the number of chains. When $N_y \gtrsim 14$ this linear relationship breaks down, as it does in Fig. 2.5(b). These results are valid for all strongly coupled chains with an odd number of lattice sites.

Notice that in Figs. 2.5, panels (b) and (d) the scaling of the \mathcal{PT} threshold breaks down as N_y is increased. This breakdown is due to the finite values of J_y/J_x used in the calculations. We find that the scaling is only valid in the “strong coupling” regime which we defined by enforcing that the energy bands do not overlap. We were able to calculate that for a large

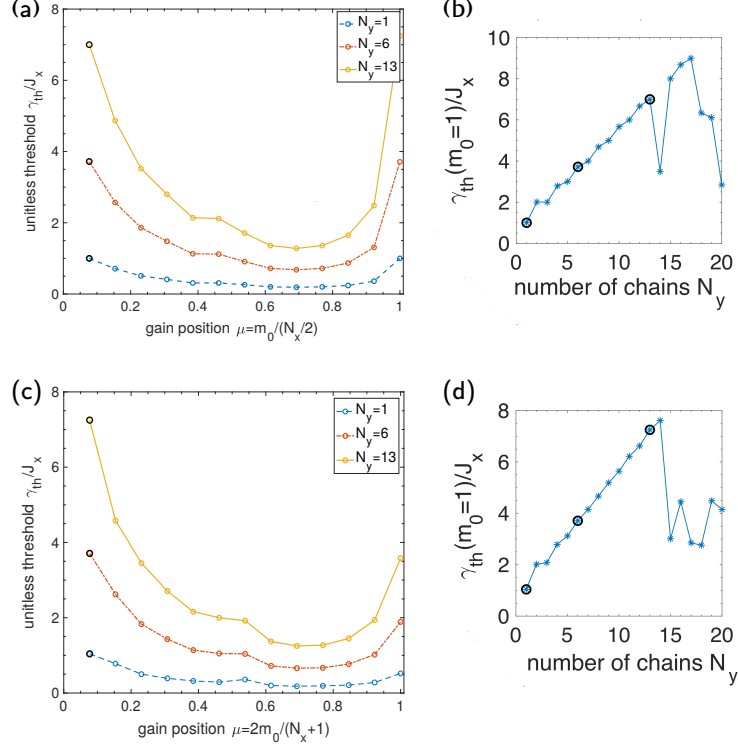


Figure 2.5. Dependence of the \mathcal{PT} -breaking threshold $\gamma_{\text{th}}(m_0)/J_x$ on the relative gain position $\mu = 2m_0/N_x$ and the number of horizontal chains N_y for (a) even lattice with $N_x = 26$ and (c) odd lattice with $N_x = 27$. The couplings are $J_y/J_x = 20$. For a single chain, $\gamma_{\text{th}}(m_0)$ shows the characteristic U-shape. As N_y is increased, the \mathcal{PT} -threshold increases as well. The graphs in panel (b) and (d) show that the maximum value of the threshold, found for $m_0 = 1$, increases linearly with the number of chains.

number of chains $N_y \gg 1$, in the strong coupling limit, the \mathcal{PT} breaking threshold for N_y coupled chains is strongly renormalized. For open boundary conditions, Fig. 2.5, we get

$$\lim_{N_y \gg 1} \gamma_{\text{th}}(m_0, N_y) = \left(\frac{N_y + 1}{2} \right) \gamma_{\text{th}}(m_0, N_y = 1), \quad (2.10)$$

2.1.3 Results for small systems

Let us now consider some experimentally accessible system sizes with 2-3 chains, i.e. $N_y = \{2, 3\}$, and with two or three sites in each chain, $N_x = \{2, 3\}$, and small to moderate

coupling ratio $J_y/J_x \sim O(1)$. Fig. 2.6(a) shows a gain-loss dimer (strongly) connected to a neutral dimer. The 4×4 Hamiltonian for such a system is given by

$$H_4(\gamma) = (-J_x\sigma_x + i\gamma\sigma_z) \otimes \mathbf{1}_2 + \mathbf{1}_2 \otimes (-J_y\sigma_x). \quad (2.11)$$

It is straightforward to obtain the particle-hole symmetric eigenvalues

$$\lambda_k = \pm \left[J_x^2 + J_y^2 - \frac{\gamma^2}{2} \pm \frac{1}{2} \sqrt{\gamma^4 + 16J_x^2J_y^2 - 4\gamma^2J_y^2} \right]^{1/2}. \quad (2.12)$$

The \mathcal{PT} transition threshold γ_{th}/J_x can be analytically obtained from Eq.(2.11). Depending on the ratio J_y/J_x the pair of eigenvalues, among the four given in Eq.(2.12), that drive the \mathcal{PT} breaking transition varies. This variation gives rise to the three distinct functional forms for the threshold function $\gamma_{\text{th}}(J_y)$ seen in Fig. 2.6(a). In a similar spirit, we also consider a \mathcal{PT} dimer connected to two neutral dimers, and a \mathcal{PT} trimer connected to one or two neutral trimers.

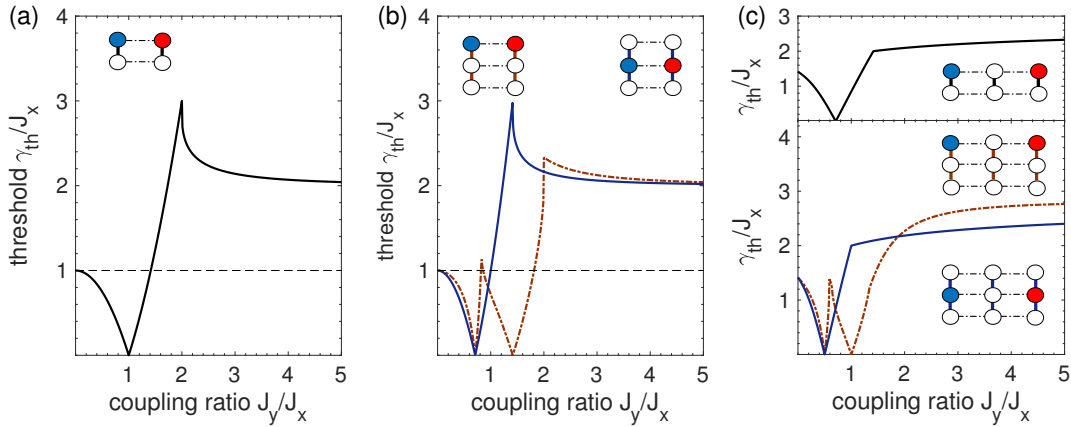


Figure 2.6. \mathcal{PT} threshold dependence on coupling to neutral sites shown by blank circles; the gain-site is shown in blue and the loss-site is shown in red. (a) γ_{th}/J_x for a \mathcal{PT} -neutral dimer system is tripled from its single-dimer value when $J_y/J_x = 2$, and saturates to two in the strong coupling limit, $J_y/J_x \gg 1$. (b) for three dimers, the threshold is more than doubled near $J_y/J_x \sim 2$ and saturates to two for $J_y/J_x \gg 1$. Corresponding results for a (c) \mathcal{PT} -neutral trimer system, and (d) a three-trimers system. In all cases, the threshold is more than doubled even at moderate values of $J_y/J_x \gtrsim 2$.

Figure 2.6(a) schematically shows the dependence of the threshold γ_{th}/J_x on the ratio of coupling strengths J_y/J_x for a \mathcal{PT} -neutral dimer system. Starting from unity, the dimensionless threshold γ_{th}/J_x decreases to zero for the symmetrical configuration, i.e. $J_y = J_x$, but then rises rapidly to three when $J_y = 2J_x$. As the asymmetry increases, $J_y/J_x \gg 1$, the threshold saturates to two. Results for one \mathcal{PT} dimer with two neutral dimers are shown in panel (b). When the \mathcal{PT} dimer is in the middle, the threshold is first suppressed to zero, and then rises to three when $J_y/J_x = \sqrt{2}$ (solid blue line). In contrast, when the \mathcal{PT} dimer is on top, the threshold vanishes at two different coupling strengths, and reaches a maximum near $J_y/J_x = 2$ (dot-dash red line). In both configurations, the threshold saturates to $\gamma_{\text{th}}/J_x = 2$ in the strong coupling limit.

Figures 2.6(c) shows the corresponding results for a \mathcal{PT} trimer. When connected to another neutral trimer (top panel), the threshold γ_{th}/J_x first decreases down to zero, then increases, and saturates to $\gamma_{\text{th}}/J_x = 2\sqrt{2} = 2\gamma_{\text{th}}(J_y = 0)$. When we have two neutral trimers (bottom panel), the threshold shows a qualitatively similar behavior. The results in Fig. 2.6 show that the \mathcal{PT} transition threshold in experimentally realizable configurations is dramatically changed by coupling the \mathcal{PT} -dimer or \mathcal{PT} -trimer to neutral sites.

In conclusion, these results show that highly asymmetrical, two-dimensional lattice models, with a few balanced gain and loss sites, give rise to a strong renormalization of the \mathcal{PT} symmetry breaking threshold. These results show an interesting and novel way to change the \mathcal{PT} symmetry breaking thresholds from zero to a factor of two to three times the dimer coupling by simply changing the inter-dimer coupling.

2.2 A brief introduction to topological superconductors

Let us now explore the non-Hermitian version of a model that has received a lot of attention in recent year due to its application to quantum computing. In these sections of this chapter, we investigate the variation of the \mathcal{PT} -symmetry breaking threshold in a celebrated toy model for a topological superconductor called the Kitaev chain model with one pair of gain-loss potentials on reflection symmetric sites. The Kitaev chain is intuitively constructed to host the so-called Majorana fermions. In the past decade there has been a race to observe these elusive particles, because in principle, they could serve as viable and robust candidates for a quantum bit; the building block for a quantum computer. A Majorana particle is, by design, a superposition of Dirac fermions, i.e. a fermion constructed from a electron-hole pair. This superposition is defined such that the particle is its own antiparticle. By this definition, they must have zero energy. Conversely, a Dirac fermion can be assumed to a superposition of two Majorana particles. Since this seems like a mathematical construction, the question is if one can separate these Majoranas far enough to probe them.

One innovative design is done on a finite 1D tight-binding chain that couples the Majorana particles on the nearest neighbor sites. This leaves the Majoranas on the edges uncoupled which are highly localized, robust modes with zero energy of this open chain. Kitaev's model is a way to build a one dimensional p-wave superconductor with topological properties.

2.3 Understanding the Kitaev Hamiltonian

The Kitaev model of a one dimensional, p-wave superconducting chain with N -sites and open boundary conditions is described by the following Hermitian Hamiltonian,

$$\begin{aligned}
 H_0 &= -\mu \sum_{n=1}^N c_n^\dagger c_n - J \sum_{n=1}^{N-1} (c_n^\dagger c_{n+1} + \text{h.c.}) \\
 &+ \sum_{n=1}^{N-1} (\delta e^{i\Phi} c_n c_{n+1} - \text{h.c.}).
 \end{aligned} \tag{2.13}$$

Here c_n^\dagger and c_n are fermionic creation and annihilation operators for site n in the chain, μ is the on-site potential, $J > 0$ is the nearest-neighbor hopping strength, and $\delta > 0$ is the

amplitude of the (p-wave) superconducting coupling for a Cooper pair that is localized across neighboring sites [49].

The fermionic creation and annihilation operators can be written in terms of the Majorana operators as

$$c_n^\dagger = \frac{e^{i\Phi/2}}{2}(a_{2n-1} + ia_{2n}), \quad (2.14)$$

$$c_n = \frac{e^{-i\Phi/2}}{2}(a_{2n-1} - ia_{2n}). \quad (2.15)$$

The Majorana operators satisfy the anticommutator relation $\{a_i, a_j\} = 0$. The global phase, Φ , of the superconducting order parameter is fixed at $\pi/2$ to ensure that Eq.(2.13) is parity-time symmetric, with the parity operator given by $\mathcal{P} : c_n \rightarrow c_{\bar{n}}$ where $\bar{n} = N + 1 - n$ is the mirror-symmetric counterpart of site n and the time-reversal operator is given by complex conjugation, $\mathcal{T} = *$. The Majorana operators follow the anti-commutation relation $\{a_i, a_j\} = 2\Delta_{i,j}$ where $\Delta_{i,j}$ is the Kronecker delta function.

Additionally, the Hamiltonian with the Majorana operators looks like:

$$\begin{aligned} H_0^M &= -\frac{\mu}{2} \sum_{n=1}^N (1 + ia_{2n-1}a_{2n}) - \frac{i}{2} \sum_{n=1}^{N-1} (J + \delta)a_{2n}a_{2n+1} \\ &\quad + \frac{i}{2} \sum_{n=1}^{N-1} (J - \delta)a_{2n-1}a_{2n+2}. \end{aligned} \quad (2.16)$$

Note that for the case $\mu = 0$, $J = \delta$, the Hamiltonian is $H_0^M = -iJ \sum_{n=1}^{N-1} a_{2n}a_{2n+1}$; as a result half of the modes have degenerate energy equal to $+J$ and the other half will have energy $-J$. There remain two unpaired operators, a_1 and a_{2N} , which commute with the Hamiltonian, implying that these modes have zero energy. These are called Majorana zero modes (MZM).

We rewrite Eq.(2.13) by using the Bogoliubov-de Gennes representation in terms of the operator-vector $\Psi = (c_1, c_1^\dagger, c_2, c_2^\dagger \dots c_N, c_N^\dagger)^T$ as $H_0 = \Psi^\dagger H_{\text{BdG}} \Psi$ where the $2N \times 2N$ matrix H_{BdG} in the site-representation, with open boundary conditions, is given by

$$\begin{aligned} H_{\text{BdG}} &= -\frac{\mu}{2} \sum_{n=1}^N |n\rangle \langle n| \otimes \sigma_z \\ &\quad - \frac{J}{2} \sum_{n=1}^{N-1} (|n\rangle \langle n+1| + |n+1\rangle \langle n|) \otimes \sigma_z \\ &\quad + \frac{i\delta}{2} \sum_{n=1}^{N-1} (|n\rangle \langle n+1| - |n+1\rangle \langle n|) \otimes \sigma_x, \end{aligned} \quad (2.17)$$

where σ_x, σ_z are Pauli matrices. For a chain with periodic boundary conditions, translational invariance allows us to transform the site-space Hamiltonian (2.17) into momentum space, $\tilde{H}_{\text{BdG}} = U H_{\text{BdG}} U^\dagger$ with a unitary

$$U = \frac{1}{\sqrt{N}} \sum_{k,n=1}^N e^{-i|p_k\rangle \langle n|} \otimes \left(e^{i\pi/4} \mathbf{1}_2 + e^{-i\pi/4} \sigma_z \right). \quad (2.18)$$

The block-diagonalized momentum-space Hamiltonian is given by $\tilde{H}_{\text{BdG}} = \sum_{k=1}^N h(p_k) |p_k\rangle \langle p_k|$ where $p_k = 2\pi k/N$ are the discrete quasimomenta for a finite chain and

$$h(p) = \begin{pmatrix} -J \cos p - \mu/2 & -i\delta \sin p \\ i\delta \sin p & J \cos p + \mu/2 \end{pmatrix}. \quad (2.19)$$

The bulk energy spectrum of the Hamiltonian \tilde{H}_{BdG} is given by

$$E_\pm(p) = \pm \sqrt{(J \cos p + \mu/2)^2 + \delta^2 \sin^2 p}, \quad (2.20)$$

and it shows that in the limit of an infinite chain, $N \gg 1$, the gap in the spectrum vanishes at $p = \pi$ when $\mu = 2J$. For the finite chain, the spectrum Eq.(2.20) is symmetric about $\delta = 0$ because $H_{\text{BdG}}(-\delta) = \mathcal{S} H_{\text{BdG}}(\delta) \mathcal{S}^\dagger$ with a unitary operator $\mathcal{S} = \mathbf{1}_N \otimes \sigma_z$. When the coupling between the first and the last sites is continuously reduced to zero, i.e. boundary conditions are changed from periodic to open. In the zero chemical potential limit, Majorana zero-modes (fermionic excitations) appear localized on the edges of the chain. These edge

modes are robust when gain-loss potentials are introduced on random sites [50] or on parity symmetric sites with disorder [51].

2.4 \mathcal{PT} -symmetric Kitaev chain

Recently there has been a number of studies in the setting of topological superconductors with non-Hermitian \mathcal{PT} -symmetric potentials [50]–[58]. These studies explore the effects of non-Hermiticity on these edge states which are characterized by zero energy. The Kitaev chain with a pair of \mathcal{PT} -symmetric potentials at the edges have been studied in [50], [51], [55], [56]. The result is the emergence of an additional pair of edge state with a non-zero energy eigenvalue [51]. In another study it was reported that the zero energy of these (Majorana) edge states remain unperturbed unless the \mathcal{PT} potentials are imposed on the unpaired Majorana sites on the edges of an open Kitaev chain [50]. Jin and Song show that for a finite size Kitaev chain, the non-Hermitian coupling potentials on the edges generate a pair of coalescing \mathcal{PT} -symmetry breaking modes with zero energy beyond the topological phase transition point, suggesting a non-Hermitian extension to the topological properties of the Kitaev chain. The energy eigenvalues of these states are real in the topological trivial phase (TTP) and become imaginary-energy modes in the topological non-trivial phase (TNP) [56].

In contrast to these studies on the Majorana edge modes, we focused on the variation of the \mathcal{PT} -breaking threshold $\gamma_{\text{th}}(m_0, N)$ with the location m_0 of the gain potential in a Kitaev chain of size N . These results are a part of our published paper [59].

Recall the Hermitian Kitaev Hamiltonian from Eq. 2.17. To this toy model with open boundary conditions (OBC), we add a pair of balanced gain/loss potentials $\pm i\gamma$ at mirror symmetric sites m_0 and \bar{m}_0 ,

$$i\Gamma = \frac{i\gamma}{2} (|m_0\rangle\langle m_0| - |\bar{m}_0\rangle\langle \bar{m}_0|) \otimes \sigma_z, \quad (2.21)$$

and thereby get a non-Hermitian, \mathcal{PT} -symmetric Kitaev chain Hamiltonian

$$H_{\text{K}}(\gamma, \delta, \mu) = H_{\text{BdG}} + i\Gamma. \quad (2.22)$$

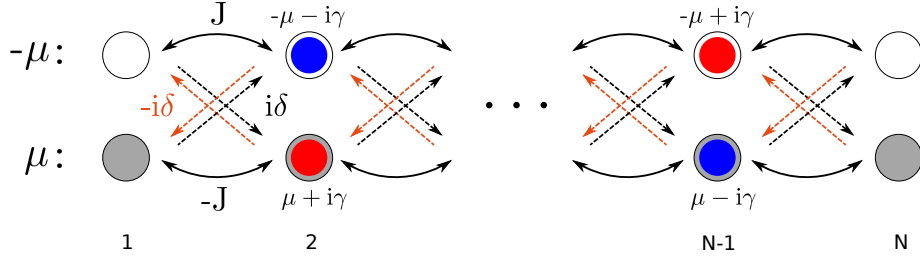


Figure 2.7. Schematic representation of a Kitaev model with one pair of gain and loss potentials, Eq.(2.22). Two chains (gray and white) with detuned potentials $\pm\mu$ have nearest neighbor Hermitian tunneling amplitudes $\pm J$, and next-nearest-neighbor Hermitian amplitudes $\pm i\delta$. Due to the presence of two degree of freedom on each site [60], the potential $i\gamma$ on site m_0 acts as gain (red) for one and loss (blue) for the other. This schematic can be realized with coupled resonator rings where one can engineer complex, Hermitian tunneling amplitudes.

Fig. 2.7 shows a schematic representation of a lattice model described by Eq.(2.22). Although the original model refers to a many-body fermionic system with two bands, in its “single-particle” form, Eq.(2.22), it can be interpreted as two detuned coupled chains with Hermitian nearest-neighbor couplings $\pm J$ and Hermitian, purely imaginary, next-nearest-neighbor couplings $\pm i\delta$ [60]. The gain potential on site m_0 , given by $(i\gamma/2)|m_0\rangle\langle m_0| \otimes \sigma_z$, then stands for gain in one chain and loss in the second chain. This representation of the \mathcal{PT} -symmetric Kitaev model can be experimentally implemented in resonator arrays where real and purely imaginary tunneling amplitudes can be easily engineered. In the next section we explore the global phase diagram for the \mathcal{PT} -symmetry breaking threshold $\gamma_{\text{th}}(m_0, \delta, \mu)$.

2.4.1 \mathcal{PT} -threshold Results

The results presented in this section are obtained by diagonalizing H_K or H_{BdG} for Kitaev chains of size $N = 20$ (Fig. 2.8) and $N = 21$ (Fig. 2.9). They remain qualitatively same for larger chain sizes, and the differences between even and odd parity chains persist in the large N limit, as they do for a simple tight-binding model. All energy scales are measured in units of the tight-binding coupling $J = 1$. Figures 2.8(a)-(d) show the the energy eigenvalues E_n for a Hermitian Kitaev chain as a function of the superconducting order parameter δ/J . In the trivial case, when $\delta = 0 = \mu$, we get the cosine-band of a tight-binding model. As the

detuning δ is increased from (a) to (d), the two bands become well-separated. On the other hand, at a fixed detuning, when δ is increased, the bands develop fan-like linear dispersion, leading to massively degenerate flat bands at $\delta/J = 1$ at zero detuning. As the detuning is increased from $\mu = 0$, the system develops two crossing points (shown by blue circles in (b)). We also note that zero-energy states are present when $\mu < 2J$. At $\mu/J = 2$, the superconducting gap closes marking a phase transition to the topologically trivial phase. Here the mid-gap states become a part of the bulk. When μ is increased further, Fig. 2.8(d), the system is in the trivial superconducting phase and energy spectrum is gapped. The topological, edge-localized zero energy states only occur when $\mu \leq 2J$. At $\mu = 0$, these zero-energy states are fully localized on the end sites. When μ is increased, these states extend into the bulk of the chain, with an exponentially decaying probability density [57], [58]. The Hermitian, (near or exact) degeneracies of the Hamiltonian H_{BdG} play an important role in determining the threshold gain-loss strength γ_{th} when a pair of gain-loss potentials is introduced at mirror symmetric sites.

Figures 2.8(e)-(h) show the numerically determined \mathcal{PT} -symmetry breaking threshold γ_{th} for the $N = 20$ chain as a function of m_0 and superconducting order parameter δ . When $\mu/J = 0$ (panel e), we see that $\gamma_{\text{th}}(m_0, \delta)$ has the characteristic U-shaped behavior [47], [48] when $\delta = 0$ and becomes mostly zero for intermediate locations $m_0 \sim N/4$. When $m_0 = 1$, i.e. when the gain-loss locations are farthest apart, the \mathcal{PT} threshold is maximized to $\gamma_{\text{th}} = J$, and reflects the non-local robustness that is ubiquitous for systems with open boundary conditions [21], [48]. In this case, the states that participate in the \mathcal{PT} -breaking process are the mid-band states. As m_0 is increased, the threshold decreases and it rises back to $\gamma_{\text{th}} = J$ when the gain and loss locations are nearest neighbors, i.e $m_0 = N/2$. In this situation, all eigenvalues simultaneously and pairwise become complex, giving rise to maximal \mathcal{PT} -symmetry breaking [46].

In contrast to the variation with m_0 , we find that when the superconducting order parameter δ is varied, for most locations m_0 , the \mathcal{PT} -threshold is uniformly suppressed from its $\delta = 0$ value. The exception is the region $m_0 \sim 1$, where, as δ is increased, we see that the \mathcal{PT} threshold at $\delta = J$ is double its $\delta = 0$ value [51], where the flat bands occur; see Fig. 2.8(a). As δ is increased further, the threshold dips to zero and then increases reaching a steady,

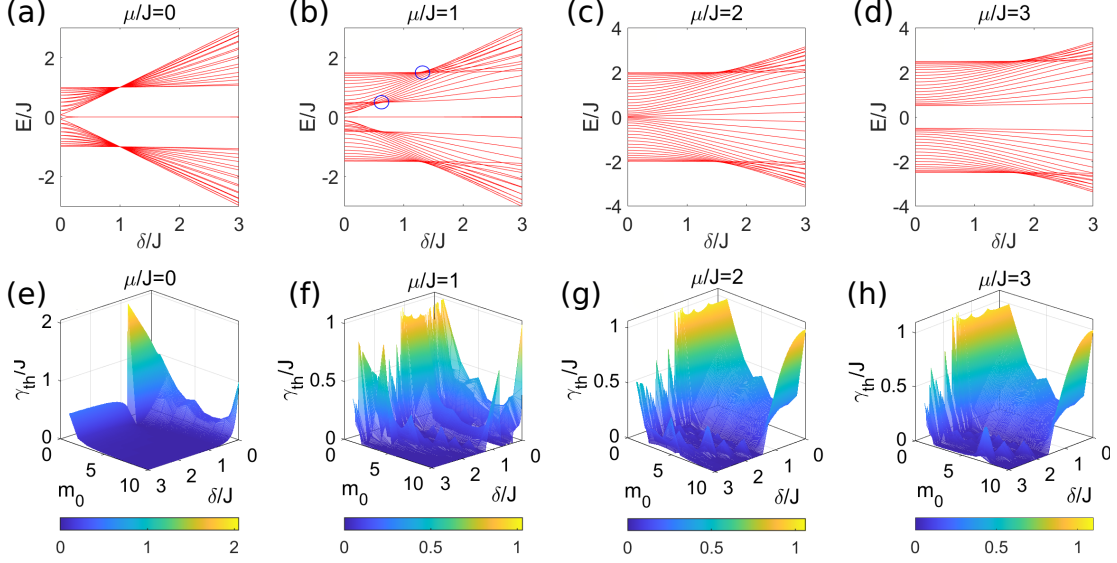


Figure 2.8. Energy eigenvalues (in units of J) of an $N = 20$ site Hamiltonian $H_{\text{BdG}}(\delta)$, Eq.(2.17) as a function of detuning. (a) $\mu/J = 0$, (b) $\mu/J = 1$ have topological edge modes, while the system is in the topologically trivial phase at (c) $\mu/J = 2$ and (d) $\mu/J = 3$. Corresponding \mathcal{PT} threshold values γ_{th}/J obtained from the Hamiltonian H_{K} , Eq.(2.22) are plotted as a function of the gain location $m_0 \in [1, N/2]$ and the superconducting order parameter δ/J : (e) $\mu/J = 0$, (f) $\mu/J = 1$, (g) $\mu/J = 2$ (h) $\mu/J = 3$. Most of these features can be understood in terms of Hermitian band structure, panels a-d.

δ -independent value of $\gamma_{\text{th}} = J/2$. As the detuning μ is increased from zero, Fig. 2.8(f), there is an overall suppression of the \mathcal{PT} -breaking threshold γ_{th} although the characteristic U-shape behavior as a function of m_0 and the non-monotonic behavior as a function of δ for farthest gain-loss potentials are both retained. These qualitative trends continue for $\mu \leq 2J$, i.e. when the system is in the topological phase.

When the detuning is large, $\mu > 2J$, the system enters into a trivial superconducting phase with no edge localized states, (g) and (h). In this regime, the system consists of two separated bands, and therefore the \mathcal{PT} -threshold does not sensitively depend on the detuning. On the other hand, when gain and loss are on nearest neighbor sites, $m_0 = N/2$, the threshold is suppressed to zero for $\delta \sim 2J$. This is explained by the level crossings that occur near band edges; see Figs. 2.8(c) and (d).

Figure 2.9 shows corresponding, representative results for a chain with $N = 21$ sites. Panels (a)-(d) shows the dispersion of the Hermitian Kitaev chain as a function of δ/J for

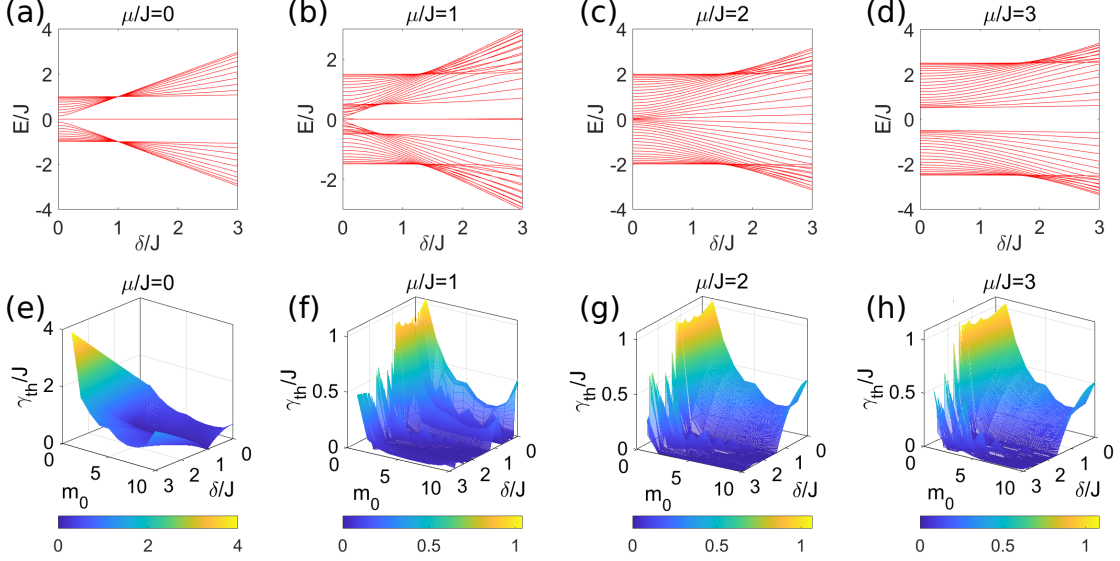


Figure 2.9. Energy eigenvalues (in units of J) of an $N = 21$ site Hamiltonian $H_{\text{BdG}}(\delta)$, Eq.(2.17) as a function of detuning. (a) $\mu/J = 0$, (b) $\mu/J = 1$ have mid-gap states with zero energy, but these are not topological. (c) $\mu/J = 2$ and (d) $\mu/J = 3$ show emergence of a gapped spectrum. Corresponding \mathcal{PT} threshold values γ_{th}/J obtained from the Hamiltonian H_{K} , Eq.(2.22) are plotted as a function of the gain location $m_0 \in [1, (N - 1)/2]$ and the superconducting order parameter δ/J : (e) $\mu/J = 0$, (f) $\mu/J = 1$, (g) $\mu/J = 2$ (h) $\mu/J = 3$. Due to the absence of topological edge modes, the \mathcal{PT} threshold behavior at $\mu = 0$ is markedly different from that of an even chain, Fig. 2.8(e). At nonzero detuning, the threshold is non-monotonically suppressed with increasing δ .

increasing detuning values. At zero detuning, panel (a), the band structure looks similar to that in Fig. 2.8(a), but with a key difference: there is no degenerate pair of topological zero energy states. As μ is increased, the qualitative evolution of the band structure is similar to that of an even Kitaev chain, with the band gap closing at $\mu = 2J$ and well-separated two-band structure at higher detuning values. Panel (e) shows the \mathcal{PT} threshold γ_{th}/J as a function of the gain location m_0 and the superconducting order parameter δ/J . Near $\delta = 0$, we recover the characteristic U-shaped behavior with a robust threshold $\gamma_{\text{th}} \sim J$ when $m_0 = 1$, i.e. the farthest gain and loss pairs. In contrast, for closest gain-loss locations, i.e. $m_0 = (N - 1)/2$, the threshold reaches $\gamma_{\text{th}} \sim J/2$ [46], [48]. This behavior is seen across the entire range of μ/J ; panels (f)-(h).

In a sharp contrast, the behavior of the threshold γ_{th}/J as a function of the superconducting order parameter δ/J is markedly different for the zero detuning case, panel (e), vs. the nonzero detuning case, panels (f)-(h). For the latter, the threshold shows a non-monotonic suppression of γ_{th} with increasing δ/J . When $\mu = 0$, on the other hand, we see that the γ_{th} increases with δ/J , thereby strengthening the \mathcal{PT} -symmetric phase. We emphasize that when $m_0 = 1$ —gain and loss localized on the end sites—this enhancement occurs even at $\delta/J = 1$. Recall that at $\delta/J = 1$, the Hermitian band structure forms flat bands (Figs. 2.8a, 2.9a), leading to a zero threshold irrespective of m_0 in the even chain, Fig. 2.8e.

To get better insights into the rich structure of the \mathcal{PT} threshold, we consider the behavior of γ_{th}/J for nearest-neighbor gain-loss potentials, $m_0 = N/2$, as a function of μ/J and δ/J for an $N = 20$ site chain (Fig. 2.10(a)). Apart from the nonzero threshold that occurs in the limit of a non-superconducting, tight-binding chain ($\delta = 0$) for any detuning, we see that $\gamma_{\text{th}} = 0$ for large δ for any μ , and there is beak-shaped region in the $\mu - \delta$ plane with a positive \mathcal{PT} threshold. In the magnified view of the region at small $\delta/J < 1$ (Fig. 2.10(b)), we see significant variations in the \mathcal{PT} threshold as we sweep across μ/J . These threshold “dips” occur at values of μ/J where the lowest energy levels in the bulk become degenerate. The white dashed line in Fig. 2.10(a), separating the zero-threshold region from the positive-threshold regions, is described by equation $\alpha\mu J + |J^2 - \delta^2|$ where $\alpha \sim 0.5$ is an N -dependent constant. The region $0 < \mu/J < 2$, $\delta/J < 1$ enveloped in the \mathcal{PT} phase boundary shows many ripples with $\gamma_{\text{th}} > 0$ but it decays to zero in the thermodynamic limit.

We remind the reader that in the $\delta = 0$ tight-binding case with nearest-neighbor gain-loss potentials, all states contribute pairwise to the \mathcal{PT} -symmetry breaking [46]. In contrast, in the current set up, only the states near the band edges become degenerate and then complex conjugate. In order to find the asymptotic behavior of the zero-threshold line, we turn to the Hermitian band structure, Eq. 2.20. A zero threshold is a result of degeneracy in the

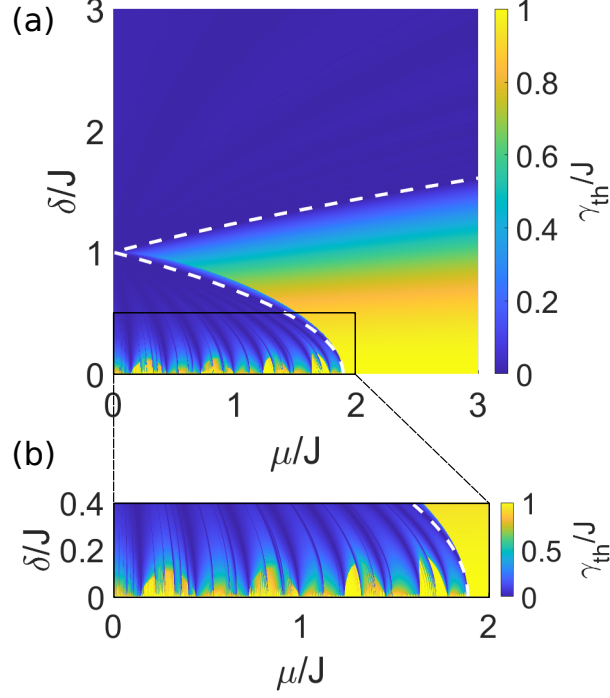


Figure 2.10. (a) \mathcal{PT} -symmetry threshold for a chain with $N = 20$ and $m_0 = N/2$. The white dashed line, separating the zero-threshold region from the nonzero-threshold region, is empirically fit by equation $\alpha\mu J + |J^2 - \delta^2| = 0$ where $\alpha \rightarrow 0.5$ as $N \rightarrow \infty$; at $N = 20$, we find that $\alpha = 0.53$. This functional dependence can be obtained by requiring that two adjacent levels in the Hermitian band-structure become degenerate to get $\gamma_{\text{th}} = 0$. (b) closeup of the boxed region near the origin shows multiple ripples in γ_{th} .

consecutive levels, i.e. $E(q_k) = E(q_{k-1})$ where $q_k = \pi k/(N+1)$ are the lattice quasimomenta consistent with open boundary conditions. Simplifying the degeneracy criterion gives

$$a_1\mu J + a_2(J^2 - \delta^2) = 0, \quad (2.23)$$

$$a_1 = \cos(q_k) - \cos(q_{k-1}), \quad (2.24)$$

$$a_2 = a_1 [\cos(q_k) + \cos(q_{k-1})]. \quad (2.25)$$

Defining $\alpha = a_1/|a_2|$, we obtain an analytical expression for asymptotic value of α . From the energy spectra in Figs. 2.8 (a)-(d) and numerical analysis, it follows that regions near $q \sim 0, \pi$ contribute giving $\alpha \rightarrow 0.5$ in the limit $N \rightarrow \infty$.

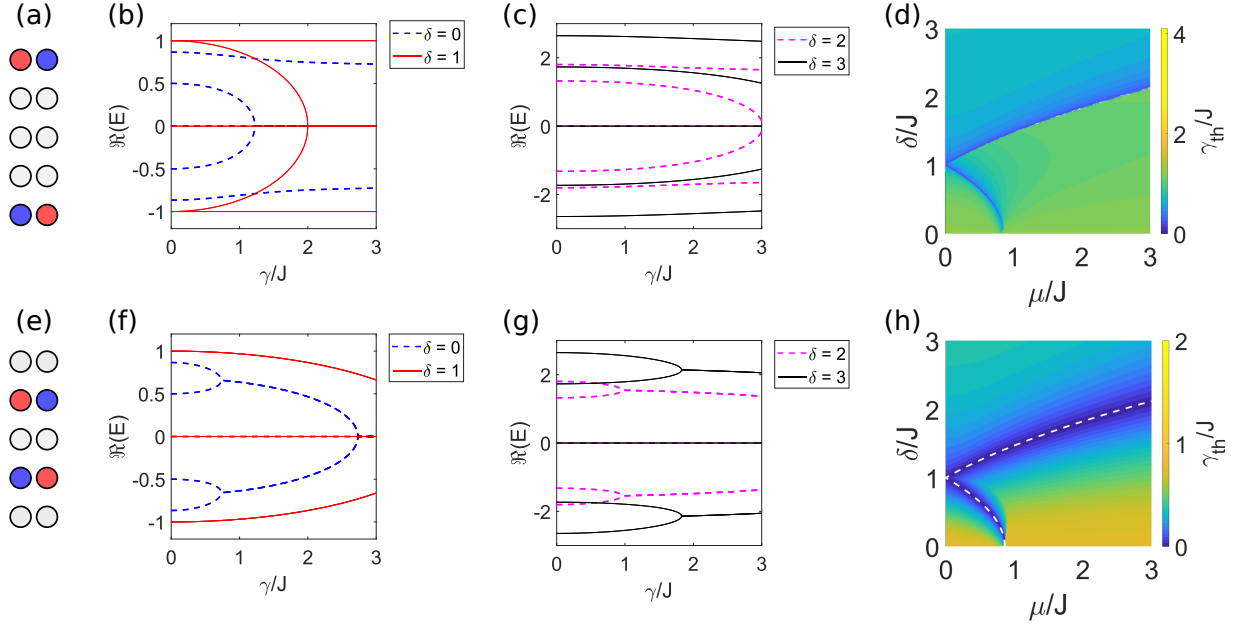


Figure 2.11. \mathcal{PT} threshold for an $N = 5$ chain. (a) Schematic of $N = 5$ chain with $m_0 = 1$. (b)-(c) Flow of real part of eigenvalues of the $N = 5$ chain as a function of γ for farthest gain-loss locations (far left) shows that \mathcal{PT} breaking occurs at an EP3 and the threshold increases monotonically with the superconducting order parameter δ . (d) $\gamma_{\text{th}}(\mu, \delta)$ shows behavior consistent with Fig. 2.10 including a contour of zero threshold given by $\alpha\mu J + |J^2 - \delta^2| = 0$. (e) Schematic of $N = 5$ chain with $m_0 = 2$. (f)-(g) Corresponding results for closest gain-loss locations, $m_0 = 2$, show that \mathcal{PT} -breaking occurs at an EP2, and the threshold varies non-monotonically with δ . (h) $\gamma_{\text{th}}(\mu, \delta)$ map shows features similar to those in panel (d). The white-dashed line is zero-threshold contour given by $\alpha\mu J + |J^2 - \delta^2| = 0$ with $\alpha = 1.6$.

Next, to understand the global behavior of the \mathcal{PT} threshold $\gamma_{\text{th}}(m_0, \mu, \delta)$ in an odd chain, we look towards the smallest nontrivial case with zero detuning, i.e. $N = 5$ and $\mu = 0$. When $m_0 = 1$, the doubly-degenerate energy spectrum is analytically tractable and is given by

$$E_n = \frac{\mp 1}{2\sqrt{2}} \left[4(J^2 + \delta^2) - \gamma^2 \pm \sqrt{4(J^2 - \delta^2)^2 + \gamma^4} \right]^{1/2}, \quad (2.26)$$

along with two (degenerate) zero eigenvalues, $E_{5,6} = 0$. As γ is increased, the energy levels $E_{3,4} = -E_{7,8}$ first approach each other, merge with the zero-levels, and then become

complex conjugate, thereby giving rise to an exceptional point of order three (EP3). The \mathcal{PT} -threshold in this case is given by

$$\gamma_{\text{th}}(1) = J \left[\frac{3(\delta^2 + J^2)^2 + 4\delta^2 J^2}{2J^2(\delta^2 + J^2)} \right]. \quad (2.27)$$

A similar analysis for the case with next-nearest-neighbor gain-loss potentials gives particle-hole symmetric, doubly degenerate spectra

$$E_n = \frac{\mp 1}{2\sqrt{2}} \left[4(J^2 + \delta^2) - \gamma^2 \pm \sqrt{A} \right]^{1/2}, \quad (2.28)$$

$$A = 4(J^2 - \delta^2)^2 + \gamma^4 - 8\gamma^2(J^2 + \gamma^2), \quad (2.29)$$

along with two (degenerate) zero eigenvalues, $E_{5,6} = 0$. As γ is increased, we now find that the levels near the band-edge approach each other and become degenerate, giving rise to an EP2. The \mathcal{PT} threshold, obtained by requiring $E_{1,2}(\gamma_{\text{th}}) = E_{3,4}(\gamma_{\text{th}})$, is given by

$$\gamma_{\text{th}}(2) = \left[4(J^2 + \delta^2) - 2\sqrt{3\delta^4 + 10\delta^2 J^2 + 3J^4} \right]^{1/2}. \quad (2.30)$$

We note that these analytical results are only valid for zero detuning, and for finite detuning $\mu > 0$, we have to resort to numerical calculations.

Figure 2.11(a) shows the schematic of an $N = 5$ site chain with gain-loss potentials at its ends, i.e. $m_0 = 1$. Panels (b)-(c) show the flow of the real parts of energy eigenvalues for the model as a function of γ/J for different values of δ . We see that increasing γ leads to \mathcal{PT} -breaking that occurs at the center of the band, giving rise to an EP3. They also show that the threshold increases monotonically with δ , consistent with what is seen in Fig. 2.9e. Panel (d) shows numerically obtained threshold diagram in the $\mu - \delta$ plane.

Figure 2.11(e) shows the configuration with nearest-possible gain-loss potentials, i.e. $m_0 = 2$. Panels (f)-(g) show the flow of real part of eigenvalues for the model. Increasing γ in this case leads to \mathcal{PT} -breaking at the band edges, and it has a non-monotonic dependence on the superconducting order parameter δ , also seen in Fig. 2.9e. Panel (h) shows numerically obtained threshold $\gamma_{\text{th}}(\mu, \delta)$. The similarity of these threshold maps with

Fig. 2.10 is striking. By fitting the zero threshold contour to the form $\alpha\mu J + |J^2 - \delta^2| = 0$ (dashed white line in panel (h)), we obtain $\alpha = 1.6$.

2.4.2 Exceptional Lines and reentrant \mathcal{PT} phase

In one-dimensional lattice models with a single pair of gain and loss potentials, typically, the \mathcal{PT} -symmetry breaking occurs monotonically with increasing gain-loss strength γ . This is true for uniform chains with open [48] or periodic boundary conditions [61]; the Su-Schrieffer-Heeger, the Aubrey-Andre-Harper or quasi-periodic models [62], [63]; and models with non-uniform, parity-time symmetric tunneling profiles [64], including the perfect-state transfer models. On the other hand, the presence of two or more gain-loss potentials can lead to re-entrant \mathcal{PT} -symmetric phase [65], [66] where increasing gain-loss strength leads to repeated \mathcal{PT} -symmetry breaking and \mathcal{PT} -symmetry restoration transitions.

In contrast to these models with multiple non-Hermitian terms [65], [66], the Kitaev chain we have considered shows a re-entrant \mathcal{PT} -symmetric phase and its subsequent breaking when the gain-loss strength γ is increased. This phenomenon occurs for an even chain with $\mu = 0$ and $m_0 = 1$, at moderate superconducting order parameter $1 \leq \delta/J \leq \sqrt{2}$, independent of the chain size. In Fig. 2.12(a), we plot $\Lambda(\gamma, \delta) = \log_{10} \max_k \Im(E_k)$ where E_k are (purely real or complex-conjugate) eigenvalues of the Hamiltonian H_K for an $N = 8$ chain. The \mathcal{PT} -symmetric region is marked by black, and the rest is \mathcal{PT} -symmetry broken region. With $\delta/J \sim 1$, as γ is increased, the first \mathcal{PT} symmetry breaking near $\gamma/J \sim 0.5$ occurs due to the level-attraction between and coalescence of two highest energy states in the upper band; recall that due to the particle-hole symmetric nature of the spectrum, two lowest energy levels in the lower band concurrently become degenerate. With increasing γ , subsequent lower energy levels, except the lowest state in the upper band, coalesce in pairs. This sequence of transitions leads to a large number of exceptional points in the \mathcal{PT} -symmetry broken region. Further increasing γ leads to a reverse process where levels with complex-conjugate energies undergo level-attraction and \mathcal{PT} -symmetry is restored. For the lowest-energy states in the upper band (and their chiral counterparts), the re-entrant \mathcal{PT} -symmetric phase is accompanied by a qualitative change where the wave-function weight

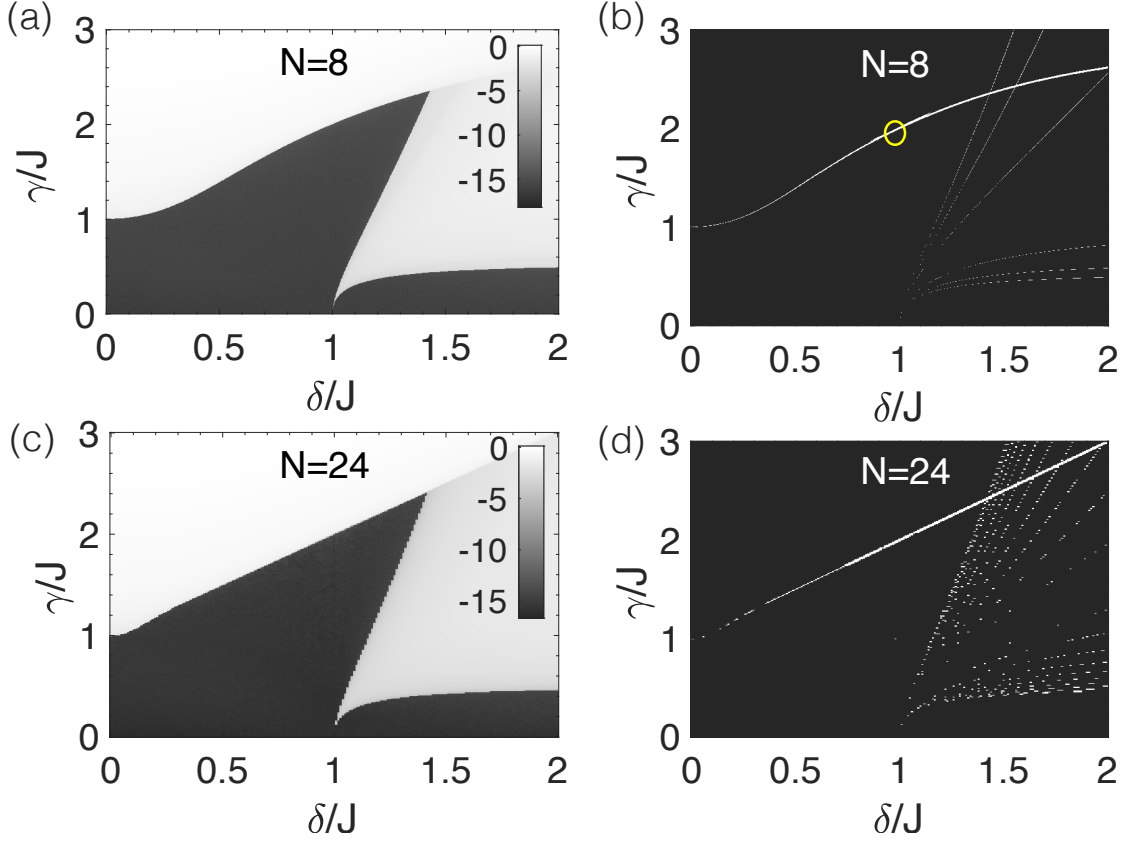


Figure 2.12. (a) \mathcal{PT} phase diagram in the $\gamma - \delta$ plane for an $N = 8$ lattice with $\mu = 0$ and $m_0 = 1$ shows the heat map of $\Lambda \equiv \log_{10} \max_k \Im(E_k)$ where E_k are the $2N$ are the eigenvalues of H_K , Eq.(2.22). A re-entrant \mathcal{PT} -symmetric phase (black) emerges in the range $1 \leq \delta/J \leq \sqrt{2}$ as the gain-loss strength γ/J is increased. (b) EP2 contours at the \mathcal{PT} boundary and in the \mathcal{PT} -broken region show sequential coalescence of eigenvalues. At $\delta/J = 1$, due to the presence of robust Majorana modes, a third-order EP emerges at $\gamma/J = 2$ (yellow circle). (c)-(d) corresponding results for an $N = 24$ lattice shows same qualitative features.

shifts from the bulk to the edges. As γ is increased further, the system enters the \mathcal{PT} -broken region again. This second \mathcal{PT} transition across an EP is driven by coalescence of the near-zero-energy state with state at the bottom of the top band.

To map out the exceptional point contours in the $\delta - \gamma$ plane, we use the (Dirac) inner-product matrix $M_{pq} = |\langle \psi_p | \psi_q \rangle|$ where $|\psi_k\rangle$ is the (Dirac)-normalized right eigenvector of H_K with eigenvalue λ_k . The order of the EP is then given by $\max_p \sum_{q \neq p} M_{pq}$. Figure 2.12(b) shows the contours of exceptional points in the parameter space. In addition to the bound-

aries of \mathcal{PT} -symmetric and \mathcal{PT} -broken regions, seen in Fig. 2.12(a), we see EP contours that denote the cascades of eigenvalue coalescence that occur in the \mathcal{PT} -broken region as γ is increased. Of particular interest is the contour that starts at $\delta = 0$ and $\gamma/J = 1$. At point $\delta/J = 1$, the system has fully degenerate bands with robust, mid-gap edge states. Therefore, introduction of the gain-loss potentials leads to a third-order EP at $\gamma/J = 2$ (shown by a yellow circle) in the otherwise second-order EP contour. We note that the prominent re-entrant \mathcal{PT} phases only occur when the gain-loss potentials are farthest apart, i.e. $m_0 = 1$ and remain robust only at $\mu = 0$ for any even N ; Figs. 2.12(c)-(d) show the phase diagram and EP contours for an $N = 20$ Kitaev chain.

In summary we have shown that the threshold profile is rich, with persistent differences between even and odd parity lattices. In particular, we have found that for a zero-detuning chain with odd number of sites, the threshold is enhanced with increasing superconducting order parameter. For an even chain with edge gain-loss potentials and superconducting coupling $\delta \gtrsim 1$, we discover re-entrant \mathcal{PT} -symmetric phase, and \mathcal{PT} -phase boundaries that contain both second and third order EPs. We have also discussed, briefly, a potential realization of our lattice model with coupled optical resonators. Our results further the understanding of non-Hermitian condensed matter models in the presence of realistically achievable gain and loss.

3. \mathcal{PT} -SYMMETRIC ELECTRICAL CIRCUITS

The content of this chapter is a part of our paper which have been slightly modified. The preprint is available on arxiv.org and in the process of submission to a journal.

The field of \mathcal{PT} -symmetry has grown and diversified due to its easily accessible experimental platforms like photonics, ultra cold atoms and electrical circuits. The realization that a \mathcal{PT} -symmetric Hamiltonian represent systems with spatially separated balanced gain and loss elements, has been the key motivator. Some of these experimental platforms include two waveguides [8], [67], two mechanical oscillators [14], two coupled electrical oscillators [12], [68], two fiber loops [9], two or more coupled micro-resonators [69]–[71], acoustics [72], diffusive systems [17], damped and driven shallow fluids [73], and two coupled, time-delayed semiconductor lasers [74]. As you might have realised, that there are always *two* elements. In this chapter we will take a look a novel protocol we designed, for \mathcal{PT} symmetry based on a time-dependent similarity transformation using electrical circuits as a platform. The manifestation of a complex gauge potential, from the non-unitary change of basis, generates a representation of separated, balanced gain and loss potentials. An added benefit of this approach is that we can implement \mathcal{PT} symmetry in a minimal system setting with only one variable element which in our case is a single LC oscillator.

3.1 \mathcal{PT} -symmetry in a single oscillator

Let us consider a LC oscillator circuit as shown in Figure 3.1a in which the voltage $V(t)$ across the capacitor and the current $I(t)$ in the inductor satisfy following Kirchhoff rules,

$$I(t) + C(t) \frac{dV(t)}{dt} = 0, \tag{3.1}$$

$$V(t) - L(t) \frac{dI(t)}{dt} = 0. \tag{3.2}$$

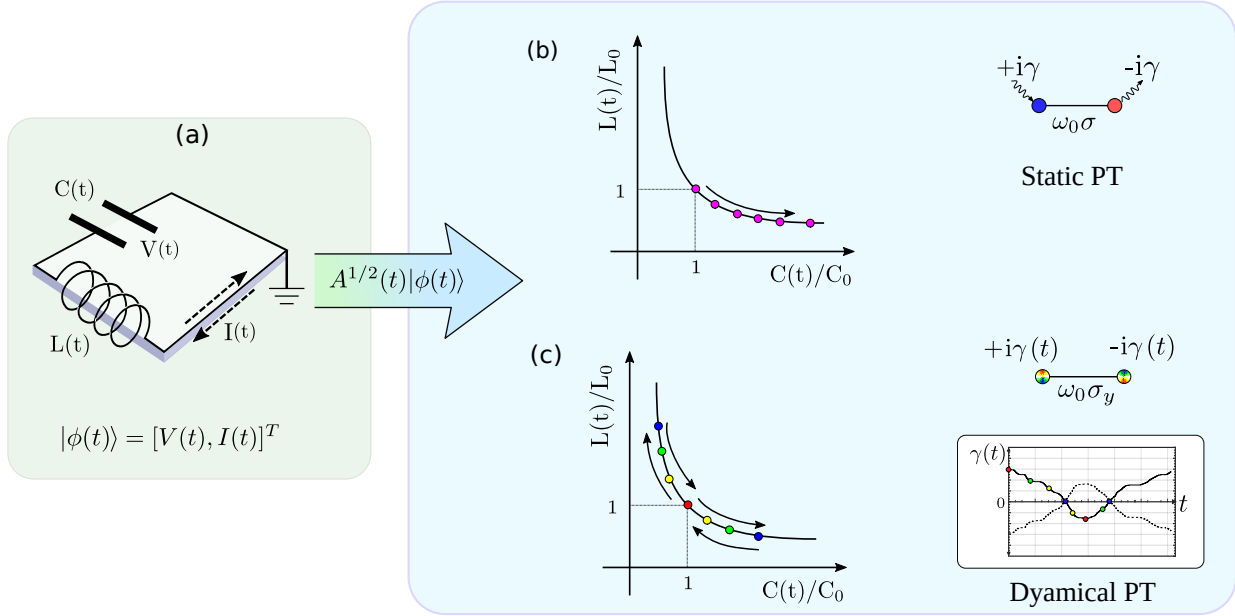


Figure 3.1. \mathcal{PT} -symmetry in a single LC circuit. (a) The state $|\phi(t)\rangle$ of the circuit encodes the voltage $V(t)$ across the capacitor and current $I(t)$ in the inductor, and satisfies a linear, first-order equation given by Kirchoff laws. A static change-of-basis to $|\psi(t)\rangle = A^{1/2}|\phi(t)\rangle$ leads to a Hermitian Hamiltonian $H_0 = \omega_0\sigma_y$ for the new state $|\psi(t)\rangle$. Thus, an LC circuit is mapped into a two-site model. (b) When $C(t), L(t)$ are exponentially varied subject to the constraint $L(t)C(t) = L_0C_0$ (hyperbola), the time-dependent change of basis generates balanced, constant gain and loss $\pm i\gamma$. This leads to a purely imaginary, \mathcal{PT} -symmetric Hamiltonian $H_{\mathcal{PT}} = \omega_0\sigma_y + i\gamma\sigma_z$. (c) When the constrained variation is not exponential, arbitrary, but balanced gain and loss potentials $\pm i\gamma(t)$ can be generated. Here, we focus on the special case when $\gamma(t)$ is periodic.

With some arrangement, these equations in a matrix representation look like,

$$i \frac{d}{dt} \begin{bmatrix} V(t) \\ I(t) \end{bmatrix} = \begin{bmatrix} 0 & -i/C(t) \\ i/L(t) & 0 \end{bmatrix} \begin{bmatrix} V(t) \\ I(t) \end{bmatrix} \quad (3.3)$$

$$i\partial_t|\phi(t)\rangle = M|\phi(t)\rangle \quad (3.4)$$

Multiplying ‘ i ’ on both side is a cheap trick to make it look like the Schrödinger equation with a “state vector” defined as $|\phi(t)\rangle \equiv [V(t), I(t)]^T$. The imaginary, non-symmetric matrix M has eigenvalues $\epsilon_{\pm} = \pm\omega_0 = \pm 1/\sqrt{LC}$.

Under a static, non-unitary change of basis to $|\psi(t)\rangle = A^{1/2}|\phi(t)\rangle$, the equation of motion becomes $i\partial_t|\psi(t)\rangle = H_0|\psi(t)\rangle$ with a Hermitian Hamiltonian

$$H_0 = A^{1/2}MA^{-1/2} = \omega_0\sigma_y. \quad (3.5)$$

Here

$$A = \begin{bmatrix} C/2 & 0 \\ 0 & L/2 \end{bmatrix} \quad (3.6)$$

and σ_y is the Pauli y-matrix. The energy of the circuit by can be calculated by take the expectation value

$$\langle\phi(t)|A|\phi(t)\rangle = \frac{1}{2}CV(t)^2 + \frac{1}{2}LI(t)^2 = \mathcal{E}(t). \quad (3.7)$$

Here things get interesting when the basis transformation is time dependent, and so the new state vector satisfies $i\partial_t|\psi(t)\rangle = H_{\text{eff}}(t)|\psi(t)\rangle$. The effective Hamiltonian H_{eff} is the sum of (possibly time-dependent) Hamiltonian $H_0(t)$ and a gauge potential $i\Gamma(t)$ that arises from the non-constant nature of the change of basis matrix [75],

$$H_{\text{eff}} = A(t)^{1/2}MA(t)^{-1/2} + i\left(\frac{\partial}{\partial t}A(t)^{1/2}\right)A(t)^{-1/2} \quad (3.8)$$

$$= H_0(t) + i\frac{\partial}{\partial t} \ln A^{1/2}(t) \quad (3.9)$$

We label our newly manifested gauge term as,

$$\Gamma(t) = \partial_t \ln A^{1/2}(t). \quad (3.10)$$

In fundamentally quantum systems, the matrix $A^{1/2}$ is unitary and gives rise to a Hermitian gauge term $i\Gamma = (i\Gamma)^\dagger$. In contrast, for effective models like ours, a non-unitary $A^{1/2}(t)$ can be tailored to create non-Hermitian, gain and loss potentials.

Generating a \mathcal{PT} Hamiltonian

Now, let us consider constrained variations of the form $C(t) = C_0 \exp[+2f(t)]$ and $L(t) = L_0 \exp[-2f(t)]$ to ensure that the frequency of the oscillator remains unchanged. Such variations give rise to a traceless, anti-Hermitian gauge potential $i\Gamma = i\gamma(t)\sigma_z = i(df/dt)\sigma_z$ that represents balanced gain and loss in a solitary oscillator. The effective Hamiltonian then becomes

$$H_{\text{PT}}(t) = \omega_0\sigma_y + i\gamma(t)\sigma_z. \quad (3.11)$$

$H_{\text{PT}}(t)$ is invariant under combined operations of parity $\mathcal{P} = \sigma_x$ and time reversal $\mathcal{T} = *$ (complex conjugation). In contrast to quantum systems with a complex state vector, the realness of the elements of $|\psi(t)\rangle = [\sqrt{C(t)/2V(t)}, \sqrt{L(t)/2I(t)}]^T$ is guaranteed by an H_{PT} with purely imaginary entries. This requirement also constrains the most general form of the non-Hermitian Hamiltonian for this system to $H_{\text{PT}} = h_y\sigma_y + ih_z\sigma_z + ih_x\sigma_x$ with $h_k \in \mathbb{R}$.

With a suitable choice of the dimensionless function $f(t)$, Eq.(3.11) provides the protocol for arbitrary, balanced gain and loss for the energy dynamics. When $f(t) = \gamma t$ is linear in time, Eq.(3.11) gives the static \mathcal{PT} -symmetric Hamiltonian $H_{\text{PT}}(\gamma) = \omega_0\sigma_y + i\gamma\sigma_z$. As shown in Fig. 3.1b, when $\gamma > 0$, the capacitor acts as the “gain site” and the inductor acts as the “loss site” for the circuit energy. On the other hand, surfing the hyperbola $L(t)C(t) = L_0C_0$ back and forth leads to a time-periodic $\gamma(t)$ where each “site” acts as a gain for fraction of the period and a loss for rest of the time (Fig. 3.1c).

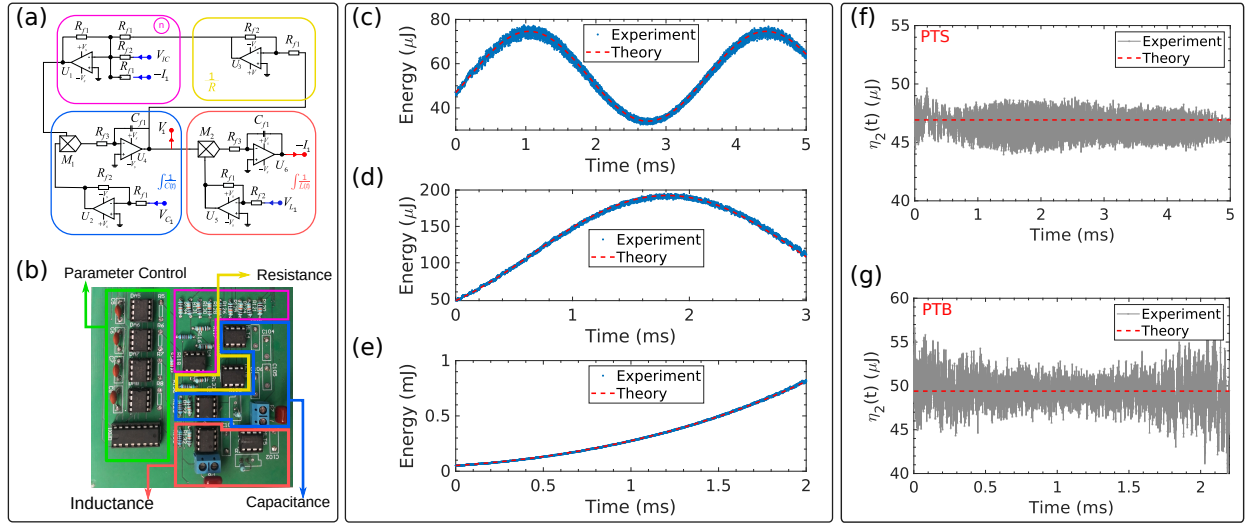


Figure 3.2. Dynamics of a \mathcal{PT} -dimer with static gain and loss. (a) Schematics of synthetic LC circuit comprising capacitor (red), inductor (blue), resistor (yellow), and signal adder (pink) boxes. (b) Actual circuit board with corresponding color-coded components marked. The circuit has $C = 100 \mu\text{F}$, $L = 0.01 \text{ H}$, $\omega_0 = (2\pi) \times 159.15 \text{ Hz}$, and a parasitic resistance $R = 10^3 \Omega$. (c)-(d) Circuit energy $\mathcal{E}(t)$ oscillates in the \mathcal{PT} -symmetric phase. The gain-loss strength is (c) $\gamma = 0.375\omega_0$ and (d) $\gamma = 0.75\omega_0$. (e) $\mathcal{E}(t)$ grows exponentially in the \mathcal{PT} -broken phase, $\gamma = 1.05\omega_0$ (experimental data: blue dots, theory: red dashed line). (f) At $\gamma = 0.375\omega_0$ (\mathcal{PT} -symmetric region, PTS) although the circuit energy $\mathcal{E}(t)$ oscillates, $\eta_2(t) = \mathcal{E}(t) + \gamma V(t)I(t)/2\omega_0^2$ remains constant with time. (g) The same, constant behavior of $\eta_2(t)$ is observed at $\gamma = 1.05\omega_0$ (\mathcal{PT} -broken region, PTB). Gray traces are experimental data; red dashed lines are theory.

3.2 Experimental results for a static H_{PT}

We experimentally demonstrate this protocol with a state-of-the-art fully reconfigurable electronic oscillator comprising functional blocks synthesized with operational amplifiers (op-amps) and passive linear components [16], [76], [77]. We thus electronically reproduce the dynamics described by Eqs.(3.1) and (3.2) in the presence of a parasitic resistance $R = 10^3 \Omega$ in parallel with the LC circuit. Figure 3.2a shows for the circuit schematics, while the actual device is shown in Fig. 3.2b. $C_0 = 100 \mu\text{F}$ is minimum capacitance and $L_0 = 0.01 \text{ H}$ is the maximum inductance that our electronic platform can efficiently simulate. Their combination gives $\omega_0 = (2\pi) \times 159 \text{ Hz}$ as the fundamental frequency of the oscillator. By increasing the capacitance at different speeds, different gain-loss strengths are realized. The eigenvalues of $H_{\text{PT}}(\gamma)$ are $\pm\sqrt{\omega_0^2 - \gamma^2}$, and they change from real to complex-conjugate pair at the exceptional point marked by $\gamma_{\text{EP}} = \omega_0$.

The time-dependent evolution of the circuit energy $\mathcal{E}(t) = \langle \psi(t) | \psi(t) \rangle$ in the \mathcal{PT} -symmetric phase is shown in Fig. 3.2 (experimental data: blue dots, theory: red dashed lines). When the gain-loss strength is doubled from $\gamma = 0.375\omega_0$, Fig. 3.2c, to $\gamma = 0.75\omega_0$, Fig. 3.2d, the period of oscillations increases by $\sqrt{2}$, and the amplitude of oscillations also increases. It is worth pointing out that the fast fluctuations in the experimental data are due to oscilloscope's inherent noise; as the circuit energy $\mathcal{E}(t)$ increases from tens of micro-Joules (μJ) to a milli-Joule (mJ), the relative effect of the noise is suppressed. When $\gamma = 1.05\omega_0$, Fig. 3.2e, the system goes into the \mathcal{PT} -broken phase, as indicated by a monotonically increasing circuit energy. The temporal range of our simulation of a static $H_{\text{PT}}(\gamma)$ is limited the maximum value of capacitance, and not by the gain saturation of op-amps at high circuit energies.

For an ideal \mathcal{PT} -symmetric circuit, the energy $\mathcal{E}(t) = \langle \psi(t) | \psi(t) \rangle$ either oscillates or grows exponentially with time and yet, for all values of γ/ω_0 , this open system has two conserved quantities given by expectation values of Hermitian, intertwining operators. Recalling the intertwining relation,

$$\hat{\eta}_k H_{\text{PT}}(\gamma) = H_{\text{PT}}^\dagger(\gamma) \hat{\eta}_k. \quad (3.12)$$

In this case, the operators are

$$\hat{\eta}_1 = \sigma_y \quad (3.13)$$

$$\hat{\eta}_2 = \eta_1 H_{\text{PT}}/\omega_0 = \mathbb{1}_2 + (\gamma/\omega_0)\sigma_x. \quad (3.14)$$

The experimentally measured $\eta_2(t) \equiv \langle \psi(t) | \hat{\eta}_2 | \psi(t) \rangle = \mathcal{E}(t) + \gamma V(t)I(t)/2\omega_0^2$ is shown in Fig. 3.2f ($\gamma = 0.375\omega_0$) and Fig. 3.2g ($\gamma = 1.05\omega_0$). Gray traces are experimental data; red dashed line is theory. $\eta_2(t)$ remains flat (modulo oscilloscope noise) in both \mathcal{PT} -symmetric and \mathcal{PT} -broken regions. Note that the system starts out with $V(0) = 0.99$ Volts and $I(0) = 0$, and thus the conserved quantity $\eta_2(t) = \mathcal{E}(0)$. Since $|\psi(t)\rangle$ has real entries and $\hat{\eta}_1 = \sigma_y$ has purely imaginary entries, $\eta_1(t)$ is identically equal to zero.

3.3 Results for a time-periodic H_{PT}

The range of dynamics generated by Eq.(3.11) is tremendously enhanced if the anti-Hermitian term $\gamma(t)$ is periodic with period T . The time-evolution operator $G(t)$ at time $t = nT + \theta$ is given by $G(t) = K(\theta)G_F(T)^n$ where,

$$K(\theta) = \mathbb{T} \exp[-i \int_0^\theta H_{\text{PT}}(t') dt'], \quad (3.15)$$

captures the micromotion that occurs during a single period $0 \leq \theta < T$, \mathbb{T} denotes the time-ordered product, n is an integer, and $G_F(T) \equiv K(T) = \exp(-iT H_F)$ is the one-period time evolution operator, that, in turn, defines the Floquet Hamiltonian H_F . The complex eigenvalues λ_\pm of $G_F(T)$ determine whether the system is in the \mathcal{PT} symmetric region ($|\lambda_+| = |\lambda_-|$) or broken region ($|\lambda_+| \neq |\lambda_-|$).

Congruent with the experimental setup, we use the function $f(t) = \alpha \Pi(t) = f(t + T)$ where $\Pi(t) = \text{sgn}(t)/2$ for $|t| \leq T/2$ is the unit-step square wave (Fig. 3.3a), and α quantifies the extent of constrained variation, i.e. $e^{-\alpha} \leq C(t)/C_0, L(t)/L_0 \leq e^\alpha$. By taking into

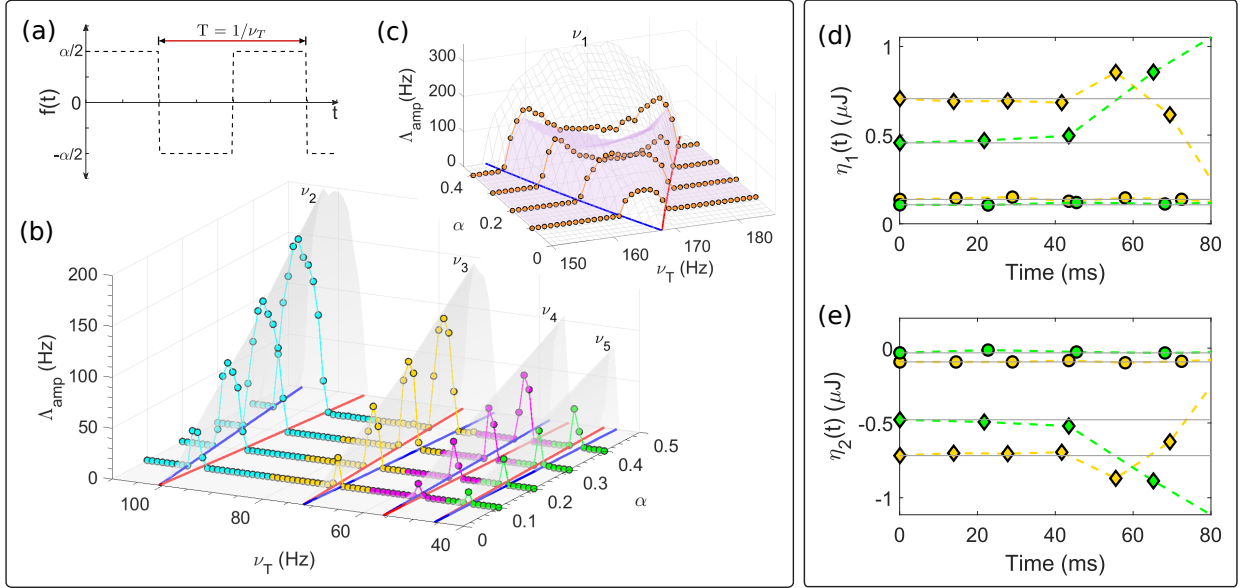


Figure 3.3. Floquet \mathcal{PT} -transitions and conserved quantities. (a) The step-function $f(t)$ switches $C(t)$ and $L(t)$ by a factor of $e^{\pm\alpha}$ and gives rise to periodic, δ -function gain and loss. Resultant EP lines emerging from odd resonances $\nu_k = 502/(2k + 1)$ Hz are shown by red and blue in the α - ν_T plane. (b) \mathcal{PT} -broken regions in the vicinity of ν_2 (cyan), ν_3 (yellow), ν_4 (pink), and ν_5 (green), signaled by $\Lambda_{\text{amp}} > 0$, are shown (experimental data: filled circles, theory: gray surface). (c) At $\nu_1 = 500/3 = 167$ Hz, the gain saturation leads to a suppressed Λ_{amp} , with the suppression largest near the resonance (experimental data: filled circles; theory with gain saturation: muve surface, theory without: gray mesh). In all cases $2\tau = 50$ ms is used in Eq.(3.18). (d) Constant of motion $\eta_{1F}(t_m)$ is measured near the ν_3 dome (yellow) in the \mathcal{PT} -symmetric phase ($\nu = 69$ Hz; circles) and \mathcal{PT} -broken phase ($\nu = 72$ Hz; diamonds). These data are at $\alpha = 0.1$. (e) Measured values of $\eta_{2F}(t_m)$ near the ν_5 dome (green), both in the \mathcal{PT} -symmetric phase ($\nu = 44$ Hz, circles) and \mathcal{PT} -broken phase ($\nu = 46$ Hz, diamonds). These data are at $\alpha = 0.2$. Gain saturation leads to non-constant behavior at times $t \gtrsim 2\tau$. Gray flat lines are theory in (d)-(e).

account the δ -function generated by $\partial_t \Pi(t)$, it is straightforward to evaluate the purely real, one-period operator

$$G_F(T) = e^{+\alpha\sigma_z} e^{-i\omega_0\sigma_y T/2} e^{-\alpha\sigma_z} e^{-i\omega_0\sigma_y T/2}. \quad (3.16)$$

Its eigenvalues are $\lambda_{\pm} = C^2 - S^2 \cosh(2\alpha) \pm iS\sqrt{D}$ where the discriminant is given by $D = C^2[1 + \cosh(2\alpha)]^2 - \sinh^2(2\alpha)$, and $C = \cos(\omega_0 T/2)$, $S = \sin(\omega_0 T/2)$. The boundary between the \mathcal{PT} -symmetric and \mathcal{PT} -broken regions in the $\alpha - \nu_T$ plane ($\nu_T = 1/T$) is marked by a vanishing discriminant $D = 0$ or, equivalently,

$$\cos(\omega_0 T/2) = \pm \tanh(\alpha_{\text{EP}}). \quad (3.17)$$

At $\alpha = 0$, the eigenvalues $\lambda_{\pm} = e^{\pm i\omega_0 T}$ of the matrix G_F become degenerate at odd resonances $2\pi\nu_n = 2\omega_0/(2n + 1)$. These are diabolic-point (DP) degeneracies. At small α symmetrical EP lines, emerging from the DP, satisfy the equation $\delta\nu_n(\alpha_{\text{EP}}) = \pm A_n \alpha_{\text{EP}}$ where $\delta\nu_n = \nu_T - \nu_n$ is the distance from DP and $A_n = 2\omega_0/[(2n + 1)\pi]^2$. Thus, the \mathcal{PT} -broken region at arbitrarily small α , bounded by the two EP lines, becomes narrower with increasing n [24], [78]. Figures 3.3b,c show these lines in the $\alpha - \nu_T$ plane.

For this set of experiments, using $C_0 = 400 \mu\text{F}$ and $L_0 = 1 \text{ mH}$ fixes the oscillator frequency at $\omega_0/(2\pi) = 251 \text{ Hz}$. We use an experimentally friendly parameter [16], [79]

$$\Lambda_{\text{amp}}(\alpha, \nu_T) = \lim_{2\tau \gg T} \frac{1}{\tau} \log \left[\frac{\max \mathcal{E}(0 \leq t \leq 2\tau)}{\max \mathcal{E}(0 \leq t \leq \tau)} \right], \quad (3.18)$$

obtained from the circuit energy to characterize the strength of the \mathcal{PT} -broken phase. Since $\mathcal{E}(t)$ oscillates in the \mathcal{PT} -symmetric phase, $\Lambda_{\text{amp}} = 0$, whereas its exponential growth in the \mathcal{PT} -broken region gives $\Lambda_{\text{amp}} > 0$. Figure 3.3b shows the emergent triangular \mathcal{PT} -broken regions at $\nu_2 = 100 \text{ Hz}$ (cyan circles), $\nu_3 = 71 \text{ Hz}$ (yellow circles), $\nu_4 = 55 \text{ Hz}$ (pink circles), and $\nu_5 = 45 \text{ Hz}$ (green circles). The gray surface is theory. In the \mathcal{PT} -broken regions, at high circuit energies, $\mathcal{E}(t)$ does not grow exponentially due to op-amp saturation. This leads to a suppression of the effective amplification rate Λ_{amp} . This suppression is maximum in the deepest \mathcal{PT} -symmetry broken region and leads to $\Lambda_{\text{amp}} \rightarrow 0$ as the circuit energy saturates

at short times. It is clearly seen in Fig. 3.3c at $\nu_1 = 167$ Hz (orange circles) at large α , but is absent at smaller values of α . The mauve surface is a theory prediction with gain saturation $+i\gamma(V)$, whereas the gray mesh is one without gain saturation. This suppression is almost complete at the primary resonance which occurs at $\nu_0 = 2\omega_0/(2\pi) = 502$ Hz (not shown) limiting the use of Eq.(3.18) to distinguish between \mathcal{PT} -symmetric and broken phases.

In the Floquet case, the conserved quantities are the expectation values of Hermitian, indefinite operators $\hat{\eta}_F$ that satisfy the intertwining relation $G_F^\dagger(T)\hat{\eta}_F G_F(T) = \hat{\eta}_F$, i.e. $\eta_F(t_m) \equiv \langle \psi(mT) | \hat{\eta}_F | \psi(mT) \rangle$ is independent of m [37]. We choose them as $\hat{\eta}_{1F} = \cosh(\alpha)\mathbb{1}_2 - \sinh(\alpha)\sigma_z + \sinh(\alpha)\tan(\omega_0 T/2)\sigma_x$ and $\hat{\eta}_{2F} = \hat{\eta}_{1F}G_F(T)$. Figure 3.3d shows η_{1F} obtained from the experimentally measured state-vector $|\psi(t)\rangle$ at times $t = t_m$. Since $\nu \sim 70$ Hz – 40 Hz, there are ~ 5 stroboscopic data points available. These are representative results in the \mathcal{PT} -symmetric (circles) and \mathcal{PT} -broken (diamonds) phases in the vicinity of ν_3 and ν_5 domes with color-coded symbols (Fig. 3.3b). Experimentally measured $\eta_{2F}(t_m)$ results are shown in Fig. 3.3e. The deviation from flat gray lines (theory) at long times $t \gtrsim 2\tau$ is due to gain saturation in the \mathcal{PT} -broken phase (diamonds). Since $G_F(T) = -\mathbb{1}_2$ at the DP degeneracies $\nu_k = 502/(2k + 1)$ Hz, we see that $\eta_{2F}(t_m) = -\eta_{1F}(t_m)$ holds, surprisingly, irrespective of the gain saturation. Similar results are valid, of course, across the entire $\alpha - \nu_T$ plane. This remarkable ability to map out the entire Floquet \mathcal{PT} -phase diagram across five domes showcases the tremendous versatility of the synthetic electronic platform, and the distinct advantage of complex gauge-field induced gain and loss mechanism over traditional approaches. This unparalleled versatility has also enabled the first demonstration of conserved quantities in the Floquet dynamics of a \mathcal{PT} -symmetric system.

3.4 Walking the EP line

As a last demonstration of the synthetic oscillator platform, we investigate the temporal dynamics at numerous points along the EP contours. This has been extremely challenging in gain-loss systems due to the requisite fine-tuning of multiple mechanisms. In loss-only \mathcal{PT} -systems, it is a challenge because decay rate is maximum at the EP.

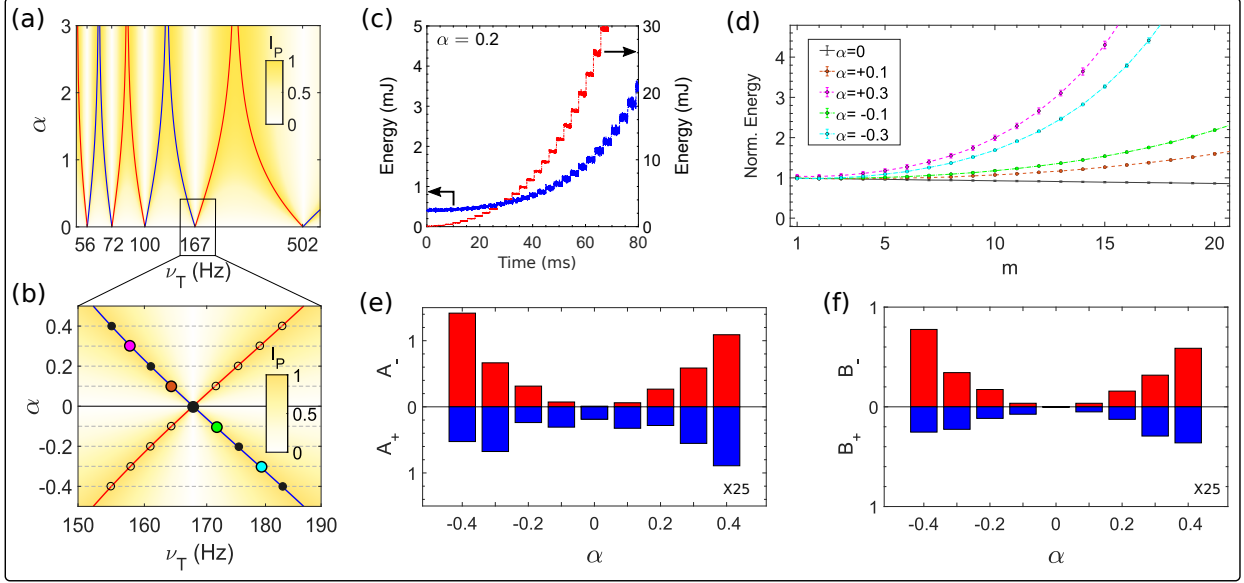


Figure 3.4. Giant dynamical asymmetry along the EP contours. (a) The inner-product heat map $I_P(\alpha, \nu_T)$ shows EP lines emerging from odd resonances $\nu_k = 502/(2k + 1)$ Hz, consistent with Eq.(3.17). (b) Zoomed-in view near $\nu_1 = 167$ Hz shows the α_{EP} values sampled for the circuit dynamics (filled and open circles). (c) Experimentally measured $\mathcal{E}(t)$ for the two EPs at $\alpha = 0.2$ show a giant asymmetry. The circuit energy is constant except at times $pT/2$ ($p \geq 1$) when the δ -function gain-loss potentials are active. (d) Color-coded stroboscopic, normalized energy traces along the blue contour show quadratic behavior consistent with a second-order EP. The (constant) energy along the flat steps in (c) is averaged to obtain error bars on $\mathcal{E}(t_m)/\mathcal{E}(0)$. By fitting the data to Eq.(3.20), $A_{\pm}(\alpha), B_{\pm}(\alpha)$ are obtained for the nine α values sampled along blue and red contours. (e) $A_{\pm}(\alpha)$ show approximate $\alpha \leftrightarrow -\alpha$ symmetry, vanish at the DP as expected, and show that $\mathcal{E}(t_m)$ growth along the red contour is ~ 25 -fold larger than along the blue contour. (f) Similar results, including a giant 25-fold asymmetry, are obtained for $B_{\pm}(\alpha)$.

A complementary way to show the \mathcal{PT} -phase diagram in the $\alpha-\nu_T$ plane is the Dirac inner-product of the right eigenvectors of $G_F(T)$. By expressing the real, Floquet evolution matrix as $G_F(T) = G_0\mathbb{1}_2 + G_x\sigma_x + G_z\sigma_z + iG_y\sigma_y$ where $G_k \in \mathbb{R}$, it is straightforward to obtain the inner-product as $I_P(\alpha, \nu_T) = \min(r, 1/r)$ where

$$r = \frac{G_y^2}{\sqrt{G_x^2 + G_z^2}} = \frac{\tanh(\alpha)}{\cos(\omega_0/2\nu_T)}. \quad (3.19)$$

Figure 3.4a shows the heat-map overlaid with EP contours, $I_P = 1$, where blue is for the plus sign and red corresponds to the minus sign in Eq.(3.17). Figure 3.4b shows the region near $\nu_1 = 167$ Hz extended to negative values of α . We “park the system” at 9 points with equidistant α_{EP} values along the blue (filled circles) and red (open circles) contours each, and obtain the circuit energy evolution $\mathcal{E}(t)$. Since the system has second-order EP contours, the stroboscopic circuit energy $\mathcal{E}(t_m) = \langle \psi(0) | G_F^\dagger(mT) G_F(mT) | \psi(0) \rangle$ grows quadratically with time t_m . Figure 3.4c shows the experimentally measured circuit energy $\mathcal{E}(t)$ at $\alpha = 0.2$ on the blue contour (blue trace) and the red contour (red trace) over $m \sim 25$ periods. It is constant except at integer and half-integer periods when the δ -function gain-loss potential is active. Surprisingly, $\mathcal{E}(t)$ also shows an order-of-magnitude asymmetry for the two contours that emerge symmetrically from the DP at ν_1 ; this asymmetry persists at all α_{EP} .

We quantify the growth of stroboscopic, normalized circuit energy $\mathcal{E}(t_m)$ with two dimensionless coefficients,

$$\frac{\mathcal{E}(t_m)}{\mathcal{E}(0)} = 1 - A_\pm(\alpha_{\text{EP}})m + B_\pm(\alpha_{\text{EP}})m^2, \quad (3.20)$$

that depend only on α_{EP} since it uniquely determines the corresponding ν_T via Eq.(3.17). This approach allows us to investigate their dependence on the proximity to the DP degeneracy at $\alpha = 0$, and the dynamical asymmetry between temporal evolution along the blue (plus) and red (minus) EP contours. At the second-order EP,

$$G_F(t_m) = e^{-ih_0T}(\mathbb{1}_2 - imTH_F) \quad (3.21)$$

where,

$$\begin{aligned}
H_F &= \frac{1}{T} [\mp 2 \sinh(\alpha_{\text{EP}}) \sigma_y \\
&\quad + 2i \tanh(\alpha_{\text{EP}}) \sigma_z \\
&\quad \pm 2i \sinh(\alpha_{\text{EP}}) \tanh(\alpha_{\text{EP}}) \sigma_x]
\end{aligned} \tag{3.22}$$

is the Floquet Hamiltonian and $h_0 T = \pi$. We obtain

$$A = iT \langle \psi(0) | H_F^\dagger - H_F | \psi(0) \rangle / \mathcal{E}(0) \tag{3.23}$$

$$B = T^2 \langle \psi(0) | H_F^\dagger H_F | \psi(0) \rangle / \mathcal{E}(0) \geq 0 \tag{3.24}$$

for the coefficients in Eq.(3.20). Figure 3.4d shows the stroboscopic, normalized circuit energy $\mathcal{E}(t_m)/\mathcal{E}(0)$ as a function of m along the blue contour for $|\alpha| = \{0, 0.1, 0.3\}$. The error bars on $\mathcal{E}(t_m)$ are obtained by averaging its value over the constant region. As the DP at $\alpha = 0$ is approached from either side, the coefficients $A_+(\alpha)$ and $B_+(\alpha)$ are monotonically suppressed to zero. The slight negative slope of $\mathcal{E}(t_m)$ at $\alpha = 0$ (no gain or loss) is due to the parasitic resistance in the circuit.

We extract the coefficients $A_-(\alpha)$ (Fig. 3.4e) and $B_-(\alpha)$ (Fig. 3.4f) from the experimental data along the red contour. Similar results, with dramatically smaller values of A_+ and B_+ , are obtained for a walk along the blue contour. They clearly demonstrate the order-of-magnitude dynamical asymmetry that arises when the same initial state $|\psi(0)\rangle$, with a fully charged capacitor, is evolved along the two symmetrical EP lines that emerge from $\nu_1 = 167$ Hz.

To summarize, most of the transformative ideas in non-Hermitian physics—Riemann surfaces, bi-orthogonal basis, exceptional points, to name a few—have been well-known in mathematics. Yet, their reinterpretation in the context of open systems has lent novel insights which could be used to support some technological advances such as enhanced sensing [70], [71], chiral mode switch [80], [81], or topological braiding [82].

We have contextualized time-dependent non-unitary transformations into a novel protocol to implement balanced gain and loss in a single oscillator. Models based on the simple

harmonic oscillator are all-pervasive in nature, and our protocol provides a recipe for their non-Hermitian generalization. For example, in a metamaterial, the non-unitary change of basis is given by the permittivity ϵ and the permeability μ . A constrained variation of the two, with a constant product (and therefore a constant index of refraction), can lead to a new class of \mathcal{PT} -symmetric metamaterials [83] without material gain or loss.

It is also easy to generalize this protocol to a network of oscillators, where the gain and loss “sites” are localized in different nodes or are distributed throughout the network. For example, with reconfigurable synthetic LC circuits, this method can lead to non-passive, \mathcal{PT} -symmetric extensions of topoelectrical circuits [84].

4. CONCLUSION

Open systems with balanced gain-loss can be described by a non-Hermitian Hamiltonian which is invariant under the combined operations of an antilinear symmetry. The consequence of such a Hamiltonian is that depending on the strength of gain and loss the eigenvalue spectrum of such a system will be either completely real, called the \mathcal{PT} -symmetric phase, or will have pairs of complex conjugate eigenvalues, called the \mathcal{PT} -broken phase. For a non-zero gain-loss strength, we also saw that the time evolution of an arbitrary state, in the symmetric phase, no longer has unit norm, but is oscillator and bounded. At the \mathcal{PT} -threshold, the time evolution of the norm has a polynomial growth, while in the broken phase, the norm of the state grows exponentially.

We have also explored time dependent Hamiltonians which with a periodic drive lead to a rich \mathcal{PT} phase diagram. This is a powerful tool to emulate other non-Hermitian systems which may not be experimentally accessible. In lattice models, we have studied the effects of surrounding a \mathcal{PT} symmetric chain with neutral chains of the same length. The primary effect is that the \mathcal{PT} transition threshold is increased by a factor equal to half the total number of chains. Although our analysis was carried out for many, long, strongly coupled chains, the results are also true for experimentally realizable \mathcal{PT} symmetric dimers and trimers. The \mathcal{PT} symmetry breaking thresholds in these systems are increased by a factor of two to three. We have investigated the dependence of the \mathcal{PT} -threshold γ_{th} on the properties of the underlying Hermitian Kitaev model and gain-loss potential locations. We have shown that the threshold profile is rich, with persistent differences between even and odd parity lattices. In particular, we have found that for a zero-detuning chain with odd number of sites, the threshold is enhanced with increasing superconducting order parameter. For an even chain with edge gain-loss potentials and superconducting coupling $\delta > 1$, we discover a re-entrant \mathcal{PT} -symmetric phase, and \mathcal{PT} -phase boundaries that contain both second and third order exceptional points. With all the attention to symmetries of the system, the conserved quantities associated with them, need to be well understood. We have reviewed conserved quantities that arise in the dynamics of systems that are governed by non-Hermitian Hamiltonians with antilinear symmetries. For isolated quantum systems

governed by Hermitian Hamiltonians, the conserved observables are linearly independent operators that commute with the Hamiltonian. Furthermore, we have presented a new method to obtain intertwining operators or conserved quantities in \mathcal{PT} -symmetric systems with static or time-periodic Hamiltonians. In this approach, these operators appear as zero- \mathcal{E} eigenmodes of the static Liouvillian \mathcal{L} or as $\lambda = 1$ eigenmodes of the Floquet \mathcal{G} . Finally, while exploring electrical circuits, we discovered that by actively manipulating the inductor and capacitor in a ‘single’ LC oscillator circuit, we see signatures of \mathcal{PT} -symmetry, which is counter-intuitive from the traditional idea for the need of a pair of gain-loss elements to see \mathcal{PT} transitions. This is possible if we realise that the time dependent non-unitary transformation of basis, gives rise to a gauge term that can be interpreted as a non-Hermitian potential with spatially separated balance gain and loss elements.

REFERENCES

- [1] C. M. Bender and S. Boettcher, “Real spectra in non-hermitian hamiltonians Having-PTSymmetry,” *Phys. Rev. Lett.*, vol. 80, no. 24, pp. 5243–5246, Jun. 1998. DOI: [10.1103/physrevlett.80.5243](https://doi.org/10.1103/physrevlett.80.5243). [Online]. Available: <https://doi.org/10.1103/physrevlett.80.5243>.
- [2] C. M. Bender, D. C. Brody, and H. F. Jones, “Complex extension of quantum mechanics,” *Phys. Rev. Lett.*, vol. 89, p. 270 401, 27 Dec. 2002. DOI: [10.1103/PhysRevLett.89.270401](https://doi.org/10.1103/PhysRevLett.89.270401). [Online]. Available: <https://link.aps.org/doi/10.1103/PhysRevLett.89.270401>.
- [3] L. Feng, R. El-Ganainy, and L. Ge, “Non-hermitian photonics based on parity–time symmetry,” *Nat. Photonics*, vol. 11, no. 12, pp. 752–762, Nov. 2017. DOI: [10.1038/s41566-017-0031-1](https://doi.org/10.1038/s41566-017-0031-1). [Online]. Available: <https://doi.org/10.1038/s41566-017-0031-1>.
- [4] R. El-Ganainy, K. G. Makris, M. Khajavikhan, Z. H. Musslimani, S. Rotter, and D. N. Christodoulides, “Non-hermitian physics and PT symmetry,” *Nat. Phys.*, vol. 14, no. 1, pp. 11–19, Jan. 2018. DOI: [10.1038/nphys4323](https://doi.org/10.1038/nphys4323). [Online]. Available: <https://doi.org/10.1038/nphys4323>.
- [5] Ş. K. Özdemir, S. Rotter, F. Nori, and L. Yang, “Parity–time symmetry and exceptional points in photonics,” *Nat. Mater.*, vol. 18, no. 8, pp. 783–798, Apr. 2019. DOI: [10.1038/s41563-019-0304-9](https://doi.org/10.1038/s41563-019-0304-9). [Online]. Available: <https://doi.org/10.1038/s41563-019-0304-9>.
- [6] A. Mostafazadeh, “Pseudo-hermiticity versus PT symmetry: The necessary condition for the reality of the spectrum of a non-hermitian hamiltonian,” *J. Math. Phys.*, vol. 43, no. 1, pp. 205–214, Jan. 2002. DOI: [10.1063/1.1418246](https://doi.org/10.1063/1.1418246). [Online]. Available: <https://doi.org/10.1063/1.1418246>.
- [7] A. Mostafazadeh, “Pseudo-hermitian representation of quantum mechanics,” *International Journal of Geometric Methods in Modern Physics*, vol. 07, no. 07, pp. 1191–1306, Nov. 2010. DOI: [10.1142/s0219887810004816](https://doi.org/10.1142/s0219887810004816). [Online]. Available: <https://doi.org/10.1142/s0219887810004816>.
- [8] C. E. Rüter, K. G. Makris, R. El-Ganainy, D. N. Christodoulides, M. Segev, and D. Kip, “Observation of parity–time symmetry in optics,” *Nat. Phys.*, vol. 6, no. 3, pp. 192–195, Jan. 2010. DOI: [10.1038/nphys1515](https://doi.org/10.1038/nphys1515). [Online]. Available: <https://doi.org/10.1038/nphys1515>.
- [9] A. Regensburger, C. Bersch, M.-A. Miri, G. Onishchukov, D. N. Christodoulides, and U. Peschel, “Parity–time synthetic photonic lattices,” *Nature*, vol. 488, no. 7410, pp. 167–171, Aug. 2012. DOI: [10.1038/nature11298](https://doi.org/10.1038/nature11298). [Online]. Available: <https://doi.org/10.1038/nature11298>.

- [10] L. Chang, X. Jiang, S. Hua, C. Yang, J. Wen, L. Jiang, G. Li, G. Wang, and M. Xiao, “Parity–time symmetry and variable optical isolation in active–passive-coupled microresonators,” *Nat. Photonics*, vol. 8, no. 7, pp. 524–529, Jun. 2014. DOI: [10.1038/nphoton.2014.133](https://doi.org/10.1038/nphoton.2014.133). [Online]. Available: <https://doi.org/10.1038/nphoton.2014.133>.
- [11] H. Hodaei, M.-A. Miri, M. Heinrich, D. N. Christodoulides, and M. Khajavikhan, “Parity-time-symmetric microring lasers,” *Science*, vol. 346, no. 6212, pp. 975–978, Oct. 2014. DOI: [10.1126/science.1258480](https://doi.org/10.1126/science.1258480). [Online]. Available: <https://doi.org/10.1126/science.1258480>.
- [12] J. Schindler, A. Li, M. C. Zheng, F. M. Ellis, and T. Kottos, “Experimental study of active lrc circuits with \mathcal{PT} symmetries,” *Phys. Rev. A*, vol. 84, p. 040101, 4 Oct. 2011. DOI: [10.1103/PhysRevA.84.040101](https://link.aps.org/doi/10.1103/PhysRevA.84.040101). [Online]. Available: <https://link.aps.org/doi/10.1103/PhysRevA.84.040101>.
- [13] Y. Choi, C. Hahn, J. W. Yoon, and S. H. Song, “Observation of an anti-pt-symmetric exceptional point and energy-difference conserving dynamics in electrical circuit resonators,” *Nat. Commun.*, vol. 9, no. 1, p. 2182, 2018, ISSN: 2041-1723. DOI: [10.1038/s41467-018-04690-y](https://doi.org/10.1038/s41467-018-04690-y). [Online]. Available: <https://doi.org/10.1038/s41467-018-04690-y>.
- [14] C. M. Bender, B. K. Berntson, D. Parker, and E. Samuel, “Observation of PT phase transition in a simple mechanical system,” *Am. J. Phys.*, vol. 81, no. 3, pp. 173–179, Mar. 2013. DOI: [10.1119/1.4789549](https://doi.org/10.1119/1.4789549). [Online]. Available: <https://doi.org/10.1119/1.4789549>.
- [15] A. Guo, G. J. Salamo, D. Duchesne, R. Morandotti, M. Volatier-Ravat, V. Aimez, G. A. Siviloglou, and D. N. Christodoulides, “Observation of \mathcal{PT} -symmetry breaking in complex optical potentials,” *Phys. Rev. Lett.*, vol. 103, p. 093902, 9 Aug. 2009. DOI: [10.1103/PhysRevLett.103.093902](https://link.aps.org/doi/10.1103/PhysRevLett.103.093902). [Online]. Available: <https://link.aps.org/doi/10.1103/PhysRevLett.103.093902>.
- [16] R. d. J. Leon-Montiel, M. A. Quiroz-Juarez, J. L. Dominguez-Juarez, R. Quintero-Torres, J. L. Aragon, A. K. Harter, and Y. N. Joglekar, “Observation of slowly decaying eigenmodes without exceptional points in floquet dissipative synthetic circuits,” *Commun. Phys.*, vol. 1, no. 1, p. 88, 2018, ISSN: 2399-3650. DOI: [10.1038/s42005-018-0087-3](https://doi.org/10.1038/s42005-018-0087-3). [Online]. Available: <https://doi.org/10.1038/s42005-018-0087-3>.
- [17] J. Li, A. K. Harter, J. Liu, L. de Melo, Y. N. Joglekar, and L. Luo, “Observation of parity-time symmetry breaking transitions in a dissipative floquet system of ultracold atoms,” *Nat. Commun.*, vol. 10, no. 1, p. 855, 2019, ISSN: 2041-1723. DOI: [10.1038/s41467-019-08596-1](https://doi.org/10.1038/s41467-019-08596-1). [Online]. Available: <https://doi.org/10.1038/s41467-019-08596-1>.
- [18] Y. Wu, W. Liu, J. Geng, X. Song, X. Ye, C.-K. Duan, X. Rong, and J. Du, “Observation of parity-time symmetry breaking in a single-spin system,” *Science*, vol. 364, no. 6443, pp. 878–880, May 2019. DOI: [10.1126/science.aaw8205](https://doi.org/10.1126/science.aaw8205). [Online]. Available: <https://doi.org/10.1126/science.aaw8205>.

- [19] M. Naghiloo, M. Abbasi, Y. N. Joglekar, and K. W. Murch, “Quantum state tomography across the exceptional point in a single dissipative qubit,” *Nat. Phys.*, vol. 15, no. 12, pp. 1232–1236, Oct. 2019. DOI: [10.1038/s41567-019-0652-z](https://doi.org/10.1038/s41567-019-0652-z). [Online]. Available: <https://doi.org/10.1038/s41567-019-0652-z>.
- [20] F. Klauck, L. Teuber, M. Ornigotti, M. Heinrich, S. Scheel, and A. Szameit, “Observation of PT-symmetric quantum interference,” *Nat. Photonics*, vol. 13, no. 12, pp. 883–887, Sep. 2019. DOI: [10.1038/s41566-019-0517-0](https://doi.org/10.1038/s41566-019-0517-0). [Online]. Available: <https://doi.org/10.1038/s41566-019-0517-0>.
- [21] Y. N. Joglekar, C. Thompson, D. D. Scott, and G. Vemuri, “Optical waveguide arrays: Quantum effects and PT symmetry breaking,” *The European Physical Journal Applied Physics*, vol. 63, no. 3, p. 30 001, Sep. 2013. DOI: [10.1051/epjap/2013130240](https://doi.org/10.1051/epjap/2013130240). [Online]. Available: <https://doi.org/10.1051/epjap/2013130240>.
- [22] C. M. Bender and P. D. Mannheim, “Symmetry and necessary and sufficient conditions for the reality of energy eigenvalues,” *Physics Letters A*, vol. 374, no. 15-16, pp. 1616–1620, Apr. 2010. DOI: [10.1016/j.physleta.2010.02.032](https://doi.org/10.1016/j.physleta.2010.02.032). [Online]. Available: <https://doi.org/10.1016/j.physleta.2010.02.032>.
- [23] P. D. Mannheim, “Antilinearity rather than hermiticity as a guiding principle for quantum theory,” *Journal of Physics A: Mathematical and Theoretical*, vol. 51, no. 31, p. 315 302, Jun. 2018. DOI: [10.1088/1751-8121/aac035](https://doi.org/10.1088/1751-8121/aac035). [Online]. Available: <https://doi.org/10.1088/1751-8121/aac035>.
- [24] A. K. Harter and Y. N. Joglekar, “Connecting active and passive \mathcal{PT} -symmetric floquet systems,” *Progress of Theoretical and Experimental Physics*, vol. 2020, no. 12, Dec. 2020. DOI: [10.1093/ptep/ptaa181](https://doi.org/10.1093/ptep/ptaa181). [Online]. Available: <https://doi.org/10.1093/ptep/ptaa181>.
- [25] E. P. Wigner and U. Fano, “Group theory and its application to the quantum mechanics of atomic spectra,” *American Journal of Physics*, vol. 28, no. 4, pp. 408–409, Apr. 1960. DOI: [10.1119/1.1935822](https://doi.org/10.1119/1.1935822). [Online]. Available: <https://doi.org/10.1119/1.1935822>.
- [26] A. Mostafazadeh, “Exact PT-symmetry is equivalent to Hermiticity,” *Journal of Physics A: Mathematical and General*, vol. 36, no. 25, pp. 7081–7091, 2003, ISSN: 03054470. DOI: [10.1088/0305-4470/36/25/312](https://doi.org/10.1088/0305-4470/36/25/312).
- [27] H. Goldstein, *Classical mechanics*. San Francisco: Addison Wesley, 2002, ISBN: 0201657023.
- [28] M. Znojil, “Complete set of inner products for a discrete \mathcal{PT} -symmetric square-well hamiltonian,” *Journal of Mathematical Physics*, vol. 50, no. 12, p. 122 105, Dec. 2009. DOI: [10.1063/1.3272002](https://doi.org/10.1063/1.3272002). [Online]. Available: <https://doi.org/10.1063/1.3272002>.

- [29] Z. Bian, L. Xiao, K. Wang, X. Zhan, F. A. Onanga, F. Ruzicka, W. Yi, Y. N. Joglekar, and P. Xue, “Conserved quantities in parity-time symmetric systems,” *Phys. Rev. Res.*, vol. 2, no. 2, May 2020. DOI: [10.1103/physrevresearch.2.022039](https://doi.org/10.1103/physrevresearch.2.022039). [Online]. Available: <https://doi.org/10.1103/physrevresearch.2.022039>.
- [30] K. S. Agarwal, J. Muldoon, and Y. N. Joglekar, “Conserved quantities in non-hermitian systems via vectorization method,” *arXiv preprint arXiv:2201.05019*, 2022.
- [31] V. Gorini, A. Kossakowski, and E. Sudarshan, “Completely positive dynamical semigroups of n-level systems,” *Journal of Mathematical Physics*, vol. 17, no. 5, p. 821, 1976. DOI: [10.1063/1.522979](https://doi.org/10.1063/1.522979). [Online]. Available: <https://doi.org/10.1063/1.522979>.
- [32] G. Lindblad, “On the generators of quantum dynamical semigroups,” *Comm. Math. Phys.*, vol. 48, no. 2, pp. 119–130, 1976. [Online]. Available: <https://projecteuclid.org/443/euclid.cmp/1103899849>.
- [33] M. Ban, “Lie-algebra methods in quantum optics: The liouville-space formulation,” *Physical Review A*, vol. 47, no. 6, pp. 5093–5119, Jun. 1993. DOI: [10.1103/physreva.47.5093](https://doi.org/10.1103/physreva.47.5093). [Online]. Available: <https://doi.org/10.1103/physreva.47.5093>.
- [34] V. V. Albert and L. Jiang, “Symmetries and conserved quantities in lindblad master equations,” *Phys. Rev. A*, vol. 89, p. 022 118, 2 Feb. 2014. DOI: [10.1103/PhysRevA.89.022118](https://doi.org/10.1103/PhysRevA.89.022118). [Online]. Available: <https://link.aps.org/doi/10.1103/PhysRevA.89.022118>.
- [35] D. Manzano, “A short introduction to the lindblad master equation,” *AIP Advances*, vol. 10, no. 2, p. 025 106, Feb. 2020. DOI: [10.1063/1.5115323](https://doi.org/10.1063/1.5115323). [Online]. Available: <https://doi.org/10.1063/1.5115323>.
- [36] J. Gunderson, J. Muldoon, K. W. Murch, and Y. N. Joglekar, “Floquet exceptional contours in lindblad dynamics with time-periodic drive and dissipation,” *Phys. Rev. A*, vol. 103, p. 023 718, 2 Feb. 2021. DOI: [10.1103/PhysRevA.103.023718](https://doi.org/10.1103/PhysRevA.103.023718). [Online]. Available: <https://link.aps.org/doi/10.1103/PhysRevA.103.023718>.
- [37] F. Ruzicka, K. S. Agarwal, and Y. N. Joglekar, *Conserved quantities, exceptional points, and antilinear symmetries in non-hermitian systems*, 2021. arXiv: [2104.11265](https://arxiv.org/abs/2104.11265) [quant-ph].
- [38] Y. N. Joglekar, R. Marathe, P. Durganandini, and R. K. Pathak, “PTspectroscopy of the rabi problem,” *Physical Review A*, vol. 90, no. 4, p. 040 101, Oct. 2014. DOI: [10.1103/physreva.90.040101](https://doi.org/10.1103/physreva.90.040101). [Online]. Available: <https://doi.org/10.1103/physreva.90.040101>.
- [39] T. E. Lee and Y. N. Joglekar, “ \mathcal{PT} -symmetric rabi model: Perturbation theory,” *Phys. Rev. A*, vol. 92, p. 042 103, 4 Oct. 2015. DOI: [10.1103/PhysRevA.92.042103](https://doi.org/10.1103/PhysRevA.92.042103). [Online]. Available: <https://link.aps.org/doi/10.1103/PhysRevA.92.042103>.

- [40] J. Li, A. K. Harter, J. Liu, L. de Melo, Y. N. Joglekar, and L. Luo, “Observation of parity-time symmetry breaking transitions in a dissipative floquet system of ultracold atoms,” *Nature Communications*, vol. 10, no. 1, Feb. 2019. DOI: [10.1038/s41467-019-08596-1](https://doi.org/10.1038/s41467-019-08596-1). [Online]. Available: <https://doi.org/10.1038/s41467-019-08596-1>.
- [41] M. A. Quiroz-Juárez, K. S. Agarwal, Z. A. Cochran, J. L. Aragón, Y. N. Joglekar, and R. d. J. León-Montiel, “On-demand parity-time symmetry in a lone oscillator through complex, synthetic gauge fields,” *arXiv preprint arXiv:2109.03846*, 2021.
- [42] P. Hanggi, *Driven quantum systems*, 1998 (accessed October 31, 2020). [Online]. Available: https://www.physik.uni-augsburg.de/theo1/hanggi/Chapter_5.pdf.
- [43] A. Ruschhaupt, F. Delgado, and J. G. Muga, “Physical realization of \mathcal{P} -symmetric potential scattering in a planar slab waveguide,” *Journal of Physics A: Mathematical and General*, vol. 38, no. 9, pp. L171–L176, Feb. 2005. DOI: [10.1088/0305-4470/38/9/103](https://doi.org/10.1088/0305-4470/38/9/103). [Online]. Available: <https://doi.org/10.1088/0305-4470/38/9/103>.
- [44] K. G. Makris, R. El-Ganainy, D. N. Christodoulides, and Z. H. Musslimani, “Beam dynamics in \mathcal{PT} -symmetric optical lattices,” *Phys. Rev. Lett.*, vol. 100, no. 10, Mar. 2008. DOI: [10.1103/physrevlett.100.103904](https://doi.org/10.1103/physrevlett.100.103904). [Online]. Available: <https://doi.org/10.1103/physrevlett.100.103904>.
- [45] M. S. Wartak, *Computational Photonics*. Cambridge University Press, 2009. DOI: [10.1017/cbo9780511794247](https://doi.org/10.1017/cbo9780511794247). [Online]. Available: <https://doi.org/10.1017/cbo9780511794247>.
- [46] Y. N. Joglekar and J. L. Barnett, “Origin of maximal symmetry breaking in even \mathcal{PT} -symmetric lattices,” *Phys. Rev. A*, vol. 84, p. 024 103, 2 Aug. 2011. DOI: [10.1103/PhysRevA.84.024103](https://link.aps.org/doi/10.1103/PhysRevA.84.024103). [Online]. Available: <https://link.aps.org/doi/10.1103/PhysRevA.84.024103>.
- [47] K. S. Agarwal, R. K. Pathak, and Y. N. Joglekar, “Raising the \mathcal{PT} -transition threshold by strong coupling to neutral chains,” *Phys. Rev. A*, vol. 97, p. 042 107, 4 Apr. 2018. DOI: [10.1103/PhysRevA.97.042107](https://link.aps.org/doi/10.1103/PhysRevA.97.042107). [Online]. Available: <https://link.aps.org/doi/10.1103/PhysRevA.97.042107>.
- [48] Y. N. Joglekar, D. Scott, M. Babbey, and A. Saxena, “Robust and fragile \mathcal{PT} -symmetric phases in a tight-binding chain,” *Phys. Rev. A*, vol. 82, p. 030 103, 3 Sep. 2010. DOI: [10.1103/PhysRevA.82.030103](https://link.aps.org/doi/10.1103/PhysRevA.82.030103). [Online]. Available: <https://link.aps.org/doi/10.1103/PhysRevA.82.030103>.
- [49] A. Y. Kitaev, “Unpaired majorana fermions in quantum wires,” *Phys. Usp.*, vol. 44, no. 10S, pp. 131–136, Oct. 2001. DOI: [10.1070/1063-7869/44/10s/s29](https://doi.org/10.1070/1063-7869/44/10s/s29). [Online]. Available: <https://doi.org/10.1070/1063-7869/44/10s/s29>.

- [50] C. Yuce, “Majorana edge modes with gain and loss,” *Phys. Rev. A*, vol. 93, p. 062 130, 6 Jun. 2016. DOI: [10.1103/PhysRevA.93.062130](https://doi.org/10.1103/PhysRevA.93.062130). [Online]. Available: <https://link.aps.org/doi/10.1103/PhysRevA.93.062130>.
- [51] K. Kawabata, Y. Ashida, H. Katsura, and M. Ueda, “Parity-time-symmetric topological superconductor,” *Phys. Rev. B*, vol. 98, p. 085 116, 8 Aug. 2018. DOI: [10.1103/PhysRevB.98.085116](https://doi.org/10.1103/PhysRevB.98.085116). [Online]. Available: <https://link.aps.org/doi/10.1103/PhysRevB.98.085116>.
- [52] X. Wang, T. Liu, Y. Xiong, and P. Tong, “Spontaneous \mathcal{PT} -symmetry breaking in non-hermitian kitaev and extended kitaev models,” *Phys. Rev. A*, vol. 92, p. 012 116, 1 Jul. 2015. DOI: [10.1103/PhysRevA.92.012116](https://doi.org/10.1103/PhysRevA.92.012116). [Online]. Available: <https://link.aps.org/doi/10.1103/PhysRevA.92.012116>.
- [53] C. Li, X. Z. Zhang, G. Zhang, and Z. Song, “Topological phases in a kitaev chain with imbalanced pairing,” *Phys. Rev. B*, vol. 97, p. 115 436, 11 Mar. 2018. DOI: [10.1103/PhysRevB.97.115436](https://doi.org/10.1103/PhysRevB.97.115436). [Online]. Available: <https://link.aps.org/doi/10.1103/PhysRevB.97.115436>.
- [54] S. Yao and Z. Wang, “Edge states and topological invariants of non-hermitian systems,” *Phys. Rev. Lett.*, vol. 121, p. 086 803, 8 Aug. 2018. DOI: [10.1103/PhysRevLett.121.086803](https://doi.org/10.1103/PhysRevLett.121.086803). [Online]. Available: <https://link.aps.org/doi/10.1103/PhysRevLett.121.086803>.
- [55] M. Klett, H. Cartarius, D. Dast, J. Main, and G. Wunner, “Relation between \mathcal{PT} -symmetry breaking and topologically nontrivial phases in the su-schrieffer-heeger and kitaev models,” *Phys. Rev. A*, vol. 95, p. 053 626, 5 May 2017. DOI: [10.1103/PhysRevA.95.053626](https://doi.org/10.1103/PhysRevA.95.053626). [Online]. Available: <https://link.aps.org/doi/10.1103/PhysRevA.95.053626>.
- [56] C. Li, L. Jin, and Z. Song, “Coalescing majorana edge modes in non-hermitian pt-symmetric kitaev chain,” *Sci. Rep.*, vol. 10, no. 1, p. 6807, 2020, ISSN: 2045-2322. DOI: [10.1038/s41598-020-63369-x](https://doi.org/10.1038/s41598-020-63369-x). [Online]. Available: <https://doi.org/10.1038/s41598-020-63369-x>.
- [57] S. D. Sarma, M. Freedman, and C. Nayak, “Majorana zero modes and topological quantum computation,” *npj Quantum Inf.*, vol. 1, no. 1, p. 15 001, 2015, ISSN: 2056-6387. DOI: [10.1038/npjqi.2015.1](https://doi.org/10.1038/npjqi.2015.1). [Online]. Available: <https://doi.org/10.1038/npjqi.2015.1>.
- [58] N. Leumer, M. Marganska, B. Muralidharan, and M. Grifoni, “Exact eigenvectors and eigenvalues of the finite kitaev chain and its topological properties,” *J. Phys.: Condens. Matter*, vol. 32, no. 44, p. 445 502, Aug. 2020. DOI: [10.1088/1361-648x/ab8bf9](https://doi.org/10.1088/1361-648x/ab8bf9). [Online]. Available: <https://doi.org/10.1088/1361-648x/ab8bf9>.
- [59] K. S. Agarwal and Y. N. Joglekar, *\mathcal{PT} -symmetry breaking in a kitaev chain with one pair of gain-loss potentials*, 2021. arXiv: [2103.07058](https://arxiv.org/abs/2103.07058) [quant-ph].

- [60] H. Vemuri and Y. N. Joglekar, “ \mathcal{PT} -symmetric lattices with a local degree of freedom,” *Phys. Rev. A*, vol. 87, p. 044 101, 4 Apr. 2013. DOI: [10.1103/PhysRevA.87.044101](https://doi.org/10.1103/PhysRevA.87.044101). [Online]. Available: <https://link.aps.org/doi/10.1103/PhysRevA.87.044101>.
- [61] D. D. Scott and Y. N. Joglekar, “ \mathcal{PT} -symmetry breaking and ubiquitous maximal chirality in a \mathcal{PT} -symmetric ring,” *Phys. Rev. A*, vol. 85, p. 062 105, 6 Jun. 2012. DOI: [10.1103/PhysRevA.85.062105](https://doi.org/10.1103/PhysRevA.85.062105). [Online]. Available: <https://link.aps.org/doi/10.1103/PhysRevA.85.062105>.
- [62] A. K. Harter, T. E. Lee, and Y. N. Joglekar, “ \mathcal{PT} -breaking threshold in spatially asymmetric aubry-andré and harper models: Hidden symmetry and topological states,” *Phys. Rev. A*, vol. 93, p. 062 101, 6 Jun. 2016. DOI: [10.1103/PhysRevA.93.062101](https://doi.org/10.1103/PhysRevA.93.062101). [Online]. Available: <https://link.aps.org/doi/10.1103/PhysRevA.93.062101>.
- [63] A. K. Harter, F. A. Onanga, and Y. N. Joglekar, “Veiled symmetry of disordered parity-time lattices: Protected \mathcal{PT} -threshold and the fate of localization,” *Sci. Rep.*, vol. 8, no. 1, Jan. 2018. DOI: [10.1038/s41598-017-18589-z](https://doi.org/10.1038/s41598-017-18589-z). [Online]. Available: <https://doi.org/10.1038/s41598-017-18589-z>.
- [64] Y. N. Joglekar, C. Thompson, and G. Vemuri, “Tunable waveguide lattices with nonuniform parity-symmetric tunneling,” *Phys. Rev. A*, vol. 83, p. 063 817, 6 Jun. 2011. DOI: [10.1103/PhysRevA.83.063817](https://doi.org/10.1103/PhysRevA.83.063817). [Online]. Available: <https://link.aps.org/doi/10.1103/PhysRevA.83.063817>.
- [65] Y. N. Joglekar and B. Bagchi, “Competing \mathcal{PT} potentials and the re-entrant \mathcal{PT} -symmetric phase: A particle in a box,” *Journal of Physics A: Mathematical and Theoretical*, vol. 45, no. 40, p. 402 001, Sep. 2012. DOI: [10.1088/1751-8113/45/40/402001](https://doi.org/10.1088/1751-8113/45/40/402001). [Online]. Available: <https://doi.org/10.1088/1751-8113/45/40/402001>.
- [66] C. H. Liang, D. D. Scott, and Y. N. Joglekar, “ \mathcal{PT} restoration via increased loss and gain in the \mathcal{PT} -symmetric aubry-andré model,” *Phys. Rev. A*, vol. 89, p. 030 102, 3 Mar. 2014. DOI: [10.1103/PhysRevA.89.030102](https://doi.org/10.1103/PhysRevA.89.030102). [Online]. Available: <https://link.aps.org/doi/10.1103/PhysRevA.89.030102>.
- [67] D. Duchesne, V. Aimez, R. Morandotti, D. N. Christodoulides, G. J. Salamo, M. Volatier-Ravat, G. A. Siviloglou, and A. Guo, “Observation of \mathcal{PT} -Symmetry Breaking in Complex Optical Potentials,” *Physical Review Letters*, vol. 103, no. 9, pp. 1–4, 2009, ISSN: 0031-9007. DOI: [10.1103/physrevlett.103.093902](https://doi.org/10.1103/physrevlett.103.093902).
- [68] T. Wang, J. Fang, Z. Xie, N. Dong, Y. N. Joglekar, Z. Wang, J. Li, and L. Luo, “Observation of two \mathcal{PT} transitions in an electric circuit with balanced gain and loss,” *The European Physical Journal D*, vol. 74, no. 8, Aug. 2020. DOI: [10.1140/epjd/e2020-10131-7](https://doi.org/10.1140/epjd/e2020-10131-7). [Online]. Available: <https://doi.org/10.1140/epjd/e2020-10131-7>.

- [69] B. Peng, S. K. Özdemir, S. Rotter, H. Yilmaz, M. Liertzer, F. Monifi, C. M. Bender, F. Nori, and L. Yang, “Loss-induced suppression and revival of lasing,” *Science*, vol. 346, p. 328, 2014.
- [70] H. Hodaiei, A. U. Hassan, S. Wittek, H. Garcia-Gracia, R. El-Ganainy, D. N. Christodoulides, and M. Khajavikhan, “Enhanced sensitivity at higher-order exceptional points,” *Nature*, vol. 548, no. 7666, pp. 187–191, Aug. 2017. DOI: [10.1038/nature23280](https://doi.org/10.1038/nature23280). [Online]. Available: <https://doi.org/10.1038/nature23280>.
- [71] W. Chen, Ş. K. Özdemir, G. Zhao, J. Wiersig, and L. Yang, “Exceptional points enhance sensing in an optical microcavity,” *Nature*, vol. 548, no. 7666, pp. 192–196, Aug. 2017. DOI: [10.1038/nature23281](https://doi.org/10.1038/nature23281). [Online]. Available: <https://doi.org/10.1038/nature23281>.
- [72] X. Zhu, H. Ramezani, C. Shi, J. Zhu, and X. Zhang, “ \mathcal{PT} -symmetric acoustics,” *Phys. Rev. X*, vol. 4, p. 031 042, 3 Sep. 2014. DOI: [10.1103/PhysRevX.4.031042](https://doi.org/10.1103/PhysRevX.4.031042). [Online]. Available: <https://link.aps.org/doi/10.1103/PhysRevX.4.031042>.
- [73] F. R. Humire, Y. N. Joglekar, and M. A. G. Nustes, *Rabi oscillations of dissipative structures effected by out-of-phase parametric drives*, 2019. arXiv: [1905.03896](https://arxiv.org/abs/1905.03896) [[nlin.PS](#)].
- [74] G. Vemuri, A. Wilkey, and Y. N. Joglekar, “Exceptional points in anti-PT symmetric system of delay coupled semiconductor lasers,” in *Active Photonic Platforms XIII*, G. S. Subramania and S. Foteinopoulou, Eds., SPIE, Aug. 2021. DOI: [10.1117/12.2593311](https://doi.org/10.1117/12.2593311). [Online]. Available: <https://doi.org/10.1117/12.2593311>.
- [75] M. Nakahara, *Geometry, topology, and physics*. Bristol Philadelphia Boca Raton Fla: Institute of Physics Pub. CRC Press, an imprint of Taylor & Francis Group, 2003, ISBN: 978-0750306065.
- [76] M. A. Quiroz-Juárez, J. Chávez-Carlos, J. L. Aragón, J. G. Hirsch, and R. de J. León-Montiel, “Experimental realization of the classical dicke model,” *Phys. Rev. Research*, vol. 2, p. 033 169, 3 Jul. 2020. DOI: [10.1103/PhysRevResearch.2.033169](https://doi.org/10.1103/PhysRevResearch.2.033169). [Online]. Available: <https://link.aps.org/doi/10.1103/PhysRevResearch.2.033169>.
- [77] M. A. Quiroz-Juárez, C. You, J. Carrillo-Martínez, D. Montiel-Álvarez, J. L. Aragón, O. S. Magaña-Loaiza, and R. de J. León-Montiel, “Reconfigurable network for quantum transport simulations,” *Phys. Rev. Research*, vol. 3, p. 013 010, 1 Jan. 2021. DOI: [10.1103/PhysRevResearch.3.013010](https://doi.org/10.1103/PhysRevResearch.3.013010). [Online]. Available: <https://link.aps.org/doi/10.1103/PhysRevResearch.3.013010>.
- [78] A. Kumar, K. W. Murch, and Y. N. Joglekar, *Maximal quantum entanglement at exceptional points via unitary and thermal dynamics*, 2021. arXiv: [2109.07503](https://arxiv.org/abs/2109.07503) [[quant-ph](#)].

- [79] Z. A. Cochran, A. Saxena, and Y. N. Joglekar, “Parity-time symmetric systems with memory,” *Phys. Rev. Research*, vol. 3, p. 013 135, 1 Feb. 2021. DOI: [10.1103/PhysRevResearch.3.013135](https://doi.org/10.1103/PhysRevResearch.3.013135). [Online]. Available: <https://link.aps.org/doi/10.1103/PhysRevResearch.3.013135>.
- [80] J. Doppler, A. A. Mailybaev, J. Böhm, U. Kuhl, A. Girschik, F. Libisch, T. J. Milburn, P. Rabl, N. Moiseyev, and S. Rotter, “Dynamically encircling an exceptional point for asymmetric mode switching,” *Nature*, vol. 537, no. 7618, pp. 76–79, Jul. 2016. DOI: [10.1038/nature18605](https://doi.org/10.1038/nature18605). [Online]. Available: <https://doi.org/10.1038/nature18605>.
- [81] H. Xu, D. Mason, L. Jiang, and J. G. E. Harris, “Topological energy transfer in an optomechanical system with exceptional points,” *Nature*, vol. 537, no. 7618, pp. 80–83, Jul. 2016. DOI: [10.1038/nature18604](https://doi.org/10.1038/nature18604). [Online]. Available: <https://doi.org/10.1038/nature18604>.
- [82] K. Wang, A. Dutt, C. C. Wojcik, and S. Fan, “Topological complex-energy braiding of non-hermitian bands,” *Nature*, vol. 598, no. 7879, pp. 59–64, Oct. 2021. DOI: [10.1038/s41586-021-03848-x](https://doi.org/10.1038/s41586-021-03848-x). [Online]. Available: <https://doi.org/10.1038/s41586-021-03848-x>.
- [83] S. Droulias, I. Katsantonis, M. Kafesaki, C. M. Soukoulis, and E. N. Economou, “Chiral metamaterials with pt symmetry and beyond,” *Phys. Rev. Lett.*, vol. 122, p. 213 201, 21 May 2019. DOI: [10.1103/PhysRevLett.122.213201](https://doi.org/10.1103/PhysRevLett.122.213201). [Online]. Available: <https://link.aps.org/doi/10.1103/PhysRevLett.122.213201>.
- [84] C. H. Lee, S. Imhof, C. Berger, F. Bayer, J. Brehm, L. W. Molenkamp, T. Kiessling, and R. Thomale, “Topoelectrical circuits,” *Commun Phys*, vol. 1, no. 1, Jul. 2018. DOI: [10.1038/s42005-018-0035-2](https://doi.org/10.1038/s42005-018-0035-2). [Online]. Available: <https://doi.org/10.1038/s42005-018-0035-2>.